Implementation of TALIF on negative ion sources for the determination of the properties of atomic hydrogen

Dissertation

zur Erlangung des akademischen Grades

Dr. rer. nat.

eingereicht an der
Mathematisch-Naturwissenschaftlich-Technischen Fakultät
der Universität Augsburg

von

Frederik Merk

Augsburg, September 2022

Universität
Augsburg
University

Tag der mündlichen Prüfung: 07.02.2023

Erste Gutachterin: apl. Prof. Dr.-Ing. Ursel Fantz

Zweiter Gutachter: apl. Prof. Dr. Helmut Karl

Contents

1 Introduction

Nuclear fusion is a source of renewable energy which has the potential to play a significant role in the global CO_2 neutral energy production of the future. The experimental reactor ITER (latin: *the way*) is currently being built in Cadarache, France, with the purpose of demonstrating the feasibility of nuclear fusion for energy production. Deuterium and tritium nuclei are fused to a helium nucleus and a single neutron within a magnetically confined high temperature plasma. The neutrons leave the plasma and can thus be used for energy production. Here, a temperature of 150 million °C needs to be maintained inside the plasma core as the positively charged nuclei need to overcome the Coulomb barrier in order to fuse. Therefore plasma heating methods need to be employed whereas one of them is NBI (**n**eutral **b**eam **i**njection) which also drives a plasma current which is relevant for the magnetic confinement. NBI is based on the injection of fast neutral hydrogen[1] atoms which transfer their energy to the plasma via collisions. After ionization, the particles are confined inside the plasma.

The ITER NBI which will deliver 33 MW of heating power is based on a negative ion source from which H^- ions are extracted from a low pressure low temperature plasma and accelerated to the required energy. Subsequently, the fast ions are neutralised in a chamber filled with H_2 gas via charge exchange collisions between ions and gas neutrals. The resulting neutral beam is injected into the fusion plasma. For the ITER NBI, a homogeneous H^- beam with an accelerated current of 46 A (D^-: 40 A), a total extraction area of $0.2\,\mathrm{m}^2$ and the kinetic energy of 0.87 MeV (D^-: 1 MeV) per ion is required. In addition, the current of unavoidably co-extracted electrons is to be kept below the ion current. Research and development are undertaken in order to achieve these goals simultaneously for the total ion source pulse length of 1 h (i. e. the maximum ITER pulse length).

The BATMAN Upgrade (BUG) test facility is used in order to investigate the formation, extraction and acceleration of negative hydrogen ions and the characterisation of the ion beam. This test facility is equipped with an ion source

---

[1] Denoting the isotopes hydrogen and deuterium.

of the size of 1/8 of the ITER negative ion source. The source operates after the tandem principle meaning that a low pressure low temperature plasma is generated with up to 100 kW of RF power via inductive coupling in a designated part of the source (the *driver*). Subsequently, the plasma expands towards a plasma facing grid (the *plasma grid*) while the electrons are cooled with the aid of a magnetic filter field leading to a reduced destruction of H^- via electron collisions. H^- is produced at the plasma grid surface via surface conversion of hydrogen atoms or positive ions. In the course of this, the plasma grid is covered with caesium in order to enhance the H^- production due to its low work function. Finally, H^- is extracted through the grid and accelerated using high voltage of up to 45 kV.

The conversion of H atoms is commonly regarded as the dominant H^- production process such that the flux of H^- into the source depends on the flux of H atoms towards the plasma grid (determined by H atom density n_H and temperature T_H) and the conversion yield (determined by T_H). n_H and T_H are thus important parameters for the ion source characterisation. At BUG, they are up to now measured indirectly with optical emission spectroscopy (OES) resulting in high error bars such that a direct determination of the density and temperature of H atoms is strongly desired. Thus, the general aim of this work is the implementation of *two-photon absorption laser induced fluorescence* (TALIF) at the ion source of BUG in the vicinity of the plasma grid as a direct method for the n_H and T_H determination. Here, ground state H atoms are excited into the $n = 3$ state via the simultaneous absorption of two photons at 205.08 nm and the subsequent fluorescence from the H_α transition at 656.3 nm is collected for the diagnostic. In order to generate the UV light at sufficient intensity, a pulsed dye laser is used and in addition, the whole diagnostic system consists of various further optics.

BUG operates in a harsh environment due to the high RF power and the applied high voltage such that the commissioning of a new diagnostic is cumbersome as the access to the experiment during plasma operation is not possible. Therefore, TALIF is first assembled and tested thoroughly at a small scale plasma experiment. The tests aim towards getting experience with the TALIF system, simulating the expected H density and investigating the influence of the used hydrogen isotope on the dissociation degree. Also a comparison of n_H to OES measurements is performed here. From the small scale experiment, the TALIF system is transferred to the ion source in a second step to gain the first results and demonstrate the application of TALIF at a H^- ion source for the very first time. Again, a comparison of the obtained n_H to OES is performed.

2 Low pressure low temperature plasmas for negative hydrogen ion sources

The plasmas within the negative ion source of BATMAN Upgrade as well as within the small-scale experiment that is used for the first TALIF implementation are considered *low pressure low temperature* (LPLT) plasmas. The following chapter deals with the properties of LPLT hydrogen plasmas and is based on [CB15, LL05]. In the latter part, the realization of negative hydrogen ion sources is elaborated. As the isotope hydrogen is predominantly used as carrier gas in laboratory experiments and teststands, the atomic and molecular properties are focussed on hydrogen. However, if not specifically stated otherwise, they also hold for the use of deuterium.

2.1 Low pressure low temperature plasma properties

A plasma can be created by the application of an electromagnetic field to neutral gas. Due to this field, naturally occurring free electrons are accelerated and collide with neutral particles which causes ionization and the formation of further ion-electron pairs. The newly formed electrons are in course accelerated by the electromagnetic field and the process starts again such that an *avalanche effect* occurs. Experimental plasma setups are distinguished by the method of generating the electromagnetic fields. Using alternating fields at radio frequency (RF) as in this work, two types can be differentiated. If the electromagnetic field is generated by a potential across the neutral gas, the plasma is considered as *capacitively coupled plasma* (CCP). On the other hand, if the electromagnetic field is induced by driving an alternating current in a coil in the vicinity of the plasma the plasma is considered as *inductively coupled plasma* (ICP). At the same pressure, CCPs can be operated at lower RF power and they are in general characterized by a lower electron density and a higher potential drop close to the edges of the plasma vessel [CS00, LL05].

Even though a plasma is driven inductively, the potential difference on the coil (up to several kV) can create electric RF fields in the plasma close to the coil which cause the presence of a CCP. The accompanying high voltage close to the edges of the plasma causes acceleration of positive ions towards the plasma vessel which might cause damage to the exposed parts. The formation of a CCP can be omitted by the use of a Faraday shield inserted between the coil and the plasma vessel. It is a grounded metal plate equipped with slits which are oriented parallel to the polarization of the induced electromagnetic field such that this field passes the shield unaffected. As the shield is grounded, the capacitive electric field terminate on the shield which suppresses the capacitive coupling [Hop94]. Both discharges which are evaluated in this work are ICPs. *Low pressure low temperature plasmas* are operated at low gas pressure (between 0.1 Pa and 100 Pa). ICPs at this pressure range exhibit a low ionisation degree (between 10^{-6} and 10^{-3}) and consequently, the electron density is low (between $10^{15}\,\mathrm{m}^{-3}$ and $10^{19}\,\mathrm{m}^{-3}$) [LL05].

If H_2 is used as gas species, the plasma consists of the neutral particles H and H_2, the positive ions H^+, H_2^+ and H_3^+, and the negatively charged particles H^- and electrons (e^-). On a global scale, the densities of positive and negative charges are equal such that no charged regions inside the plasma can form. This property is called *quasi-neutality.* Microscopically, quasi-neutrality can be violated on a length scale of

$$\lambda_{\mathrm{D,e}} = \sqrt{\frac{\epsilon_0 k_{\mathrm{B}} T_{\mathrm{e}}}{e^2 n_{\mathrm{e}}}}\,, \tag{2.1}$$

which is called electron *Debye length.* Here, ϵ_0 is the vacuum permittivity, k_{B} is the Boltzmann constant, T_{e} is the electron temperature, e is the electron charge and n_{e} corresponds to the electron density. Potentials that result from the violation of quasi-neutrality are shielded by the plasma within a few values of λ_{D}.

2.1.1 Distribution functions

A plasma species S can be characterized by its *velocity distribution function* (VDF) $f_{\mathbf{v},S}(\mathbf{r},\mathbf{v},t)$ at position $\mathbf{r} = (x,y,z)^\top$, velocity $\mathbf{v} = (v_x,v_y,v_z)^\top$ and time t. The quantity $f_{\mathbf{v},S}(\mathbf{r},\mathbf{v},t)\,\mathrm{d}^3r\,\mathrm{d}^3v$ is defined as the number of particles inside the phase space volume $\mathrm{d}^3r\,\mathrm{d}^3v$ at the phase space coordinate $(\mathbf{r},\mathbf{v})$ at time t [LL05]. The

VDF is normalized to the particle density via $n_S(\mathbf{r},t) = \iiint f_{\mathbf{v},S}(\mathbf{r},\mathbf{v},t)\,\mathrm{d}^3v$ and the mean kinetic energy of the particles $\langle E_S\rangle$ is given by

$$\langle E_S\rangle = \frac{m_S}{2\,n_S(\mathbf{r},t)} \iiint v^2 f_{\mathbf{v},S}(\mathbf{r},\mathbf{v},t)\,\mathrm{d}^3v\,. \tag{2.2}$$

The integration is to be carried out over the whole velocity space for each $\mathbf{v}$ component. m_S is the mass of the particle S and $v = \sqrt{v_x^2 + v_y^2 + v_z^2}$ is the absolute velocity.

Analogous to $f_{\mathbf{v},S}(\mathbf{r},\mathbf{v},t)$, the *energy distribution function* (EDF) $f_{E,S}(\mathbf{r},E,t)$ can be defined such that $f_{E,S}(\mathbf{r},E,t)\,\mathrm{d}E$ is the number of particles per unit volume within the kinetic energy interval $[E, E + \mathrm{d}E]$. It is normalized to the particle density via $n_S(\mathbf{r},t) = \int_0^\infty f_{E,S}(\mathbf{r},E,t)\,\mathrm{d}E$ and the mean kinetic energy of the particles can be expressed as

$$\langle E_S\rangle = \frac{1}{n_S(\mathbf{r},t)} \int_0^\infty E\, f_{E,S}(\mathbf{r},E,t)\,\mathrm{d}E\,. \tag{2.3}$$

Typically, $\mathbf{r}$ and t are omitted in the preceding equations if the distribution function is independent of the two parameters or the distribution function is evaluated locally. $f_{\mathbf{v},S}$ and $f_{E,S}$ are equivalent and the choice depends on the application for which the distribution function is evaluated.

In thermodynamic equilibrium the distribution functions are given by a *Maxwell-Boltzmann distribution*, where

$$f_{\mathbf{v},S}(\mathbf{v}) = n_S\left(\frac{m_s}{2\pi\,k_\mathrm{B}T_S}\right)^{3/2} \exp\left[-\frac{m_S(v_x^2+v_y^2+v_z^2)}{2\,k_\mathrm{B}T_S}\right] \text{ and} \tag{2.4}$$

$$f_{E,S}(E) = n_S\,2\sqrt{\frac{E}{\pi}}\left(\frac{1}{k_\mathrm{B}T_S}\right)^{3/2} \exp\left[-\frac{E}{k_\mathrm{B}T_S}\right]. \tag{2.5}$$

T_S is the temperature of the particle species S. In this case, the mean kinetic energy is given by $\langle E_S\rangle = \frac{3}{2}k_\mathrm{B}T_S$ and the mean velocity of the particle is given by $\overline{v_S} = \sqrt{\frac{8k_\mathrm{B}T_S}{\pi m_S}}$. In plasmas, specific mechanisms could cause the production of highly energetic particles and the loss of particles at a specific energy. Both lead to a deviation of the VDF or EDF from a Maxwell-Boltzmann distribution if the particle collision rate is not high enough to maintain thermalization within the particle lifetime. This is for example the case if the plasma is operated at low pressure where the collision rate is low. In those cases, the assignment of a temperature in the thermodynamic meaning is not possible as this requires the presence of a Maxwell-Boltzmann distribution. Instead, an effective temperature T_S^{eff} can be assigned which describes the mean kinetic energy after

$$\langle E_S \rangle = \frac{3}{2} k_{\mathrm{B}} T_S^{\mathrm{eff}} . \tag{2.6}$$

However, if a temperature is assigned to a particle species, its EDF is implicitly assumed to follow a Maxwell Boltzmann distribution in the remainder of this work.

In LPLT plasmas driven by an electromagnetic RF field, the driving power is mainly coupled to the electrons as they are able to follow the field due to their small mass. The electrons can transfer the energy to the heavy particles (neutrals and ions) via elastic collisions between the two particle species. The effectiveness of this transfer is limited due to the small electron density (between $10^{15}\,\mathrm{m}^{-3}$ and $10^{19}\,\mathrm{m}^{-3}$) in LPLT plasmas and the high mass difference between electrons and heavy particles limiting the energy exchange efficiency. This is why typically

$$\begin{aligned} \langle E_{\mathrm{e}} \rangle \gg \langle E_{\mathrm{n}} \rangle \approx \langle E_{\mathrm{i}} \rangle \ \text{ or} \\ T_{\mathrm{e}}^{\mathrm{eff}} \gg T_{\mathrm{n}}^{\mathrm{eff}} \approx T_{\mathrm{i}}^{\mathrm{eff}} . \end{aligned} \tag{2.7}$$

The indices n and i denote *neutrals* and *ions*. This is why LPLT plasmas are considered *non-thermal plasmas*. On the other side, the energy distributions of heavy particles can be approximated to be equal among all species which therefore also holds for their temperatures if the VDF follows a Maxwell-Boltzmann distribution. In this case, the common temperature is denoted as *gas temperature* T_{gas}. Typical values of $T_{\mathrm{e}}^{\mathrm{eff}}$ in LTLP plasmas are between 1 eV and 10 eV whereas effective neutral and ion temperatures range between room temperature and 10^{-1} eV.

2.1.2 Processes in plasmas

Due to the variety of plasma species multiple processes can occur in a plasma. Examples are ionization, dissociation and excitation of plasma particles. These can be described by the respective *reaction rate* which is the number of reactions per unit volume and time (in $\mathrm{m}^{-3}\mathrm{s}^{-1}$). The reactions creating a specific particle or state a (*sources*) can be balanced against the processes that lead to the destruction of the particle or state (*sinks*) in a balance equation

$$\frac{\mathrm{d}\,n_a}{\mathrm{d}t} = \overbrace{\sum_h R_h}^{\text{sources}} - \overbrace{\sum_j R_j}^{\text{sinks}}\,, \tag{2.8}$$

which links the temporal derivative of the density n_a of particle or state a with the sum of source (R_h) and sink (R_j) reaction rates. For an inelastic collision between the two particles a and b with the densities n_a and n_b, the reaction rate is given by

$$R = n_a \cdot n_b \cdot X_{\text{react}}\,. \tag{2.9}$$

X_{react} is the rate coefficient. It is given by $\langle \sigma_{\text{react}}(v_{\text{R}})\, v_{\text{R}} \rangle_{a,b}$, the average over all particles a and b of the product of the reaction cross section σ_{react} and the relative velocity of the two particles. In low pressure plasmas, collisions between heavy particles and electrons dominate the production and destruction of other particle species. In this case, the relative velocity is equal to the electron velocity. Thus, X_{react} can be expressed via [SVY12]

$$X_{\text{react}} = \int_0^\infty \sigma_{\text{react}}(E_{\text{e}}) \sqrt{\frac{2eE_{\text{e}}}{m_{\text{e}}}}\, \frac{f_{E,e}(E_{\text{e}})}{n_e}\, \mathrm{d}E_{\text{e}}\,, \tag{2.10}$$

if the electron energy E_{e} is given in eV. Otherwise, the elementary charge e is omitted. m_{e} is the electron mass and $f_{E,e}(E_{\text{e}})$ is the electron energy distribution function (EEDF). If the EEDF is given by a Maxwell-Boltzmann distribution, X_{react} is a function of T_{e}.

Plasma emission

A particle in an electronically excited state p may undergo a spontaneous transition into the energetically lower state q while emitting a photon with the wavelength [Tho88]

$$\lambda_{pq} = \frac{hc}{E_p - E_q}\,. \tag{2.11}$$

h is the Planck constant and c is the speed of light. E_p and E_q are the energies of the states p and q respectively. The reaction rate of the spontaneous emission is given by the emissivity [Tho88]

$$\frac{\mathrm{d}n_p}{\mathrm{d}t} = \epsilon_{qr} = n_p \, A_{pq} \, . \tag{2.12}$$

In this equation, n_p is the density of particles in state p and A_{pq} is the *Einstein coefficient* (in s^{-1}) which represents the transition probability. A_{pq} depends on the transition under investigation and can for example be found in [NIST] for various transitions of different neutral and ion species.

From one transition, photons are not emitted at only one fixed wavelength λ_0 determined by equation (2.11) but within a finite wavelength range. The shape of the wavelength distribution is denoted as *line profile* $g(\lambda)$ and is normalized after $\int_{\mathrm{line}} g(\lambda)\,\mathrm{d}\lambda = 1$. The line profile is determined by *broadening mechanisms* which are relevant in the plasma. For the plasmas and gases which are investigated in this work only two mechanisms are of relevance. These are *Doppler broadening* and *natural broadening.* This is due to the low gas pressure in the discharge omitting pressure broadening [MR02] and the low electron density below $10^{19}\,\mathrm{m}^{-3}$ omitting Stark broadening [vHBS+12]. Natural line broadening arises from the Heisenberg uncertainty principle. The finite lifetimes τ_q and τ_p of the lower and upper state result in a broadening of the energies of these states. The resulting *full width at half maximum* (FWHM) $\Delta\lambda_{\mathrm{nat}}$ is given by [Tho88]

$$\Delta\lambda_{\mathrm{nat}} = \frac{(\lambda_0)^2}{c} \left(\frac{1}{2\pi\tau_q} + \frac{1}{2\pi\tau_p} \right) . \tag{2.13}$$

The line profile induced by natural line broadening has the shape of a Lorentzian. The average lifetime of a state p is mainly determined by the decay via spontaneous emission such that $\tau_p = (\sum_q A_{pq})^{-1}$ where the latter is the sum over all possible transitions originating from state p.

Doppler broadening arises from the motion of the absorbing particles which shifts the emission wavelength depending on the particle velocity. If the particle motion is given by a Maxwell-Boltzmann velocity distribution function with temperature T, the FWHM $\Delta\lambda_{\mathrm{Dop}}$ is given by [Tho88]

$$\Delta\lambda_{\mathrm{Dop}} = \frac{\lambda_0}{c} \sqrt{\frac{8\,\ln(2)\,k_{\mathrm{B}}\,T}{m}} \, . \tag{2.14}$$

Here, m is the particle mass. In this case, the line profile has the shape of a Gaussian. The combination of both broadening mechanisms is given by the convolution of the two respective line profiles resulting in a Voigt profile. Typically,

$\Delta\lambda_{\mathrm{nat}} \ll 1\,\mathrm{pm}$ while $\Delta\lambda_{\mathrm{Dop}} > 1\,\mathrm{pm}$ such that Doppler broadening dominates the resulting line profile.

Ionization balance

Positive ions are predominantly produced via electron impact ionization and are lost due to diffusion towards the plasma vessel walls and subsequent recombination [Beh91]. These two processes can be used for a global ionization balance after equation (2.8). For this, however, it is assumed, that only one neutral species (density: n_0) and one ion species (density: n_{i}) at a common temperature T_0 are present in the plasma. Electrons are assumed to be the only negatively charged species and a Maxwellian EEDF at temperature T_{e} is assumed while $n_{\mathrm{e}} = n_{\mathrm{i}}$.

The diffusion of positive ions towards the vessel wall is characterized by the collective behaviour of ions and electrons. If one of the species is diffused, the other follows due to maintaining quasi-neutrality in the plasma and vice versa. This is called *ambipolar diffusion*. At sufficient pressure, such that the mean free path for ions $s^+_{\mathrm{mfp}} = (\sqrt{2}n_0\sigma_{\mathrm{hs}})^{-1}$ is smaller than the characteristic length of the plasma, diffusion can be treated according to [Möl93]. σ_{hs} is the collision cross section for positive ions and neutral particles after the hard sphere model and the characteristic length is defined as the ratio of the plasma volume to the plasma surface. In this case, the diffusion time is given by

$$\tau_{\mathrm{diff}} \propto \frac{T_0}{T_{\mathrm{e}}}\,(s^+_{\mathrm{mfp}})^{-1}\sqrt{\frac{m_i}{k_{\mathrm{B}}T_0}}\,, \tag{2.15}$$

where m_i is the ion mass. Equation (2.8) is 0 in steady state, such that

$$n_{\mathrm{e}}\,n_0\,X_{\mathrm{ion}}(T_{\mathrm{e}}) = \frac{n_i}{\tau_{\mathrm{diff}}} \tag{2.16}$$

for the ionization balance. Here, the left side denotes the electron impact ionization and $X_{\mathrm{ion}}(T_{\mathrm{e}})$ is the corresponding rate coefficient calculated according to equation (2.10). Solving for $X_{\mathrm{ion}}(T_{\mathrm{e}})$, assuming quasi-neutrality ($n_i = n_{\mathrm{e}}$) and inserting equation (2.15) yields

$$X_{\mathrm{ion}}(T_{\mathrm{e}}) \propto \frac{s^+_{\mathrm{mfp}}}{n_0\sqrt{m_i}}\,. \tag{2.17}$$

From this, the plasma behaviour for varying pressure can be predicted. First, decreasing pressure leads to a n_0 drop and a s^+_{mfp} rise due to its n_0 dependence. Essentially, the loss of positive ions at the vessel wall becomes stronger. In order to compensate that loss, T_e must increase as it enhances the ion production rate. Secondly, a higher ion mass slows down the diffusion to the walls such that a lower T_e value is sufficient in order to satisfy the ionization balance. Thirdly, having particles with a low ionization potential (which is connected to a high ionization cross section) also decreases the T_e value due to the same reason.

Power balance

The power that is supplied to the plasma is mainly absorbed by the electrons. From those, the power is dissipated via excitation, ionization or dissociation of the neutral species j. Following [Beh91], a balance of the external power P_ext per volume V can be set up. This is

$$\begin{aligned}\frac{P_\mathrm{ext}}{V} &= \frac{P_\mathrm{exc}+P_\mathrm{ion}+P_\mathrm{diss}}{V}\\ &= n_\mathrm{e}\cdot\sum_{j,i} n_{j,0}\,E^{j,i}_\mathrm{exc}\,X^{j,i}_\mathrm{exc}(T_\mathrm{e}) && \longleftarrow \text{ excitation}\\ &\quad + n_\mathrm{e}\cdot\sum_{j,k} n_{j,0}\,E^{j,k}_\mathrm{ion}\,X^{j,k}_\mathrm{ion}(T_\mathrm{e}) && \longleftarrow \text{ ionization}\\ &\quad + n_\mathrm{e}\cdot\sum_{j,l} n_{j,0}\,E^{j,l}_\mathrm{diss}\,X^{j,l}_\mathrm{diss}(T_\mathrm{e})\,. && \longleftarrow \text{ dissociation}\end{aligned} \tag{2.18}$$

Here, $n_{j,0}$ is the density of species j. $E^{j,i}_\mathrm{exc}$ and $X^{j,i}_\mathrm{exc}$ are the excitation energy and the excitation rate coefficient for electron excitation of species j into state i including vibrational and rotational excitation in the case of molecules. $E^{j,k}_\mathrm{ion}$ and $X^{j,k}_\mathrm{ion}$ are the ionization potential and the electron impact ionization rate coefficient of the ionization stage k of species j. Finally, $E^{j,l}_\mathrm{diss}$ and $X^{j,l}_\mathrm{diss}$ are the dissociation energy and the electron impact dissociation rate coefficient for the dissociation process l of species j in the case that j is a molecular species.

The values for E are constants and the rate coefficients are also constant as long as the pressure in the plasma does not change. In the latter case, this holds also for $n_{j,0}$. Thus, a sole increase of the power coupled to the plasma leads to an increase of n_e as it is the only remaining variable. In the case that j is a molecular species, vibrational excitation (with comparably high excitation cross section) is possible acting as an additional sink of the power. This means, that only a smaller share of the input power is available for ionization leading to lower electron densities for plasmas which contain a high share of molecular species.

2.1.3 Plasma sheath

A plasma is usually surrounded by a metallic wall at a fixed electric potential. This could be ground potential in the case of small laboratory plasma experiments or negative high voltage in the case of negative ion sources to extract the ions against ground potential. When charges flow onto the wall, they get absorbed and result in a current to the connected electric network. The wall acts therefore as a sink for positive and negative charges. As the electron temperature exceeds the positive ion temperature and in addition the electron mass is much lower, the average electron velocity $\overline{v_\mathrm{e}}$ and the electron flux $\Gamma_\mathrm{e} = \frac{1}{4} n_\mathrm{e} \overline{v_\mathrm{e}}$ towards the wall is much larger compared to positive ions. In this case, electrons would be drained from the plasma leading to a violation of quasi-neutrality.

This causes the plasma to be positively charged compared to the wall which leads to a potential difference between the *plasma potential* Φ_pl and the surrounding walls (at wall potential Φ_wall). This potential difference acts decelerating on electrons and accelerating on positive ions. The region in which this happens, is called *plasma sheath*. The potential difference forms in such a way that the total currents from, towards or inside the wall are balanced globally. However, local net currents to or from the surrounding wall are possible.

The influence of this on the positive/negative ion and electron density n_i and n_e as well as the profile of the electric potential in the plasma is depicted in figure 2.1. Close to the wall, in the sheath region, the potential drops sharply. This leads to a drop of n_e relative to n_i which means that the sheath plasma is charged positively in this region. The sheath length is typically on the order of several values of $\lambda_\mathrm{D,e}$. Negative ions as present in a negative ion source plasma are neglected in this treatment. Their influence on the potential and density distribution in the sheath is for example discussed in [DR92, SWM20].

A smaller potential drop occurs already further inside the plasma. This happens since the *Bohm criterion* requires positive ions to enter the sheath already at some minimal velocity which is called the *Bohm velocity*. The acceleration of the positive ions happens due to this small potential drop and the region in which this happens in denoted as *presheath*. In the presheath, $n_\mathrm{i} = n_\mathrm{e}$ is still valid. The presheath width depends on the ion mean free path and is typically on the order of a few mm in LPLT plasmas. Further away from the wall, in the bulk plasma, $n_\mathrm{i} = n_\mathrm{e} = \mathrm{const}$ and also the electric potential is constant.

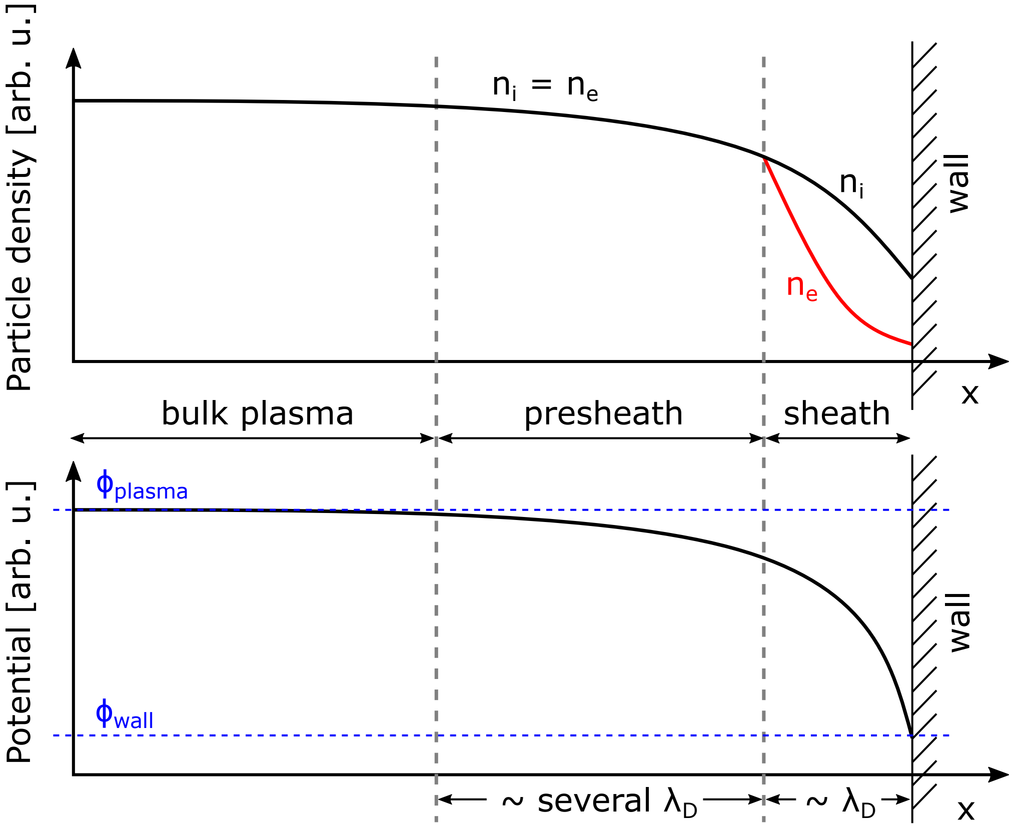

Figure 2.1: *Electron and positive ion densities as well as electric potential profile close to a vessel wall. Figure after [LL05].*

2.2 Atomic and molecular properties of hydrogen

2.2.1 Electronic states and transitions of the hydrogen atom

A hydrogen atom consists of one proton and one electron. The behaviour of the electron within the Coulomb potential of the proton is characterized by its electronic state which can be described by its quantum numbers [Dem05]. Considering only *fine structure* effects and not having a magnetic field, the quantum numbers n, l, j and m_j which are defined in table 2.1 are sufficient for describing the electronic state. With these, the binding energy of the electron with quantum numbers n and j is given by

$$E_{nj} = -\frac{E_R}{n^2} \cdot \left[1 - \frac{\alpha^2}{n} \left(\frac{1}{j + 1/2} - \frac{3}{4n} \right) \right] . \tag{2.19}$$

Table 2.1: *Necessary quantum numbers in order to characterize an electronic state of the hydrogen atom considering fine structure.*

Symbol	Name	Possible values for H
n	principal quantum number	$n \in \mathbb{N}$
l	angular momentum quantum number	$l \in \{0, \dots, n-1\}$
j	total angular momentum quantum number	$j \in \{\lvert l - 1/2 \rvert, l + 1/2\}$
m_j	magnetic total angular momentum quantum number	$m_j \in \{-j, \dots, j\}$

Here, E_R is the *Rydberg energy* which has the value $E_R = 13.6\,\mathrm{eV}$, α is the *Sommerfeld fine structure constant* with $\alpha \approx 1/137$. The negative value of E_{nj} denotes that the electron in the corresponding state needs the absolute value of E_{nj} to leave the protons Coulomb potential.

A hydrogen state can be assigned by the term symbol

$$n^2 l_j\,.$$

In this formalism, l denotes the value of the angular momentum quantum number. Instead of L, the letters S ($l = 0$), P ($l = 1$), D ($l = 2$), F ($l = 3$), ... are written when assigning a state. Each state is split into further sub-states according to their value of m_j. The number of sub-states corresponds to the number of possibilities for electrons to occupy the state n^2L_j. It is denoted as statistical weight and is given by $g = 2j + 1$. With an external magnetic field, the energy of each sub-state splits up.

Electric dipole transitions between hydrogen states p and q can occur via the emission or absorption of photons. The wavelengths of the corresponding photons can be calculated by using the equations (2.11) and (2.19). However, the corresponding transition needs to follow the transition rules which are derived in [Tho88]. They are given by

Table 2.2: *Designation of the hydrogen atom transition series and spectral regions of the lines α to δ*

Name	n (lower)	Spectral region (α to δ)
Lyman	1	95 nm – 122 nm
Balmer	2	410 nm – 656 nm
Paschen	3	1005 nm – 1875 nm
Brackett	4	1945 nm – 4053 nm

$$\begin{aligned} \Delta l &= \pm 1 \quad \text{and} \\ \Delta j &= 0, \ \pm 1\,. \end{aligned} \tag{2.20}$$

Δl and Δj are the change of the angular momentum quantum number and the total angular momentum quantum number.

The transitions of the hydrogen atom are ordered in *series* after the principal quantum number of the energetically lower lying state. Within a series, the transition lines are designated with Greek letters starting with α with ascending value of the principal quantum number of the upper state. The names and the spectral regions of the first four series are shown in table 2.2. The lines of the Balmer series are referred to as H_α, H_β, ... and so on. For deuterium, the corresponding transitions lie at slightly lower wavelengths. This is due to the dependence of E_R on the reduced mass of the electron-core system which changes due to the additional neutron in the deuterium core. The resulting deviation of the wavelength is, however, on the order of the first decimal place.

2.2.2 Electronic states and transitions of the hydrogen molecule

In addition to electronic excitation, H_2 can store energy in rotation and the relative motion of the two hydrogen atoms, i. e. vibration. These two degrees of freedom are quantized and exhibit additional internal energy levels. One state characterized by its electronic, vibrational and rotational level is called a *ro-vibronic state.* A small overview over the structure of H_2 molecules is given in the following, for further information [Her50] is recommended.

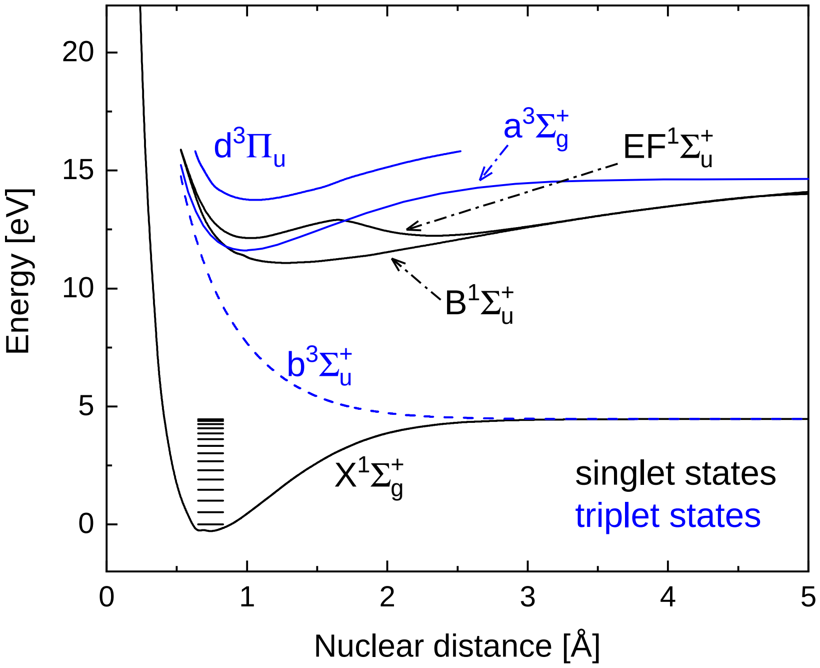

Figure 2.2: *Potential diagram of various states of the* H_2 *molecule after [Sha70, Sha71] with the vibrational levels of the ground state after [FW06].*

The potential energy as a function of internuclear distance between the two H atom cores for several molecular electronic states after [Sha70, Sha71] is depicted in figure 2.2. Here, the energy curves are shifted vertically in such a way that the value 0 corresponds to the energy of the H_2 ground state in its vibrational ground state. The electronic states are grouped in *triplet* and *singlet* states depending on the value of the total electron spin S of the two electrons (singlet: $S = 0$, triplet: $S = 1$). No electric dipole transitions are possible between these two groups. The H_2 ground state is denoted as $X^1\Sigma_g^+$ and the first excited state is $b^3\Sigma_u^+$. The latter state is *anti-bonding* such that the potential drops monotonically for increasing internuclear distance. Molecules in that state dissociate immediately and form two ground state H atoms.

In figure 2.2, the state $X^1\Sigma_g^+$ is assigned with its vibrational levels after [FW06]. Vibrational excitation is characterized by the vibrational quantum number $\nu \in \mathbb{N}_0$. Each vibrational state exhibits rotational levels which are characterized by the rotational quantum number $N \in \mathbb{N}_0$.

The population of vibrational levels can be caused by direct excitation via molecule-electron collisions or relaxation from electronically excited molecules prior excited via electron excitation. Out of the two processes, the second one is considered to be more efficient [JRS03]. Another process is the recombination of H atoms at the plasma vessel walls. Vibrational excitation via the collision of H_2 with other heavy particles is ineffective. This is due to the energy difference between two neighbouring vibrational levels on the order of $0.5 \div 0.1\,\mathrm{eV}$ which is bigger than the typical gas temperature at $\sim 0.05\,\mathrm{eV}$ ($= 600\,\mathrm{K}$). Heavy particle collisions rather cause a depopulation of high ν states [FH98]. If the population of the vibrational levels is given by a Boltzmann distribution, the according vibrational temperature is denoted as T_{vib}. Such a distribution is often present in LPLT plasmas as is for example shown in [FH98].

In contrast, the population of the rotational levels is predominantly caused by inelastic collisions between H_2 and other heavy particles. These are more efficient here as the energy difference between two neighbouring rotational levels is on the order of $0.01\,\mathrm{eV}$. Collisions of electrons with molecules cause no momentum transfer due to their high mass difference such that no change of N occurs [OOR+89]. In the case of a Boltzmann distribution among the rotational level population, the rotational temperature T_{rot} is assigned. Experimentally, a two-temperature distribution among the rotational states is often observed [VSE04, BRF17, BF18] with a “cold” and a “hot” temperature. The cold temperature corresponds to the gas temperature T_{gas} [BRF17].

For electric dipole transitions between different ro-vibronic states, the change in ν is arbitrary. They are, however, restricted regarding the change in N between the energetically upper state i and the lower state f to $\Delta N = N_f - N_i = 0, \pm 1$, while transitions between two states with $N = 0$ is forbidden. Depending on the value of ΔN the transitions can be grouped in branches. They are called P, Q and R branch for $\Delta N = -1, 0, +1$. The electronic state must change in the course of an electric dipole transition since the H_2 molecule consists of two equal atoms (*homonuclear*) omitting pure vibrational and rotational transitions. A transition system which is used for diagnostic purposes is the *Fulcher-α* system which consists of multiple transitions between the ro-vibronic states of the triplet states $d^3\Pi_u$ and $a^3\Sigma_g^+$. In this work, the Q branch of the first four diagonal vibrational transitions ($\nu'' = \nu' \in [0, 3]$) is investigated. The corresponding lines are between 590 nm and 650 nm.

For the D_2 molecule, the electronic states do not change compared to hydrogen. However, due to the higher mass, neighbouring vibrational and rotational levels are closer [Die58, FW06]. This changed structure causes that the investigated part of the Fulcher system spreads over a more narrow wavelength range from 595 nm to 635 nm.

2.3 Processes in hydrogen plasmas

Hydrogen LPLT plasmas contain a variety of plasma species and are exposed to walls surrounding the discharge. This leads to multiple possible processes which are partly described in chapter 2.1.2 in general. Additional processes are charge and particle transfer, attachment, detachment, recombination and association. These processes can occur isolated or in reaction chains both in the plasma volume and at the vessel walls. A review of collision processes which can occur in a hydrogen plasma volume is given in [JRS03].

The relevance of a particular reaction for the production/destruction of a particular particle species depends predominantly on the temperature and density of the plasma particles. This is for example described in [WF16b], where mainly two regimes depending on T_e are described, the *ionizing* plasma ($T_\mathrm{e} >$ a few eV) and the *recombining* plasma ($T_\mathrm{e} \leq 1\,\mathrm{eV}$). In an ionizing plasma, the excitation of hydrogen atoms is mainly driven by collisions of H atoms and H_2 molecules with electrons, whereas in recombining plasmas, this is due to (dissociative) recombination or mutual neutralization of one of the four ion species. In this work, the generation of hydrogen atoms as well as the processes involving H^- are of special relevance. This is why these processes are introduced in detail in the following.

2.3.1 Production and destruction of hydrogen atoms

Electron impact dissociation

The energy that is necessary for the dissociation of a ground state H_2 molecule is 4.5 eV [Sha70, Sha71]. The temperature of heavy particles is far below that value such that the excitation of H_2 molecules via heavy particle collisions is unlikely. Therefore the main process of dissociation is the excitation of H_2 molecules into the anti-bonding $b^3\Sigma_u^+$ state by electron impact:

$$\mathrm{H_2(X^1\Sigma_g^+) + e^- \longrightarrow H_2(b^3\Sigma_u^+) + e^- \longrightarrow H}(n=1) + \mathrm{H}(n=1) + \mathrm{e^-}\,. \tag{2.21}$$

From figure 2.2 is apparent that the excitation of ground state H_2 molecules requires more energy than the dissociation energy. The difference of the excitation energy and the dissociation energy is released evenly distributed as kinetic energy of the two formed H atoms. This energy is denoted as *Franck-Condon energy* and has a value of roughly 2 eV for the dissociation of ground state H_2. If a molecule is excited towards another anti-bonding state which has an even higher potential, dissociation into one excited and one ground state H atom is possible. This process is called *dissociative excitation.*

Cross sections of electron impact dissociation were calculated in [SFK+21] depending on the vibrational level and the hydrogen isotope. A significant difference of the absolute value of the cross sections for hydrogen and deuterium was not revealed. However, the difference concerning their vibrational levels and their respective population could lead to varying dissociation rates.

Wall recombination

Positive ions can be neutralized at the plasma vessel walls via Auger-Meitner neutralization [HKO78] and form neutral H atoms. These are eventually reflected back into the plasma. The formation of H atoms at the wall can involve the positive ions H^+, H_2^+ and H_3^+ such that one, two or three H atoms can be formed from one ion respectively [Phe09, Phe10]. The probability of this reaction is determined by the *particle reflection coefficient* and the share of the incident energy which remains at the H atom as kinetic energy is given by the *energy reflection coefficient.* Both coefficients depend on the wall material, the incident energy and the angle between the ion trajectory and the wall. In [EB85], those coefficients are calculated for H and D atoms hitting nickel, carbon and tungsten walls. Their values range from below 10^{-4} up to 90 % depending on the incident energy.

When approaching the wall, the positive ions get accelerated while crossing the sheath by the electric potential difference between plasma and vessel wall prior to neutralization. Thus, fast H atoms with kinetic energies up to a few eV can be produced [Koh15]. Further, the impact of fast ions on the vessel walls causes sputtering of the wall material into the plasma.

Destruction of H atoms

The recombination of H atoms at the plasma vessel walls is the dominant loss channel for H atoms in low pressure low temperature hydrogen plasmas. The H atoms are transported to the walls via diffusion such that the loss rate K_{loss} (in s^{-1}) of the H atoms in the plasma volume is given by [LL05]

$$K_{\text{loss}} = \left(\overbrace{\frac{\Lambda_0^2}{D_{\text{H},\text{H}_2}}}^{\substack{\text{diffusion}\\\text{time}}} + \overbrace{\frac{2-\gamma}{\gamma\, v_{\text{th}}} \frac{V}{S}}^{\substack{\text{wall}\\\text{recombination}\\\text{time}}} \right)^{-1} . \tag{2.22}$$

In this equation, Λ_0 is the *mean diffusion length* which is closely described in [Möl93], D_{H,H_2} is the diffusion coefficient of H atoms due to collisions with H_2 molecules. V is the volume and S is the surface of the plasma vessel. v_{th} is the thermal velocity of the H atoms and molecules assuming that both species have the same temperature. γ is the probability at which the atoms are lost at the wall due to recombination. This parameter depends heavily on the considered surface whereas stainless steel has a value of $\gamma = 0.1$ for example [MM71, MDZ99].

The equation consists of the diffusion term and the recombination term. Depending on the pressure range, one of the two dominates over the other. At high pressure, diffusion is the rate limiting process of the total process such that the diffusion term is dominating the equation. At low pressure, the flow of H atoms can not be considered diffusive meaning that the H atoms flow freely towards the wall which omits the assumptions made for the above equation. This is the case if the mean free path of the H atoms is on the same order or exceeds the plasma vessel dimensions. Yet the equation is considered reliable as the wall recombination term becomes dominant [Cha87].

The diffusion of H atoms due to collisions with H_2 molecules is considered as *free diffusion* and D_{H,H_2} is given by

$$D_{\text{H},\text{H}_2} = \frac{3\sqrt{\pi}}{8} s_{\text{mfp}}^{\text{H}} \sqrt{k_{\text{B}} T_{\text{gas}} \frac{m_{\text{H}} + m_{\text{H}_2}}{2 m_{\text{H}} m_{\text{H}_2}}} . \tag{2.23}$$

Here, $s_{\text{mfp}}^{\text{H}}$ is the mean free path of H atoms and m_{H} and m_{H_2} are the masses of H atoms and H_2 molecules respectively. Applying this formula to deuterium yields that the diffusion constant for deuterium is smaller compared to hydrogen by 30 %. This causes a lower wall recombination rate for D atoms.

2.3.2 A dissociation model for hydrogen

The multitude of production and loss mechanisms of both hydrogen atoms and the positive ion species can be modelled by solving the corresponding balance equations. That can be used in order to calculate the densities of H atoms, H^+, H_2^+ and H_3^+ ions in a discharge at known plasma parameters. Such a calculation is

Table 2.3: *Reactions considered for the dissociation model [Bri22] for the calculation of the H atom density as well as the* H^+*,* H_2^+ *and* H_3^+ *densities.*

Dissociation model			
Diffusion	H, H^+, H_2^+, H_3^+	$\longrightarrow$	wall
Wall recombination	H^+	$\xrightarrow{\text{wall}}$	H
Wall recombination	$H_2^+, 2\,H$	$\xrightarrow{\text{wall}}$	H_2
Wall recombination	H_3^+	$\xrightarrow{\text{wall}}$	$H_2 + H$
Electron impact dissociation:	$H_2 + e^-$	$\longrightarrow$	$2\,H + e^-$
Electron impact ionisation:	$H_x + e^-$	$\longrightarrow$	$H_x^+ + 2\,e^- \quad (x \in \{1, 2\})$
Dissociative ionisation:	$H_2 + e^-$	$\longrightarrow$	$H + H^+ + 2\,e^-$
Recombination (radiative & three-body):	$H^+ + e^- (+e^-)$	$\longrightarrow$	H
Dissociative recombination:	$H_2^+ + e^-$	$\longrightarrow$	$2\,H$
Electron impact dissociation:	$H_2^+ + e^-$	$\longrightarrow$	$H + H^+ + e^-$
Electron impact dissociation:	$H_2^+ + e^-$	$\longrightarrow$	$2\,H^+ + 2\,e^-$
H_3^+ production:	$H_2^+ + H_2$	$\longrightarrow$	$H_3^+ + H$
Dissociative recombination:	$H_3^+ + e^-$	$\longrightarrow$	$3\,H$
Dissociative recombination:	$H_3^+ + e^-$	$\longrightarrow$	$H + H_2$
Electron impact dissociation:	$H_3^+ + e^-$	$\longrightarrow$	$H^+ + 2\,H + e^-$
Charge exchange collision:	$H^+ + H_2$	$\longrightarrow$	$H + H_2^+$

performed within a *dissociation model* [Bri22]. The reaction rates depend on the electron temperature T_e, electron density n_e and the temperature of heavy particles T_{gas} which are necessary as input parameters for the model calculations. For the calculation, the balance equations for each species are solved for equilibrium. This is done with the same method as for the CR models Yacora H and H_2 (see chapter 2.4.2), such that detailed information on the calculation of the solution to the balance equations can be found in [WF16b]. The considered processes are depicted in table 2.3. The diffusion of H atoms and the positive ions is treated following the equations (2.22) and (2.23) such that the geometry of the plasma vessel needs to be considered in the model calculations. The wall loss coefficient γ is chosen according to the experimental conditions (i. e. the relevant surface). The model is used in this work in order to predict the H atom density in the plasma from known plasma parameters n_e, T_e and T_{gas}.

2.3.3 Production and destruction of negative hydrogen ions

The production of negative hydrogen (and deuterium) ions in ion source plasmas is mainly determined by two processes, volume production and surface production [BW20].

Volume production

The main production mechanism in the plasma volume is the *dissociative attachment* where collisions of electrons with ground state H_2 molecules produce negative ions via the formation of a metastable H_2^- ion [Bac06]:

$$H_2(X^1\Sigma_g^+, \nu) + e^- \longrightarrow H_2^- \longrightarrow H^- + H\,. \tag{2.24}$$

ν denotes the vibrational quantum number. The rate coefficient of this process raises strongly for rising electron temperature T_e and is strongly increased for high vibrational quantum number. If $\nu \geq 5$ for H_2 and $\nu \geq 8$ for D_2, the H_2^- formation threshold lies below 1 eV and even cold electrons ($T_e \leq 1\,\text{eV}$) produce significant H^- densities. The formation of vibrationally excited H_2 molecules can occur via electron impact excitation which is inefficient such that a high collision rate between H_2 and e^- is desired. The required elevated electron and H_2 densities can be achieved with high pressure. Further, vibrationally excited H_2 molecules can be generated via the relaxation from electronically excited molecules which requires high electron temperature ($T_e \geq 20\,\text{eV}$) to prior excite these molecules [Bac06].

Surface production

Additionally, H^- ions can be produced at plasma facing metal surfaces via the *surface conversion* of H atoms and various positive ion species:

$$H + e^-_{\text{surf}} \longrightarrow H^- \quad \text{and} \tag{2.25}$$

$$H_x^+ + 2\,e^-_{\text{surf}} \longrightarrow H^- + H_{x-1}\,,\ x = 1,2,3\,. \tag{2.26}$$

Ions that are close to the surface are neutralized when approaching it via Auger-Meitner neutralization such that they can be treated as H atoms [HKO78, RWL82]. The conversion process for H atoms is illustrated in figure 2.3. When the atom comes close to a metal surface, the affinity level for forming a H^- ion is lowered due

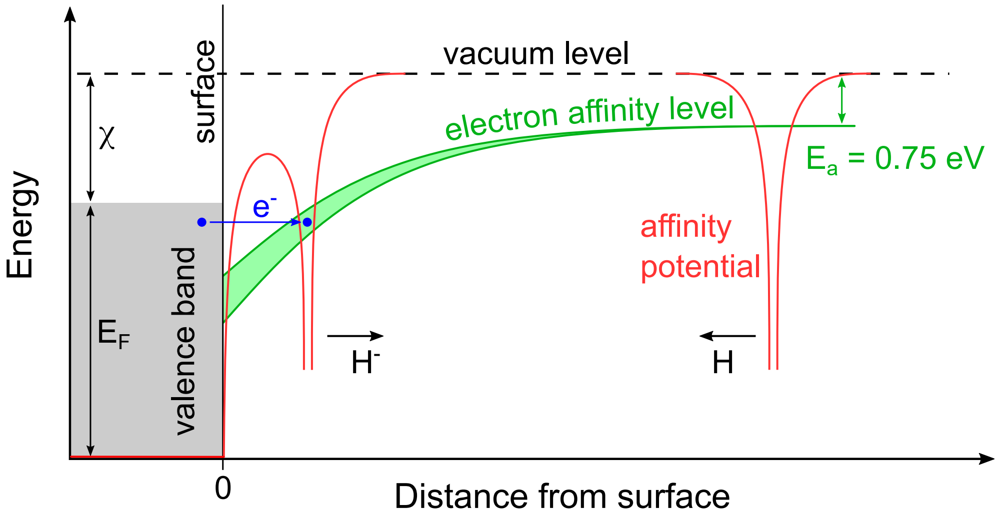

Figure 2.3: *Visualization of the surface conversion of H atoms to* H^- *ions.* E_F *is the Fermi energy of the surface material and* χ *its work function.* E_a *is the vacuum electron affinity of the approaching H atom. Picture after [RWL82].*

to the induction of a positive image charge in the metal surface. As soon as the affinity level is close to the valence band of the metal, electron tunnelling between the valence band and the affinity level starts occurring. This leads to a finite lifetime of the electron in the affinity level which in turn causes broadening of said level. The particle gets reflected at the surface while the tunnelling continues.

The probability that the particle eventually leaves the surface as H^- ion depends on the electron affinity $E_a = 0.75\,\mathrm{eV}$ far away from the surface, the surface *work function* χ and the velocity v_{H^-} of the negative ion leaving the surface. In [RWL82], the negative ion *conversion yield* β^- from impinging H atoms was calculated from the overlap of the valence band of the metal surface and the affinity level. In the limit of low v_{H^-}, it is

$$\beta^- \simeq \frac{2}{\pi} \cdot \exp\left(-\frac{\pi}{2}\,\frac{\chi - E_a}{a\,v_{H^-}}\right), \tag{2.27}$$

which was also derived earlier by [BNH76]. a is an exponential decay constant. From this it is apparent that a high conversion yield is directly related to a low work function of the metal wall. This is why H^- ion sources based on surface conversion use the alkali metal caesium (Cs), i. e. the element with the lowest work function of 2.14 eV, to cover the conversion surface which lowers its work function [BDD74].

The negative ion conversion yield was calculated more thoroughly in [Cui91, SCI+96] for the conversion of H atoms and measured in [IKS92, SCI+96] for the

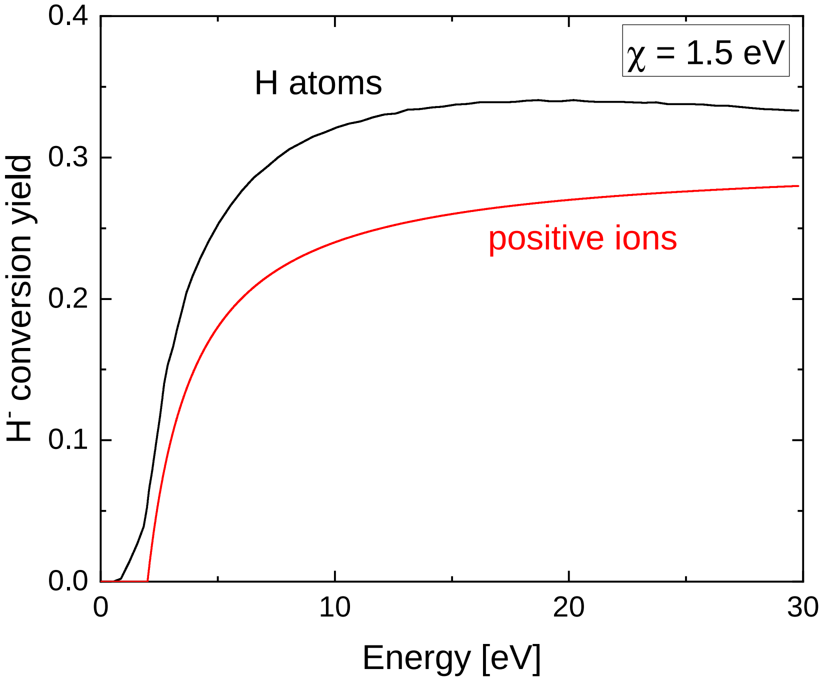

Figure 2.4: *H^- conversion yield for impinging H atoms and positive ions as function of the incident energy. For the positive ions, both energy and conversion yield are considered as value per nucleus. Figure after [SCI+96]*

conversion of positive ion species. The results of these investigations are depicted in figure 2.4. For positive ions, the y and x axis depict both conversion yield and energy *per nucleus* such that the same figure can be used for the conversion of either of the three ion species H^+, H_2^+ and H_3^+. The work function of the converter surface of both calculation and measurement is 1.5 eV which is lower than the value reached by bulk Cs, but it can be reached under certain circumstances (low Cs coverage [Wil66a, Wil66b, SS68] or the development of Cs oxides on the surface [UJ70]).

Using these values of β^-, the particle flux Γ_{H^-} of H^- ions leaving the surface can be evaluated from a given one dimensional velocity distribution function $f_{v_x,A}(v_x)$ of H atoms or positive ions in the vicinity of the converter surface:

$$\Gamma_{H^-} = \int_0^\infty f_{v_x,A}(v_x)\, v_x\, \beta^-(v_x)\, \mathrm{d}v_x\,. \tag{2.28}$$

v_x denotes the velocity perpendicular to the converter surface while positive values of v_x mean motion towards the surface. $f_{v_x,A}(v_x)$ is defined as the integral of $f_{\mathbf{v},A}(\mathbf{v})$ over the v_y and v_z axis. $f_{v_x,A}(v_x)\mathrm{d}v_x$ corresponds to the density of particles within the velocity interval $[v_x, v_x + \mathrm{d}v_x]$. A denotes the particle species that is converted into negative ions.

Destruction processes

On the other hand, H^- can be destroyed by several processes in the plasma. These are [FFK+07]:

- **Electron stripping**: $H^- + e^- \longrightarrow H + 2\,e^-$
  The dependence of this process on T_e is very steep such that for $T_e > 2\,\mathrm{eV}$, electron stripping is the most significant destruction mechanism of negative ions in negative ion sources.
- **Mutual neutralization**: $H^- + H^+ \longrightarrow H + H$,
  $H^- + H_2^+ \longrightarrow H_2 + H$ and
  $H^- + H_3^+ \longrightarrow H_2 + H + H$
  The rate coefficient of this process varies only slightly with ion temperature. For low T_e, mutual neutralization becomes the dominant destruction mechanism.
- **Associative Detachment**: $H^- + H \longrightarrow H_2 + e^-$ and
  Collisional Detachment: $H^- + H, H_2 \longrightarrow H + H, H_2 + e^-$
  The rate coefficients of these reactions are smaller than the mutual neutralization rate coefficient by at least one order of magnitude. However, due to the high density of H and H_2 the contribution is as dominant as the mutual neutralization.

2.4 Optical emission spectroscopy for the determination of plasma parameters

Optical emission spectroscopy (OES) is a non-invasive and line integrating tool in order to measure the spectrally resolved emission of a plasma. This information can be used in order to determine the line-of-sight integrated plasma parameters n_e, T_e, n_H and T_{gas}. Its use as a diagnostic is described in detail in [Fan06]. As the designation of a *temperature* hints, the investigated energy distribution functions are assumed to follow a Maxwell-Boltzmann distribution.

A spectrometer consists of a dispersive element (e. g. a grating) which divides light into its spectral parts and an optical detector which records the light intensity as a function of wavelength (e. g. a camera). In order to determine absolute values for the emissivity ϵ_i of a single spectral line i, the spectrometer needs to be calibrated with the aid of a calibration standard. With this,

$$\epsilon_i = \frac{1}{l_{\mathrm{pl}}\, t_{\mathrm{exp}}} \cdot \int\limits_{\mathrm{line}} C_i(\lambda) S_i(\lambda)\, \mathrm{d}\lambda\,, \tag{2.29}$$

where l_{pl} is the plasma length, i. e. the length of the LOS in the plasma, t_{exp} is the exposure time of the optical detector, $C_i(\lambda)$ is the wavelength dependent calibration factor and $S_i(\lambda)$ is the spectrometer signal (in counts). The calibration is performed by using a secondary calibration standard which emits radiation with a known spectral intensity. $C_i(\lambda)$ is obtained by dividing the specified emission from the secondary calibration standard by the measured signal. In this work, the emissivities of the H atom Balmer lines α to ϵ (denoted as $\epsilon_{\alpha-\epsilon}$) as well as the H_2 Fulcher-α system are investigated spectroscopically.

2.4.1 Spectroscopy on the H_2 Fulcher-α transition

The Fulcher-α system $\mathrm{d}^3\Pi_{\mathrm{u}}(\nu', N') \longrightarrow \mathrm{a}^3\Sigma_{\mathrm{g}}^+(\nu'', N'')$ is measured in order to investigate the properties of H_2 molecules. Out of the multiple transitions of this system, the Q branches ($N'' = N'$) for the first four diagonal vibrational transitions ($\nu'' = \nu' \in [0,3]$) are investigated. This data can be used in order to determine T_{gas} and the total emission of the Fulcher band ϵ_{Ful}. The evaluation of the data follows the procedure outlined in [BF20]. The emissivity $\epsilon_{\mathrm{d}\to\mathrm{a}}^{\nu',\nu'',N',N''}$ of a single transition of the Fulcher-α system is determined by [Her50]

$$\epsilon_{\mathrm{d}\to\mathrm{a}}^{\nu',\nu'',N',N''} \propto n_{\mathrm{d}}^{\nu',N'} \cdot \frac{S_{\mathrm{Q}}(N')}{2N'+1} \cdot A_{\mathrm{d}\to\mathrm{a}}^{\nu',N'}\,. \tag{2.30}$$

Here, $n_{\mathrm{d}}^{\nu',N'}$ is the density of H_2 molecules in the ro-vibronic state $\mathrm{d}^3\Pi_{\mathrm{u}}(\nu', N')$. $S_{\mathrm{Q}}(N')$ is the Hönl-London factor, which determines the relative intensities among the Q branch and $A_{\mathrm{d}\to\mathrm{a}}^{\nu',N'}$ is the vibronic transition probability which is defined in [FW06].

The $\mathrm{d}^3\Pi_{\mathrm{u}}$ state is predominantly populated via electron impact excitation from the ground state $\mathrm{X}^1\Sigma_{\mathrm{g}}^+$. This means that the rotational and vibrational population of the $\mathrm{d}^3\Pi_{\mathrm{u}}$ state (ultimately determining $n_{\mathrm{d}}^{\nu',N'}$) can be calculated from a known corresponding ground state distribution. This calculation is performed in order to determine T_{gas} and ϵ_{Ful}. In the course of this, vibrationally resolved electron excitation cross sections are used and the selection rule $\Delta N = 0$ for electron impact excitation is used. The electron temperature T_e is necessary for this as an independent input parameter. For the ground state vibrational and rotational distribution, two-temperature distributions are used respectively agreeing with experimentally observed distributions in LPLT plasmas [BF20]. They are characterized by the vibrational temperatures $T_{vib,1}$ and $T_{vib,2}$ and the rotational temperatures $T_{rot,1}$ and $T_{rot,2}$. The weighing factors β_{vib} and β_{rot} are used to adjust the share of the two distributions respectively. The two temperatures $T_{vib,1}$ and $T_{rot,1}$ arise from the plasma processes which cause the population of rotational and vibrational levels as outlined in chapter 2.2.2. $T_{vib,2}$ and $T_{rot,2}$ arise from the production of highly vibrationally and rotationally excited molecules via wall recombination of H atoms as described in [VSE04]. $T_{vib,2}$ and $T_{rot,2}$ are set to the same value and $\beta_{rot} = \beta_{vib} = \beta$ is used for the evaluation. The result of the calculated $d^3\Pi_u(\nu', N')$ populations is compared to the recorded emission following equation (2.30) and $T_{rot,1}$, $T_{rot,2} = T_{vib,2}$, $T_{vib,1}$ and β are optimized such that the calculation fits best to the measurement. The resulting value of $T_{rot,1}$ is taken as value for T_{gas}.

Knowing the vibrational and rotational population of the $d^3\Pi_u$ state, the absolute value of the entire Fulcher-α emission ϵ_{Ful} can be calculated. For this, the earlier determined rotational and vibrational population of the ground state is used in order to determine the vibrational and rotational population of the $d^3\Pi_u$ levels by balancing vibrationally resolved electron excitation and spontaneous emission. From this information, the full emission spectrum of the P, Q and R branches of the Fulcher-α transition is calculated.

2.4.2 A collisional radiative model for atomic and molecular hydrogen

The entire Fulcher-α emission in combination with the emission of the H atom Balmer lines can be used to determine the plasma parameters n_e, T_e and n_H. For this, the population of the excited H atom states as well as the H_2 $d^3\Pi_u$ state need to be modelled as a function of the mentioned plasma parameters. A Boltzmann distribution is not valid for the excitation of H atoms such that

$$n_{H,n=1} \gg \sum_{i\geq 2} n_{H,n=i}$$
$$\Rightarrow n_H = n_{H,n=1} \,.$$

This is why the *collisional radiative* (CR) models Yacora H and Yacora H_2 [WF16b, WSB+21] are used for this which solve the balance equations for the H atom states with principal quantum number $n \leq 40$ and for those molecular triplet states which dissociate into H atoms with principal quantum number $n \leq 10$. The restriction to these states has been proven to be valid by benchmarks of calculated population densities against measurements by optical emission spectroscopy. This system of differential equations is solved for its equilibrium where the time derivatives of the densities are 0. n_H, n_e, T_e, T_gas and the ion densities are input parameters for the calculations. The energy distribution functions of all particles are accordingly assumed to follow a Maxwell-Boltzmann distribution. These parameters change on a much lower time scale than the excited state densities of H and H_2 such that the input parameters are kept constant for the model calculations. The processes which are considered in the two models are depicted in table 2.4. The result of the models are the population coefficients R_{si} which link the equilibrium density n_i of the corresponding particle (H or H_2) in state i to n_e and the density n_s of particle species s. n_i is then given by

$$n_i = n_\mathrm{e} \sum_s n_s \, R_{si}(T_\mathrm{e}, n_\mathrm{e}, \ldots) \,. \tag{2.31}$$

In this way, information about the specific reaction channel which is responsible for the production of particles in state i is gained. The values of R_{si} depend on the specific input parameters which are used for the calculation. The used model of atomic hydrogen is described more thoroughly in [WF16b] whereas the molecular hydrogen model which is relevant for this work is described in [WSB+21].

In order to use the model results for diagnostic purposes, a set of population coefficients is calculated for a broad range of specific input parameters. Using equation (2.12), the absolute values of the resulting densities n_i are compared to the Balmer emissivities $\epsilon_{\alpha-\epsilon}$ and the Fulcher-α emission ϵ_Ful determined via spectroscopy. Also ratios of specific emission lines are compared to the respective calculated line ratios. The set of input parameters is then optimized such that the resulting n_i values fit best to the spectroscopic results. Simultaneously, the charged particle densities are constrained by the quasi-neutrality relation

$$n_{\mathrm{H}^-} + n_\mathrm{e} = n_{\mathrm{H}^+} + n_{\mathrm{H}_2^+} + n_{\mathrm{H}_3^+} \tag{2.32}$$

and the densities of neutral species need to fulfil the ideal gas law

Table 2.4: *Population and de-population reactions considered for the CR models Yacora H and* H_2 *[WF16b, WSB+21]. For H atoms, the principal quantum number is parametrized by* p *and* q*. For the* H_2 *molecules, the same holds for the electronic states. Vibrational and rotational excitation of* H_2 *molecules is not considered.*

Yacora H

Electron impact (de-)excitation:	$\mathrm{H}(p) + \mathrm{e}^-$	$\longrightarrow$	$\mathrm{H}(q \gtrless p) + \mathrm{e}^-$
Spontaneous emission:	$\mathrm{H}(p)$	$\longrightarrow$	$\mathrm{H}(q < p) + h\nu$
Electron impact ionization:	$\mathrm{H}(p) + \mathrm{e}^-$	$\longrightarrow$	$\mathrm{H}^+ + 2\,\mathrm{e}^-$
Three-body recombination:	$\mathrm{H}^+ + 2\,\mathrm{e}^-$	$\longrightarrow$	$\mathrm{H}(p) + \mathrm{e}^-$
Radiative recombination:	$\mathrm{H}^+ + \mathrm{e}^-$	$\longrightarrow$	$\mathrm{H}(p) + h\nu$
Dissociative excitation:	$\mathrm{H}_2 + \mathrm{e}^-$	$\longrightarrow$	$\mathrm{H}(p) + \mathrm{H}(1) + \mathrm{e}^-$
Dissociative excitation:	$\mathrm{H}_2^+ + \mathrm{e}^-$	$\longrightarrow$	$\mathrm{H}(p) + \mathrm{H}^+ + \mathrm{e}^-$
Dissociative recombination:	$\mathrm{H}_2^+ + \mathrm{e}^-$	$\longrightarrow$	$\mathrm{H}(p) + \mathrm{H}(1)$
Dissociative recombination:	$\mathrm{H}_3^+ + \mathrm{e}^-$	$\longrightarrow$	$\mathrm{H}(p) + \mathrm{H}_2$
Mutual neutralization:	$\mathrm{H}^- + \mathrm{H}^+$	$\longrightarrow$	$\mathrm{H}(p) + \mathrm{H}(1)$
Mutual neutralization:	$\mathrm{H}^- + \mathrm{H}_2^+$	$\longrightarrow$	$\mathrm{H}(p) + \mathrm{H}_2$

Yacora H_2

Electron impact (de-)excitation:	$\mathrm{H}_2(p) + \mathrm{e}^-$	$\longrightarrow$	$\mathrm{H}_2(q \gtrless p) + \mathrm{e}^-$
Electron impact ionization:	$\mathrm{H}_2(p) + \mathrm{e}^-$	$\longrightarrow$	$\mathrm{H}_2^+ + 2\,\mathrm{e}^-$
Spontaneous emission:	$\mathrm{H}_2(p)$	$\longrightarrow$	$\mathrm{H}_2(q < p) + h\nu$
Quenching:	$\mathrm{H}_2(p) + \mathrm{H}_2$	$\longrightarrow$	$\mathrm{H}_2(q < p) + \mathrm{H}_2$
Charge exchange with H^+:	$\mathrm{H}_2(p) + \mathrm{H}^+$	$\longrightarrow$	$\mathrm{H}_2^+ + \mathrm{H}$
Dissociative attachment:	$\mathrm{H}_2(p) + \mathrm{e}^-$	$\longrightarrow$	$\mathrm{H}_2^- \longrightarrow \mathrm{H} + \mathrm{H}^-$

$$\begin{aligned} p \cdot V &= \left(N_\mathrm{H} + N_{\mathrm{H}_2}\right) k_\mathrm{B} T_\mathrm{gas} \\ \Rightarrow n_\mathrm{H} + n_{\mathrm{H}_2} &= \frac{p}{k_\mathrm{B} T_\mathrm{gas}}\,, \end{aligned} \tag{2.33}$$

where V is the plasma volume while p is the total pressure in the discharge vessel. Other particle species do not contribute to the pressure due to their low density. With this procedure, global values of n_e, T_e and n_H are obtained as the optimized set of input parameters.

Concerning n_H, this evaluation is considered reliable in ionizing plasmas since the majority of excited H atoms originates from electron impact excitation of H atoms [BF18]. The emission of the Balmer lines depends thus mostly on n_e, T_e and n_H, such that the relative error bar of the resulting parameters is small for the evaluation. In a recombining plasma, this process plays only a minor role and the production of excited H atoms is dominated by recombination processes of the positive ions [BF18]. This causes on the one hand that more free parameters are relevant for the model calculations making it more difficult to find the optimal set of parameters. On the other hand, the influence of H atoms on the excited state densities is not big such that it can be varied within a larger interval without much influence on the modelling results. Both raises high error bars to the resulting n_H value in that case.

Presently, these models are only established for hydrogen and not for deuterium. Yet, they can be applied on D_2 plasmas under certain remarks. D atoms exhibit the same electronic structure compared to H atoms due to the low respective mass dependence. Thus, the rates of reactions which involve H/D atoms exclusively are directly transferable which also holds for H^+/D^+ ions. In contrast, molecular deuterium exhibits a differing rotational and vibrational structure such that also the cross sections of reactions involving D_2 molecules and molecular ions change. This leads to an isotope dependence of the reaction rates involving H_2/D_2 molecules and molecular ions. However, the corresponding cross sections are not available with the required precision such that no model for deuterium has been developed. Therefore, also here the models Yacora H and H_2 are used.

2.4.3 Re-absorption of photons

The inverse process of spontaneous emission is the absorption of photons while exciting a particle from state q into state p. In plasmas, emitted photons can be absorbed again while traversing through the plasma which acts as a further excitation mechanism for the lower state particle. This process is called *photon re-absorption* and is treated extensively in [Gri97, MO99]. In hydrogen plasmas, especially the transitions terminating on the ground state are prone to photon re-absorption which causes a significant increase in the population of excited H atoms which holds especially for the main quantum number $n = 2$ [BF00]. This is due to the high Einstein coefficient A_{pq} of the corresponding transitions and the high ground state H atom density [Beh98]. In CR models, this process needs to be accounted for in order to depict the population coefficients correctly.

A method to accomplish this is the *escape factor* method which is described in [Iro79a, Iro79b, Iro79c, Iro80] and is shortly introduced in the following. The escape factor method treats photon re-absorption effectively as a weakening of the Einstein coefficient such that equation (2.12) is rewritten to

$$\frac{\mathrm{d}n_p}{\mathrm{d}t} = -n_p\, A_{pq}\, \Theta_{\mathrm{P}}\,. \tag{2.34}$$

Θ_{P} is the *population escape factor* that corresponds to a solution of the Holstein-Biberman equation which is treating the re-absorption problem as a rate equation for the upper state [MO99]. It is calculated in [BF00] for the Lyman series in atomic hydrogen. Θ_{P} depends on the spatial distribution of the (radiating) upper state density, the ground state hydrogen density, the transition line profile and the geometry of the plasma. Those parameters need to be measured or assumed in order to perform an escape factor calculation. For the use within Yacora H, a set of population escape factors is calculated for varying n_{H} and $T_{\mathrm{H}}(= T_{\mathrm{gas}})$. The latter parameter is relevant for the transition line profile due to Doppler broadening. Concerning the terminology: if a Yacora calculation is performed without considering photon re-absorption ($\Theta_{\mathrm{P}} = 1$), it is denoted as an *optically thin* case whereas otherwise ($\Theta_{\mathrm{P}} \neq 1$) it is denoted as an *optically thick* case. Correspondingly, the effect of photon re-absorption is often denoted as *optical thickness* or *opacity* in the literature.

2.5 Negative hydrogen ion sources for NBI

The NBI for ITER requires an ion source which operates at 0.3 Pa while maintaining extracted H^- and D^- current densities of 329 $\mathrm{A/m^2}$ and 286 $\mathrm{A/m^2}$ respectively while the co-extracted electron current density is to be kept below these values [HBB+17]. In order to produce a sufficient H^- density via volume production, reaction (2.24) needs to be enhanced. For this, high pressure and high electron density are beneficial, which contradict the ITER requirements regarding the filling pressure of 0.3 Pa and the low co-extracted electron current respectively. In contrast, the H^- production based on surface conversion offers the possibility to fulfil the ITER requirements [FFK+07]. In order to maximize the share of H^- that is extracted, their trajectory length inside the plasma is to be kept small preventing H^- destruction. Thus, a negative ion source needs to be constructed in such a way that H^- generation and extraction are located very close to each other [FFF+06, FFK+07]. In order to optimize the source regarding the H^- production rate, the *tandem principle* is utilized. Here, the source is divided into two regions: a “hot” plasma region ($T_{\mathrm{e}} \approx 10\,\mathrm{eV}$) and a “cold” plasma region ($T_{\mathrm{e}} \lesssim 2\,\mathrm{eV}$). The initial

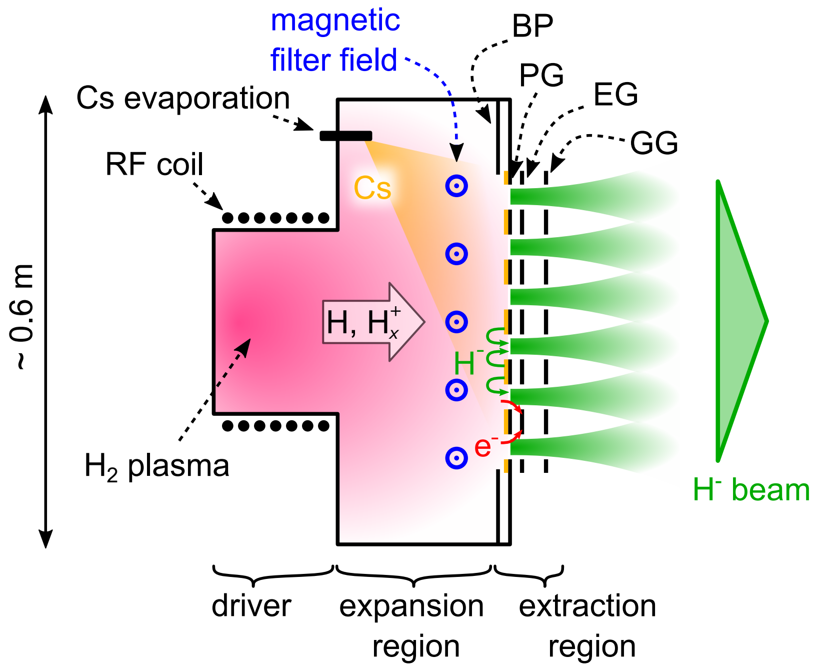

Figure 2.5: *Schematic drawing of the H^- ion source developed at IPP. BP: bias plate, PG: plasma grid, EG: extraction grid, GG: grounded grid.*

intention of this concept was to produce vibrationally excited H_2 molecules in the hot plasma region which expand into the cold plasma region in order to form H^- via the volume production process [Bac06].

The same concept was adopted by the RF driven negative ion source based on surface conversion. In that case, the hot plasma region is used for the production of H atoms as well as H_x^+ ions by electron impact which is favoured by high electron temperature. These particles expand into the cold plasma region in which they are converted into H^- at the converter surface. The low electron temperature prevents the H^- to be destroyed via electron stripping. The RF negative ion source was developed at the Max-Planck-Institut für Plasmaphysik (IPP) in Garching and it was chosen as the reference source for the ITER NBI [HDG+09]. Figure 2.5 shows the reference source in a schematic view. It consists of three parts, namely the *driver*, the *expansion region* and the *extraction region*. The driver consists of a cylindrical plasma vessel which is surrounded by a coil connected to an RF generator via an RF matching network. Here, a H_2 plasma is generated via inductive coupling resulting in electron densities of $10^{18}\,\mathrm{m}^{-3}$ and temperatures above 10 eV [FBH+21]. Capacitive coupling is prevented with the aid of a Faraday shield enclosing the driver. The high potential differences between plasma and vessel walls would cause significant damage to the driver walls due to sputtering otherwise. The hot plasma expands into the expansion region towards the plasma facing grid of the grid system (called *plasma grid*, PG). Here, H^- is produced via surface conversion of H atoms and positive ions approaching from the driver. For this, the PG needs to be covered with Cs which is evaporated by a Cs oven located above the driver. Following the evaporation of Cs into the plasma chamber, it is redistributed within the whole ion source by the plasma. A magnetic filter field (~ mT) is created in the expansion region to reduce the electron density and temperature which suppresses electron stripping of H^- and lowers the amount of co-extracted electrons. Due to their low mass and high velocity, the electrons are magnetized by the magnetic field such that their diffusion towards the PG is hindered (reducing their density) and their collisionality is increased (causing cooling of electrons) [Hol82, FSF+11]. This results in an electron density of $\sim 10^{17}\,\mathrm{m}^{-3}$ and an electron temperature of $\lesssim 2\,\mathrm{eV}$ in the vicinity of the PG [BF18, FBH+21]. The horizontally aligned magnetic filter field is created by driving a current (~ kA) vertically through the PG. Apertures are embedded in the PG for negative ion extraction. The beam is extracted through several (~ 100) apertures while a beam that is extracted through a single aperture is called *beamlet*. The apertures are enclosed by the *bias plate* (BP). Both PG and BP can be biased positively with respect to the other source walls which has a beneficial influence on the amount of co-extracted electrons [WF16a]. The H^- ions are extracted by applying a voltage of up to 10 kV between the PG and the following grid, the *extraction grid* (EG). Co-extracted electrons are deflected by permanent magnets which are embedded in the EG and hit the EG. The ions are accelerated towards their full energy between the EG and the last grid, the *grounded grid* (GG). This grid is kept at ground potential such that the ion source vessel is kept at the negative high voltage potential.

On the H atom density and VDF close to the PG

Regarding the two surface conversion reactions (2.25) and (2.26), the dominant process of the two is considered to be the conversion of H atoms. This was shown in [WSM+12], where the amount of produced negative ions by conversion of H atoms or positive ions is estimated and compared. Thus, the amount of generated H^- ions depends directly on the density n_H and the VDF of hydrogen atoms in the vicinity of the plasma grid. Hence, reliable measurements of these two parameters are desirable.

At BATMAN Upgrade, the relevant position for the determination of n_H is close to the plasma grid, as the production of negative hydrogen ions takes place there. The result of the OES investigations undertaken at BATMAN Upgrade close to the plasma grid is n_H between $6 \times 10^{18}\,\mathrm{m}^{-3}$ and $8 \times 10^{18}\,\mathrm{m}^{-3}$ at a pressure of 0.3 Pa [BF18] and values between $1 \times 10^{19}\,\mathrm{m}^{-3}$ and $2 \times 10^{19}\,\mathrm{m}^{-3}$ at 0.6 Pa [FFF+06]. When operated with deuterium, the atomic density was higher compared to hydrogen [FFF+06]. However, the plasma close to the PG is recombining such that the stated values are assigned with a high error bar. In addition, photon re-absorption can not be accounted for since the complicated geometry of the ion source makes the determination of population escape factors computationally very expensive. Therefore only optically thin Yacora calculations were considered for the determination of the stated parameters. T_H was determined by evaluating the Doppler broadening of the H_α line to be 0.8 eV [WMS+13]. That value was corrected recently by using a spectrometer with a higher resolution revealing a two temperature distribution of H atoms with a cold temperature of 2200 K and a hot temperature of 2.5 eV. The share of the two populations depends on the operation parameters [FBH+21]. As the observed radiation originates from excited H atoms, it is not yet clear if it is also present among ground state atoms.

In [Koh15], the H atom density and its energy distribution function were simulated in a DSMC (direct simulation monte carlo) code which models generation, collisions and destruction of neutral particles in a scaled version of the ion source of BATMAN Upgrade. Close to the PG, the calculation predicts a H atom density of $9 \times 10^{18}\,\mathrm{m}^{-3}$ for a pressure of 0.3 Pa at a power of 60 kW coupled to the plasma. The resulting energy distribution function is strongly peaked towards 0 eV but exhibits a prominent high energy tail which makes the distribution strongly non-Maxwellian. The tail features energies above 20 eV and is caused by the recombination of positive ions at the vessel walls with prior acceleration inside the plasma sheath.

In order to overcome the diagnostic difficulties for both parameters, it is necessary to directly access H atoms in the ground state circumventing the indirect influence of n_H and the H atom VDF on the emission spectra. TALIF offers this possibility including sufficient spectral resolution in order to determine the H atom VDF. The installation of a TALIF diagnostic at BATMAN Upgrade could therefore resolve the uncertainty of the earlier diagnostics.

3 TALIF for the H atom density and VDF determination

Laser induced fluorescence (LIF) is a widely used minimally invasive diagnostic in order to determine the density of atoms or molecules in a plasma [DMT+15, EKG20]. For this diagnostic, a laser is used in order to excite the particles of interest to an excited state. Subsequently, the excited particles emit radiation in the course of spontaneous emission which is collected with a photon detector. The detector signal is then used for the density determination [Dem07]. In addition, by varying the wavelength of the illuminating laser, the absorption line profile can be measured. That is connected to the particle velocity distribution function via the Doppler effect if the line broadening induced by this is dominant over other line broadening mechanisms.

In order to study ground state H atoms by means of single photon LIF, the wavelength of the laser needs to be smaller than or equal to 121 nm (Lyman-α transition) owing to the electronic structure of H. However, this wavelength range lies in the vacuum ultra-violet (VUV) spectral region and is thus strongly absorbed in air which raises difficulties in the realization of the experimental apparatus. In addition, the absorption of resonant photons by ground state H atoms is very strong such that these photons are absorbed within the first few mm inside the plasma [Beh98, MFB+21] which impedes LIF measurements at the plasma center. A way to circumvent these difficulties is the use of an excitation scheme based on the simultaneous absorption of two photons with double the wavelength compared to the corresponding single photon transition. The diagnostic based on such an excitation scheme is called *two-photon absorption laser induced fluorescence* (TALIF).

The process of two-photon absorption has first been described by Maria Goeppert-Mayer [GM31] and has been demonstrated for ground state hydrogen atoms by [BAFS78, ABF78, BFWS81] for various transitions. After a lot of preparatory work regarding the used two-photon transition [CMK+94a] and the calibration of a TALIF diagnostic [CMK+94b, GKD98, NSD01], TALIF is nowadays used as a diagnostic to study not only ground state H atoms but also other species such as N and O atoms [Sta20, GLA+21]. However, the two-photon absorption cross section is very small [TTSC86] such that a laser at high intensity is necessary in order to cause sufficient excitation such that the resulting fluorescence can compete against the H_α radiation of the plasma. A sufficient peak intensity can only be reached by a pulsed laser system exceeding the possible intensity of continuous wave lasers. The pulse length for TALIF systems is $\lesssim 10\,\mathrm{ns}$ with some systems operating even with fs pulses [DGdO+22, SSS+17]. While offering advantages at high discharge pressure due to quenching, such short laser pulses suffer from a very broad spectral resolution due to the Fourier limit [Rei04]. As the determination of the H atom VDF requires a narrow line width of the laser, a laser system with a pulse length of $6\,\mathrm{ns}$ is chosen for this work. For the same reason it is required that the laser wavelength needs to be tunable. These requirements can be met by a tunable dye laser system which is pumped by a frequency doubled Nd:YAG laser. Such an instrument consist of multiple optical components which are sensitive to their environment and require frequent maintenance. This is why TALIF is not a standard diagnostic despite its unique and valuable capabilities.

3.1 Two-photon absorption laser induced fluorescence

In order to excite a particle in a state 1 with the energy value E_1 into the state 2 with energy E_2 via the absorption of two photons i and k, they need to satisfy the relation

$$E_1 + h\nu_i + h\nu_k = E_2\,, \tag{3.1}$$

where $\nu_i = \frac{c}{\lambda_i}$ and $\nu_k = \frac{c}{\lambda_k}$ are the frequencies of the two photons and $\lambda_{i/k}$ the corresponding wavelengths. For TALIF as performed in this work, $\lambda_i = \lambda_k$ such that only one laser is required. In addition the two particle states need to satisfy

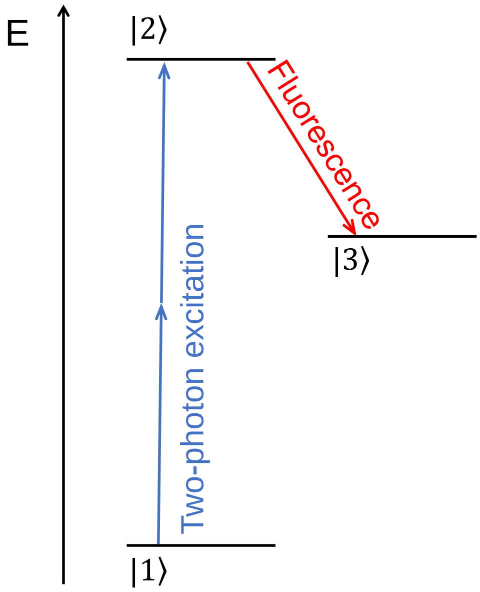

Figure 3.1: *TALIF principle.*

the selection rules for a two-photon transition [BM84]. For two linearly polarized photons of equal wavelength these are

$$\begin{aligned} &|\Delta J| \leq 2\,, \\ &\pi = \text{const}\,, \\ &J_1 + J_2 \in \mathbb{N}\,, \\ &J : 0 \leftrightarrow 1 \quad \text{forbidden}\,, \\ &\Delta M_J = 0\,, \\ \text{and if } |\Delta J| = 1,\ &M_J : 0 \rightarrow 0 \quad \text{forbidden}\,. \end{aligned} \tag{3.2}$$

Here, J_1 and J_2 denote the total angular momentum of the states 1 and 2 respectively and $\Delta J = J_2 - J_1$ is their difference. $\pi_{1/2}$ is the parity of the wave function assigned to state 1 or 2. For electronic states of the hydrogen atom with orbital angular momentum quantum number l, it is given by $\pi = (-1)^l$. $M_{J_{1/2}}$ is the magnetic quantum number of state 1 or 2, whereas ΔM_J denotes their difference.

Figure 3.1 shows the principle of TALIF for determining the density n_1 of atomic particles of species X in the ground state 1 and shall be used as a guiding example in the following. The following elaboration follows [Sta20, NSD01, vdHBM+00, CMK+94a]. When the atoms in state 1 are illuminated with a laser pulse at wavelength $\lambda = \frac{c}{\nu}$ with intensity $I(t)$, the rate at which these particles are excited to state 2 is given by

$$R_{2\mathrm{PA}}(t) = \sigma^{(2)}\, g(\lambda)\, \frac{\lambda^2}{c}\, G^{(2)} \left(\frac{\langle I(t)\rangle}{h\nu}\right)^2 . \tag{3.3}$$

Here, $\sigma^{(2)}$ denotes the two-photon absorption cross section and $g(\lambda)$ is the corresponding line profile which is normalized after $\int_{\mathrm{line}} g(\lambda)\,\mathrm{d}\lambda = 1$. $G^{(2)}$ is the photon statistical factor. It is given by the relation $\langle I(t)^2\rangle = G^{(2)} \cdot \langle I(t)\rangle^2$, where $\langle \bullet \rangle$ denotes a time average. For multi-mode lasers, $G^{(2)} = 2$ typically [CMK+94a, Lou83]. $G^{(2)}$ and the time average notation are used in equation (3.3) since the measurement of the pulsed laser intensity always happens at some finite bandwidth which is equivalent to averaging the instantaneous laser intensity over time.

Subsequent to the excitation, the X atoms in state 2 decay into state 3 spontaneously while emitting fluorescence photons. The corresponding Einstein coefficient is denoted as A_{23}. In order to connect the density n_{F} of fluorescence photons produced by one laser pulse with the density of ground state atoms n_1, the rate equation for the density n_2 of particles in state 2 is evaluated. That is

$$\frac{\mathrm{d}}{\mathrm{d}t} n_2(t) = R_{2\mathrm{PA}}(t)\, n_1(t) - A_2\, n_2(t) . \tag{3.4}$$

A_2 denotes the sum of the Einstein coefficients of all spontaneous emission transitions under which X atoms in state 2 can decay. In that equation, only the excitation of particles via two-photon absorption and spontaneous decay are considered. If further plasma or laser induced excitation and de-excitation processes need to be considered in the TALIF treatment is evaluated for each individual particle species [Sta20].

Assuming only a small influence of the laser on n_1, i. e. $n_1(t) = \text{const}$, the solution of equation (3.4) is given by

$$n_2(t) = n_1 \int_0^t R_{2\mathrm{PA}}(t')\, e^{-A_2(t-t')}\, \mathrm{d}t' . \tag{3.5}$$

From this follows that $n_2(t)$ is decaying exponentially as soon as the laser pulse has ended. The according decay constant is A_2 and the mean lifetime is $\tau = 1/A_2$. n_{F} can be calculated together with equation (3.3) via

$$\begin{aligned} n_{\mathrm{F}} &= A_{23} \int_{0}^{\infty} n_2(t)\,\mathrm{d}t \\ &= n_1\, a_{23}\, \frac{G^{(2)}\,\sigma^{(2)}}{(h\nu)^2}\, g(\lambda)\, \frac{\lambda^2}{c} \int_{0}^{\infty} \langle I(t)\rangle^2\,\mathrm{d}t\,, \end{aligned} \tag{3.6}$$

while the second step is done by performing partial integration. $a_{23} = \frac{A_{23}}{A_2}$ is the branching ratio of the observed fluorescence transition. It denotes the fraction of all excited X atoms which decay within the observed spontaneous emission channel $2 \to 3$.

In order to determine n_1, the fluorescence is detected with a photon detector which gives a signal that is proportional to the photon flux hitting its sensor area. In addition to the fluorescence in course of the TALIF diagnostic, the plasma usually emits radiation at the same wavelength since particles in the state 2 are also produced via plasma processes. This radiation is inevitably collected by the photon detector and is visible as an offset in the detector signal. Accordingly, it has to be subtracted for the evaluation. The proportionality constant between radiation and detector signal, the detector sensitivity, is denoted as ξ. The total detector signal $S_{\mathrm{Detector}}(\nu)$ per laser pulse is then given by

$$S_{\mathrm{detector}}(\lambda) = T\,\xi\,\frac{\Omega}{4\pi}\int_{V} n_{\mathrm{F}}(\vec{r})\mathrm{d}V \propto n_1 \cdot \int_{0}^{\infty} \langle I(t)\rangle^2\,\mathrm{d}t\,. \tag{3.7}$$

Here, T is the transmission of the detection optics at the wavelength of the fluorescence radiation, Ω is the acceptance solid angle of the detection system and the integral of n_{F} is performed over the whole volume observed by the photon detector. It is assumed that the emission of fluorescence is isotropic which is justified as the orientation of atoms within a plasma is generally arbitrary. This assumption is represented by the division of 4π. Moreover, Ω is assumed to be constant for fluorescence from all locations within V which is true if the distance between the photon detector and V is large compared the the dimensions of V. Lastly, n_1 is assumed to be constant within the detection volume such that the result of equation (3.7) represents an average of n_1 over V and the dimensions of V give the *resolution* of the TALIF system.

3.2 Calibration of the TALIF system

The measured $S_{\mathrm{detector}}(\lambda)$ from equation (3.7) depends on the temporal and spatial profile of the laser beam intensity, the detection optics, the photon detector itself and the line profile of the two-photon absorption transition. Deducing n_1 from $S_{\mathrm{detector}}(\lambda)$ would therefore require knowledge of all these parameters which is barely possible with the required precision. That is why a calibration of the used TALIF system is necessary. This is done as conducted in [NSD01] by using a noble gas R at known density n_R as reference. For this it is necessary that R has a two-photon transition spectrally close to the one which is used for probing the atomic species X. Probing that reference gas with the same laser system as used for X, observing the produced fluorescence and comparing the signals obtained for R and X gives then the calibration of the TALIF system. With this, however, it is assumed that the spatial intensity profile of the used laser does not change when changing its wavelength. That is reasonable if the wavelength change between the two transitions is small.

For this procedure, the normalized detector signal

$$S^X_{\mathrm{TALIF}}(\lambda) = \frac{S_{\mathrm{detector}}(\lambda)}{\int\limits_0^{\infty} \langle I(t)\rangle^2 \,\mathrm{d}t} \tag{3.8}$$

for TALIF performed on species X (and correspondingly $S^R_{\mathrm{TALIF}}(\lambda)$ for species R) is defined. With this, the ground state density of species X can be determined via [NSD01]

$$n_1 = n_R \,\frac{\xi_R\, T_R}{\xi_X\, T_X}\,\frac{a_R}{a_{23}}\,\frac{\int S^X_{\mathrm{TALIF}}(\lambda)\,\mathrm{d}\lambda}{\int S^R_{\mathrm{TALIF}}(\lambda)\,\mathrm{d}\lambda}\left(\frac{\lambda^{(2)}_{R,0}}{\lambda^{(2)}_{X,0}}\right)^4 \frac{\sigma^{(2)}_R}{\sigma^{(2)}_X}\,. \tag{3.9}$$

Here, ξ_R, T_R and ξ_X, T_X denote the detector sensitivities and detection system transmissions evaluated at the wavelengths of the fluorescence radiation of the species R and X correspondingly. a_R is the branching ratio of the observed fluorescence of species R. $\lambda^{(2)}_{R,0}$ and $\lambda^{(2)}_{X,0}$ are the central wavelengths of the two-photon transitions of the two species. $\sigma^{(2)}_R$ and $\sigma^{(2)}_X$ are the corresponding two-photon absorption cross sections. The TALIF signals are denoted as wavelength integrals over the whole transition. This is done in order to omit the line profile dependence of the TALIF signal, since $\int g(\lambda)\,\mathrm{d}\lambda = 1$. For this, $S^X_{\mathrm{TALIF}}(\lambda)$ and $S^R_{\mathrm{TALIF}}(\lambda)$ have to be measured across the whole spectral line.

With this calibration method, the only system parameters that need to be known are the ξ and T ratios at the two fluorescence wavelengths. The other constants depend on the species X and R and need to be evaluated individually. This dependence is shifted to the requirement of a precise knowledge of $\sigma_R^{(2)}$ and n_R. For the latter parameter it is therefore advantageous to use a noble gas such that the calibration can be performed without operating a plasma also omitting additional light from the plasma hitting the detector.

3.3 TALIF line profiles

The line profile $g(\lambda)$ of the two-photon absorption transition is determined by measuring $S_{\mathrm{TALIF}}^{X}(\lambda)$ while varying the wavelength of the exciting laser. The measured profile is the result of the double convolution of the actual line profile $g_{\mathrm{2PA}}(\lambda)$ with the spectral profile of the laser $g_{\mathrm{Laser}}(\lambda)$ [NSD01, Sta20]

$$g(\lambda) = g_{\mathrm{2PA}}(\lambda) \otimes g_{\mathrm{Laser}}(\lambda) \otimes g_{\mathrm{Laser}}(\lambda)\,. \tag{3.10}$$

If both $g_{\mathrm{2PA}}(\lambda)$ and $g_{\mathrm{Laser}}(\lambda)$ have the shape of a Gaussian, the resulting FWHM $\Delta\lambda$ is given by

$$\Delta\lambda = \sqrt{(\Delta\lambda_{\mathrm{2PA}})^2 + 2(\Delta\lambda_{\mathrm{Laser}})^2}\,, \tag{3.11}$$

where $\Delta\lambda_{\mathrm{2PA}}$ and $\Delta\lambda_{\mathrm{Laser}}$ are the FWHM's of the two-photon absorption and the laser line profiles respectively. From this follows the relation

$$\begin{aligned} &\Delta\lambda_{\mathrm{Laser}} \ll \Delta\lambda_{\mathrm{2PA}} \\ \Rightarrow &\Delta\lambda = \Delta\lambda_{\mathrm{2PA}}\,. \end{aligned}$$

This is why it is preferred to use a laser with a low λ_{Laser} value if $g(\lambda)$ is a parameter of interest.

The shape and FWHM of $g_{\mathrm{2PA}}(\lambda)$ depends on the line broadening mechanisms that are relevant for the transition. As was elaborated in chapter 2.1.2, these are *natural broadening* and *Doppler broadening*. Concerning natural broadening, the resulting FWHM $\Delta\lambda_{\mathrm{2PA,nat}}$ is given by [Bir19]

$$\Delta\lambda_{\mathrm{2PA,nat}} = \frac{\left(\lambda_0^{(2)}\right)^2}{c}\left(\frac{1}{4\pi\tau_1} + \frac{1}{4\pi\tau_2}\right)\,. \tag{3.12}$$

$\lambda_0^{(2)}$ is the central wavelength of the two-photon transition. $\tau_{1/2}$ are the average lifetimes of the X atom states 1 and 2 involved in the two-photon absorption.

If the X atoms have a Maxwell-Boltzmann velocity distribution function with temperature T_X, the FWHM $\Delta\lambda_{\mathrm{2PA,Dop}}$ arising from Doppler broadening is given by [CCL⁺99]

$$\Delta\lambda_{\mathrm{2PA,Dop}} = \frac{\lambda_0^{(2)}}{c}\sqrt{\frac{8\,\ln(2)\,k_{\mathrm{B}}\,T_X}{m_X}}\,. \tag{3.13}$$

Here, m_X is the X atom mass. If the atomic VDF is not given by a Maxwell distribution, $g_{\mathrm{2PA}}(\lambda)$ is given by the projection of the full VDF onto the axis parallel to the laser beam $f_{v_\parallel,X}(v_\parallel)$ [MVES01]. The velocity is converted into a wavelength by using the Doppler relation

$$\lambda' = \lambda\cdot\left(1 \pm \frac{v_\parallel}{c}\right)\,, \tag{3.14}$$

where λ' denotes the wavelength in the rest frame whereas λ is the wavelength in the moving frame of the atom (i. e. $\lambda_0^{(2)}$).

3.4 Application to hydrogen

The TALIF scheme that is used for the investigation of atomic hydrogen in this work is shown in the energy diagram in figure 3.2 (a), where the energy axis is shifted in such a way that the value 0 corresponds to the H atom ground state. The corresponding two-photon absorption wavelength and cross section data is shown in table 3.1 as well as the fluorescence transitions together with their wavelength and Einstein coefficients. Here, ground state H atoms are excited into the states $3^2D_{3/2}$, $3^2D_{5/2}$ and $3^2S_{1/2}$ via the absorption of two 205.08 nm photons according to the selection rules (3.2) for two-photon absorption. Transitions into the states $3^2P_{3/2}$ and $3^2P_{1/2}$ are omitted by the selection rules. The subsequent fluorescence decay happens in the course of the H_α transition at 656.3 nm. The two-photon absorption cross sections shown in table 3.1 were calculated in [TTSC86] not for the fully resolved fine structure states but for groups of levels with $n = 3$ according to their value of l. That is why those groups are shown in figure 3.2 (a). The two-photon absorption cross section for the $3d$ states is bigger by a factor of 7.56 compared to the $3s$ cross section. Because of this and due to the significantly lower fluorescence Einstein coefficient of the latter state, the two-photon absorption transition into the $3s$ state is commonly disregarded [Sta20].

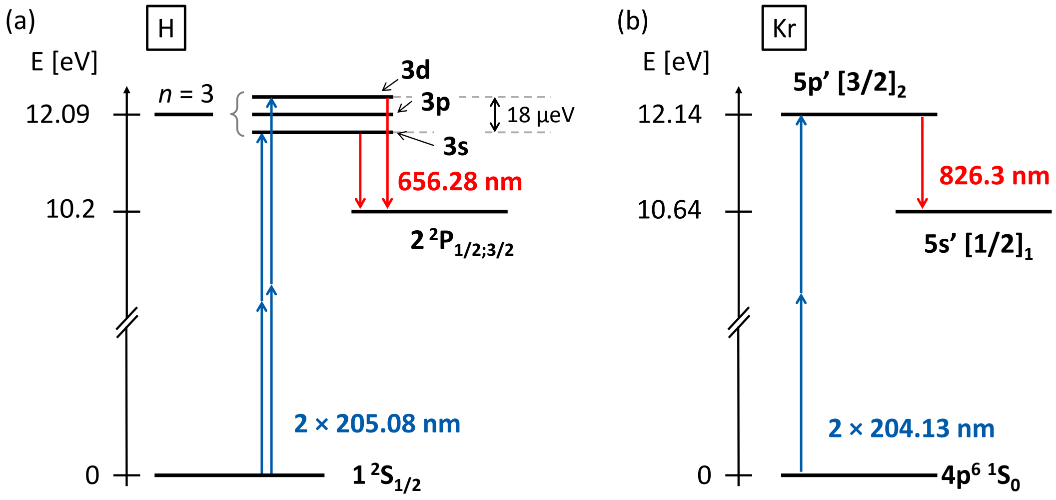

Figure 3.2: *Applied TALIF schemes for ground state (a) hydrogen and (b) krypton atoms.*

Table 3.1: *Upper states of the two-photon absorption transitions for H atoms used for TALIF with the corresponding two-photon absorption wavelength and cross section [TTSC86], fluorescence transitions with the corresponding wavelengths and Einstein coefficients [NIST].*

State	$\lambda_0^{(2)}$ [nm]	$\sigma^{(2)}$ [cm^{-4}]	Fluorescence transition	λ [nm]	Einstein coefficient [s^{-1}]
$3^2D_{5/2}$	205.08437		$\longrightarrow 2^2P_{3/2}$	656.285	6.47×10^7
$3^2D_{3/2}$	205.08444		$\longrightarrow 2^2P_{1/2}$	656.271	5.39×10^7
			$\longrightarrow 2^2P_{3/2}$	656.287	1.08×10^7
$3^2S_{1/2}$	205.08465		$\longrightarrow 2^2P_{1/2}$	656.275	0.21×10^7
			$\longrightarrow 2^2P_{3/2}$	656.291	0.42×10^7
$3d$	205.0844	1.77×10^{-35}	$\longrightarrow 2p$	656.3	6.47×10^7
$3s$	205.0847	0.23×10^{-35}	$\longrightarrow 2p$	656.3	0.63×10^7

Krypton is used for the calibration of the hydrogen TALIF system as proposed in [NSD01]. The corresponding TALIF scheme is shown in figure 3.2 (b). Ground state ($4p^6\,{}^1S_0$) krypton is excited to the state $5p'\,[3/2]_2$ by absorbing two photons at 204.13 nm. Subsequently, the excited atoms decay into the state $5s'\,[1/2]_1$ while emitting radiation at 826.3 nm. The ratio of the two-photon absorption cross sections $\sigma^{(2)}_{\mathrm{Kr}}/\sigma^{(2)}_{\mathrm{H}}$ was determined in [NSD01] to be 0.62 assigned with an uncertainty of ±50 %. The Einstein coefficient of the fluorescence transition is $3.42 \times 10^7\,\mathrm{s}^{-1}$.

The other species dependent parameter in equation (3.9) that needs to be evaluated for H and Kr atoms is the corresponding branching ratio. This parameter needs a more thorough treatment. To further determine, if equation (3.4) describes the processes happening during and after the laser pulse in the plasma to a satisfying degree, further laser and plasma induced processes need to be evaluated for H and Kr according to [Sta20], which will be done in the following sub-chapters.

3.4.1 Branching ratios and fluorescence decay times

The $n = 3$ H atom states excited by two-photon absorption do not have any further spontaneous emission transitions than the ones shown in table 3.1, such that the branching ratio a^{H}_{23} of the fluorescence is 1 and the lifetime of the excited states is 15.4 ns (when disregarding the $3s$ excitation). The krypton state $5p'\,[3/2]_2$ has two further spontaneous emission transitions, such that $a^{\mathrm{Kr}}_{23} = 0.977$ and its lifetime is 28.5 ns [NIST].

In addition to radiation losses, de-excitation of excited particles via the collision with other heavy particles or electrons (so called *quenching*) can build a significant loss channel of excited atoms. In this case the branching ratio needs to be corrected via [Sta20]

$$a_{23} = \frac{A_{23}}{A_2 + Q}\,, \tag{3.15}$$

where Q is the quenching rate of the excited particles. It is given by

$$Q = \sum_q k^X_q n_q\,. \tag{3.16}$$

k^X_q is the corresponding quenching coefficient of the excited atom X for the quenching partner q and n_q the q density. The sum in this equation is performed for all potential quenching partners q of the excited atom. The lifetime τ_X of excited atoms is then reduced according to

$$\tau_X = (A_2 + Q)^{-1} . \tag{3.17}$$

Quenching coefficients of the excited H and Kr states have been measured in [NSD01] for various quenching partners. The hydrogen plasmas that are investigated in this work, are fed either only with H_2 gas or a H_2/He mixture. The quenching coefficients of the excited H atoms for H_2 and He are

$$k_{\mathrm{H_2}}^{\mathrm{H}} = 20.4 \times 10^{-16}\,\mathrm{m^3\,s^{-1}} \quad \text{and} \quad k_{\mathrm{He}}^{\mathrm{H}} = 0.18 \times 10^{-16}\,\mathrm{m^3\,s^{-1}} .$$

In this work, the highest investigated pressure is 10 Pa and the according gas temperature was determined to be 650 K in that case (see chapter 5 for further details). Here, Q has the value $2.3 \times 10^6\,\mathrm{s^{-1}}$. This is roughly 3 % of the $3d$ Einstein coefficient such that quenching is negligible for pressures ≤ 10 Pa.. Since the quenching coefficient for helium is two orders of magnitude lower than the H_2 quenching coefficient and the partial helium pressure is below 5 Pa in the investigated plasmas, helium quenching of excited H atoms can be ignored. Quenching by electrons was investigated in [vdHBM+00] where quenching by electrons was only present at electron densities well above $10^{18}\,\mathrm{m^{-3}}$. This is one magnitude higher than any electron density observed in the plasmas of this work.

For the calibration with Kr, pure Kr gas is filled into the vacuum vessel meaning that the gas is at room temperature. The quenching coefficient of the $5p'\,[3/2]_2$ state by Kr atoms (self-quenching) was determined to be [NSD01]

$$k_{\mathrm{Kr}}^{\mathrm{Kr}} = 1.46 \times 10^{-16}\,\mathrm{m^3\,s^{-1}} .$$

At room temperature and at a pressure of 10 Pa, this leads to a quenching rate of $Q = 3.6 \times 10^5\,\mathrm{s^{-1}}$, which is two orders of magnitude lower than the fluorescence Einstein coefficient of the observed transition. At low pressure below 10 Pa, quenching can thus be ignored for the Kr TALIF.

A further process that can alter the branching ratio of the observed hydrogen transition is the population of the $3p$ states by redistribution of the two-photon absorption excited $3d$ and $3s$ states. This process is called l state mixing and

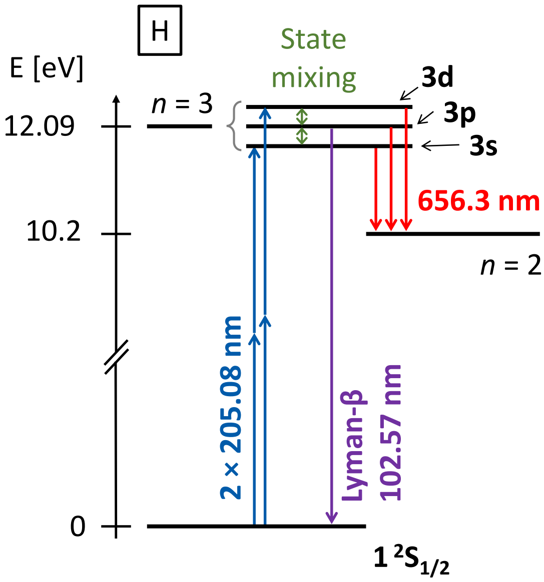

Figure 3.3: *Hydrogen atom TALIF scheme complemented with the population of the 3d states via l state mixing.*

was observed in [PPT+95] and [vdHBM+00]. Figure 3.3 shows the H atom TALIF scheme from figure 3.2 (a) complemented with l state mixing. With the additionally populated levels, the Lyman-β transition at 102.6 nm serves as an additional decay channel for the excited H atoms and has to be considered in the branching ratio calculation. Assuming population among the $n = 3$ fine structure states according to their respective statistical weights (i. e. *perfect state mixing*) results in a branching ratio of 0.441 and a lifetime of the excited states of 10 ns [vdHBM+00].

In [PPT+95], l state mixing is attributed to heavy particle collisions of the excited H atoms and mixing coefficients equivalent to the quenching coefficients in equation (3.16) are derived from the experimental data. On the other hand, [vdHBM+00] attributes the l state mixing to electric fields within the Debye sphere or the laser beam electric field. In general, the presence of l state mixing can be evaluated by measuring the fluorescence decay time τ_{H} from the time resolved photon detector signal. The branching ratio is in turn determined based on these measurements.

For the measurement of τ_{H}, the temporal pulse shape of the laser is not important as the decay of excited H atoms follows exponential decay as soon as the laser intensity drops to 0. However, the pulse length of the laser needs to be shorter than the fluorescence decay time in order to differentiate between the temporal laser intensity profile and the fluorescence decay. This is demonstrated in [SSS+17] where a highly quenched O atom TALIF signal reaches decay times clearly below 1 ns. Only TALIF systems operating with laser pulses at a length on the ps or fs scale are capable of making such timescales accessible. In this work, the shortest expected decay time is 10 ns, such that the pulse length of 6 ns mentioned earlier is sufficient for the determination of τ_{H}.

3.4.2 TALIF saturation

From equation (3.6) it is apparent that the produced fluorescence photons density depends quadratically on the intensity of the exciting laser. If a TALIF signal is saturated, this dependency is of lower order and the shown calibration procedure is not valid. Saturation of TALIF signals can occur owing to three processes, namely the ionisation of the two-photon absorption excited atoms absorbing a third photon (*three-photon ionisation*), the depletion of the ground state and stimulated two-photon emission.

- For the H atom TALIF scheme used in this work, three-photon ionisation is possible, since the ionization threshold energy for photoionisation of $n = 3$ atoms (1.51 eV) is smaller than the photon energy of the used laser (6.05 eV). The ionisation rate $\Gamma(t)$ of $n = 3$ H atoms when illuminated with laser intensity $I(t)$ is given by [LH95]

  $$\Gamma(t) = \sigma(\lambda_{\mathrm{Laser}}) \cdot \frac{\lambda_{\mathrm{Laser}}\, I(t)}{h\, c}\,, \tag{3.18}$$

  where $\sigma(\lambda_{\mathrm{Laser}})$ is the photoionisation cross section. For H atom states with main quantum number n, it is given by

  $$\sigma(\lambda_{\mathrm{Laser}}) = 2.815 \times 10^{29}\,\mathrm{cm}^2\,\mathrm{s}^{-3} \cdot \frac{\lambda^3_{\mathrm{Laser}}}{c^3\, n^5}\,. \tag{3.19}$$

  This effect needs to be considered for Kr as well, but in this case no such data is available to the authors knowledge.

- The depletion of the ground state happens if for the solution of equation (3.4), $n_1(t) = \mathrm{const}$ can not be assumed since the two-photon excitation causes a significant decrease of the ground state density.

- Stimulated emission of two photons happens if the illumination of the investigated atoms with light at the two-photon absorption wavelength triggers the emission of additional photons via a two-photons transition. The stimulated emission rate is given by

  $$R_{\mathrm{SE}} = \frac{g_1}{g_2} R_{\mathrm{2PA}} \,, \tag{3.20}$$

  where g_1 is the statistical weight of the lower state and g_2 is the statistical weight of the upper state.

According to [Sta20], three-photon ionisation, ground state depletion and stimulated two-photon emission can be neglected and the shown approach is valid if

$$\begin{aligned} &\tau_{\mathrm{Laser}} \cdot R_{\mathrm{2PA}} \ll 1 \\ \text{and} \quad &R_{\mathrm{SE}} + \Gamma \ll A_2 + Q \,. \end{aligned} \tag{3.21}$$

τ_{Laser} is the pulse length of the used laser. However, the evaluation of the involved rates requires knowledge of the spatial and temporal intensity profile of the used laser system as well as the two-photon excitation and the photoionisation cross sections for both H and Kr atoms.

Alternatively, the validity of the quadratic dependence can be shown experimentally. To illustrate this, the TALIF photon fraction, i. e. the number of fluorescence photons created per H atom and laser pulse, is calculated for a laser beam at given intensity and pulse length. This is done equivalently as in [vdHBM⁺00] by solving the differential equations

$$\begin{aligned} \frac{\mathrm{d}}{\mathrm{d}t} n_{\mathrm{H},n=1}(t) &= -R_{\mathrm{2PA}}(t)\, n_{\mathrm{H},n=1}(t) + A_{\mathrm{Ly}-\alpha}\, n_{\mathrm{H},n=2}(t) + R_{\mathrm{SE}}(t))\, n_{\mathrm{H},n=3}(t) \\ \frac{\mathrm{d}}{\mathrm{d}t} n_{\mathrm{H},n=2}(t) &= -A_{\mathrm{Ly}-\alpha}\, n_{\mathrm{H},n=2}(t) + A_{\mathrm{Bal}-\alpha}\, n_{\mathrm{H},n=3}(t) \quad \text{and} \\ \frac{\mathrm{d}}{\mathrm{d}t} n_{\mathrm{H},n=3}(t) &= R_{\mathrm{2PA}}(t)\, n_{\mathrm{H},n=1}(t) - \left[A_{\mathrm{Bal}-\alpha} - \Gamma(t) - R_{\mathrm{SE}}(t)\right] n_{\mathrm{H},n=3}(t) \end{aligned}$$

for the time traces of $n_{\mathrm{H},n=1}$, $n_{\mathrm{H},n=2}$ and $n_{\mathrm{H},n=3}$. $A_{\mathrm{Ly}-\alpha}$ and $A_{\mathrm{Bal}-\alpha}$ are the Einstein coefficients for the Lyman-α ($n = 2 \longrightarrow n = 1$) and Balmer-$\alpha$ ($n = 3 \longrightarrow n = 2$) transitions respectively. For two-photon absorption, only the excitation into the

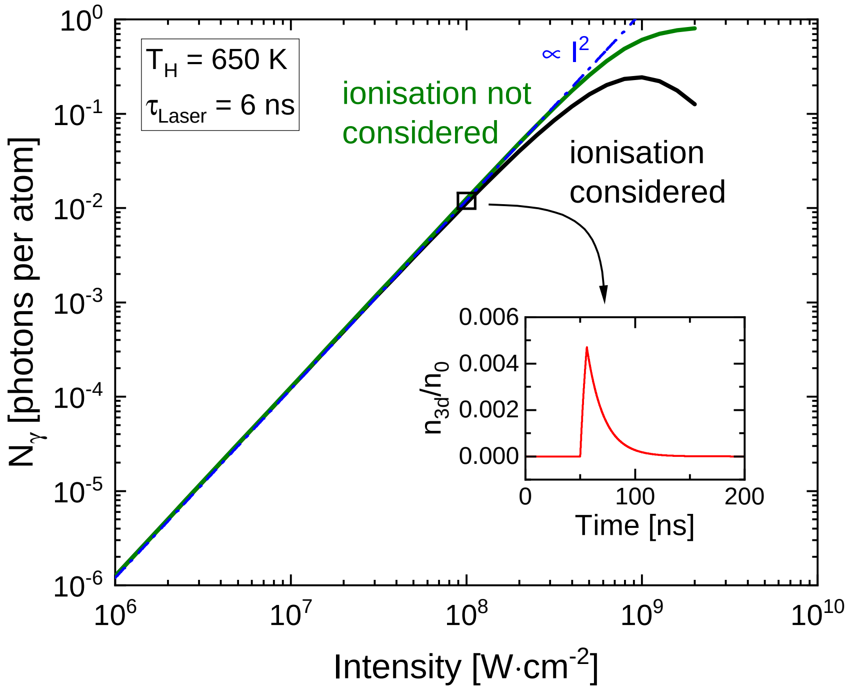

Figure 3.4: *Simulation of the emitted photon fraction as a function of laser intensity for fixed H atom temperature and laser pulse width.*

$3d$ states is considered, which decay into the $2p$ states. Thus $A_{\text{Bal-}\alpha} = 6.47 \times 10^7\,\text{s}^{-1}$ and $A_{\text{Ly-}\alpha} = 6.26 \times 10^7\,\text{s}^{-1}$ for the decay of $2p$ atoms [NIST]. The temporal laser profile is assumed to be rectangular with a pulse width of 6 ns. The laser is spectrally located at the absorption line center and its line profile is assumed to be Gaussian with a FWHM of 0.6 pm which is the value which is given by the manufacturer of the laser used in this work. For the calculation of the two-photon absorption line profile, it is assumed that the H atom temperature is 650 K whereas natural line broadening is neglected. The photon fraction N_γ is then calculated via

$$N_\gamma = A_{\text{Bal-}\alpha} \cdot \int_0^\infty \frac{n_{\text{H},n=3}(t)}{n_{\text{H},n=1}(0)}\,\text{d}t\,. \tag{3.22}$$

The differential equations are numerically solved by using the classic Runge-Kutta method under the starting conditions $n_{\text{H},n=1}(0) = 1$ and $n_{\text{H},n=2}(0) = n_{\text{H},n=3}(0) = 0$ in arbitrary units. Figure 3.4 shows calculated values of N_γ as a function of the used laser intensity. Here, two calculations are shown whereas three-photon ionisation is either included or not included in the differential equations. In the bottom right corner, $n_{\text{H},n=3}(t)$ relative to $n_{\text{H},n=1}(0)$ is shown as an example. For low laser intensity, N_γ is proportional to I^2 and $n_{\mathrm{H},n=3}(t)$ follows equation (3.5). The I region at which this holds is called the *quadratic regime*. For increasing I, N_γ reaches a plateau and drops for $I \geq 10^9\,\mathrm{W\,cm^{-2}}$. The high intensity behaviour of N_γ is predominantly caused by three-photon ionisation which is apparent from the difference between the two performed calculations. At even higher laser intensity, also the ground state depletion causes a deviation of N_γ from the quadratic behaviour. Consequently, the quadratic regime of the TALIF signal needs to be verified in the experiment. This can be done by plotting TALIF signals as a function of the laser energy per pulse.

3.4.3 Laser induced H atom production

Another possible perturbation of the TALIF signal by the laser beam itself is the additional production of H atoms via the photodissociation of other plasma species. This process corrupts the TALIF signal by increasing the photon fraction artificially. In this way, an overestimation of the TALIF signal by an order of magnitude is possible [Sta20].

The energy of 205 nm photons is 6.05 eV which is in principle higher than the binding energy of H_2 molecules of 4.5 eV. However, according to chapter 2.2.2, purely rotational or vibrational excitation of H_2 molecules is not possible such that ground state molecules can't be excited into the vibrational. This means that photodissociation could only happen via the excitation of ground state molecules into the anti-bonding $\mathrm{b}^3\Sigma_\mathrm{u}^+$ state. Consulting figure 2.2, a photon energy exceeding 10 eV would be necessary for this following the *Franck-Condon principle* which assumes no change of the internuclear distance during an electronic transition. Therefore, excitation into the anti-bonding $\mathrm{b}^3\Sigma_\mathrm{u}^+$ state is also omitted. Experimentally, photodissociation of H_2 was observed neither in neutral gas nor in plasmas [BMB+02]. Other plasma species which might cause laser induced enhancement of the H atom density are H_2^+ [Arg74], H_3^+ [UDM+19] and H^- [BHB+79]. However, in LPLT plasmas, the corresponding ion density is commonly much lower than n_H such that the distortion of the TALIF signal originating from these species can be ignored even for complete dissociation or photodetachment.

4 Towards the installation of TALIF at BATMAN Upgrade

4.1 Challenges for the installation

In order to install a TALIF system at the BATMAN Upgrade teststand, several considerations have to be made as both the teststand and the diagnostic itself are sophisticated and delicate devices. In addition, the teststand offers only limited access close to the PG where a measurement of n_{H} and the H atom VDF is desired. Out of simplicity, it would be therefore beneficial to install the laser close to the ion source in order to minimize the effort of guiding the laser beam into the teststand. However, there are mainly three considerations which speak against this:

1. The space close to the teststand is very limited such that an optical table which is necessary for the laser system does not fit into the area around the teststand. This area is enclosed due to high voltage safety.

2. During beam operation, the ion source of the teststand is kept at negative high voltage ($-45\,\mathrm{kV}$). Either, the whole laser system needs to be kept on the high voltage potential as well or the safety distance between the ion source and the laser needs to be kept while care has to be taken on the grounding of the laser components. Both options have the risk of arcs between parts on differing potential. Firstly, these include a high current which causes the heating of the involved components. Thermal stability of the laser medium is a key parameter of the stability of both energy per laser pulse and laser wavelength such that this should be avoided. Local heating of these components could also lead to thermal stress in optic holders which might damage the corresponding optic. Secondly, the laser dye is solved in ethanol which raises the risk of fire if arcs occur close to the ethanol tanks.

3. The ion source is operated with high RF power (up to 90 kW). The RF current in the antenna could cause RF radiation around the ion source which might disturb the data transfer between the laser system an the PC which is used for remote handling and the internal control of the laser. In the worst case, both could lead to damages of the laser system.

Because of these reasons and the general complexity of the diagnostic itself, TALIF was not yet installed at a H^- ion source despite its valuable diagnostic capabilities. In order to overcome this, it was decided to install the laser system further away from the teststand in a distance of 12 m on a different level of the building. This, however, raises the challenge of the laser beam transfer between the laser system and the ion source. At such a distance, even a change of the beam angle of only 0.1 ° would lead to a displacement of 2 cm which is enough to travel out of the sight cone of the fluorescence photon detector. Therefore, the use of optical fibre which guides the laser beam to BATMAN Upgrade would be the preferred solution. However, it was found that the focussed laser beam damages the fibre end, which limits the coupling of the laser into the fibre to below 1 %. In addition, quartz fibre attenuates light at 205 nm such that roughly 95 % of the light would be absorbed over the course of the 12 m distance even for perfect coupling into the fibre. Therefore, a laser beamline needs to be constructed which uses guiding mirrors.

Another point of the considerations is the first setup and construction of the complex diagnostic from scratch. For this, the installation at a continuously operating plasma source and direct access to all components is beneficial in order to optimize each single component for signal quality. With this, changes in the setup result in direct feedback which is necessary for optimization. The teststand exhibits several considerations omitting such a procedure. Firstly, BATMAN Upgrade is operated in pulsed mode with breaks on the order of several minutes between the plasma pulses. Secondly, the optimization is time consuming since TALIF measurements at BATMAN Upgrade require a dedicated experimental campaign. On the other hand, the experimental time at BATMAN Upgrade is limited due to the tight experimental schedule. Lastly, the access to the experiment during operation is restricted due to safety measures such that the optics close to the experiment can not be optimized during plasma operation. Therefore, a simple plasma experiment is built with the aim of gaining experience with the diagnostic in a controlled environment. In a second step, the experience is utilised in order to install the TALIF system at BATMAN Upgrade such that the optics

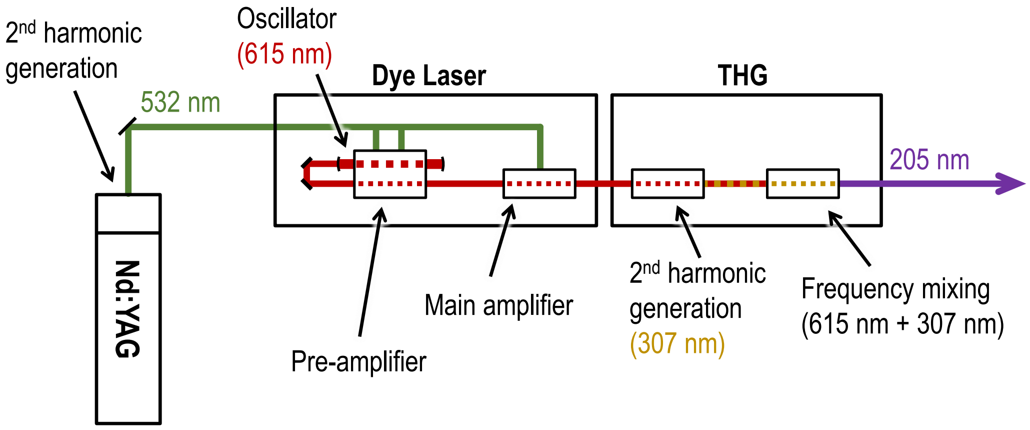

Figure 4.1: *Laser system used for the generation of the 205 nm photons. THG: third harmonic generation. Figure after [Sir19].*

can be adjusted for sufficient signal quality even without access during plasma operation.

4.2 The optical system

The laser system

The core of the TALIF system is the pulsed UV laser system which is used for the two-photon excitation. It is depicted in figure 4.1 and consists of three stages, which are the pump source, a dye laser and a third harmonic generation unit (THG). The operation principle of the laser system is shortly introduced. For a more general treatment of lasers and non-linear optics, refer to [Dem07, Rei04]

The pump source is a Q-switched diode-laser pumped Nd:YAG laser (*Innolas:* SpitLight Compact DPSS 100) which produces laser pulses at 1064 nm. Its pulse length is 6 ns with a repetition rate of 100 Hz and the total energy per pulse is specified at 110 mJ [Inn17]. The laser itself consists of two end mirrors forming the oscillator, a Nd:YAG[1] crystal as laser medium and a Pockels cell in combination with a polarizer which act as Q-switch. The latter components are all located between the two mirrors. In *shut mode* of the Q-switch, the birefringence of the Pockels cell causes a change of the polarization angle of passing light such that the combination of Pockels cell and polarizer cause significant round trip losses in the oscillator which greatly reduces the quality factor (*Q-factor*) of the resonator.

---

[1] neodymium-doped yttrium aluminium garnet, Nd:$Y_3Al_5O_{12}$

In this way, lasing is prevented even if a population inversion is present in the Nd:YAG crystal. The lasing is enabled by applying a voltage to the Pockels cell which changes its birefringence in such a way that the combination of Pockels cell and polarizer cause no losses any more restoring the Q-factor to its high value [Rei04]. With this mechanism, the emission of laser light can be timed with very high precision and the power of the laser during the pulse is large. The population inversion is generated with pulsed laser diodes which are attached to the Nd:YAG crystal.

A LBO[2] crystal is attached to the Nd:YAG laser output in order to perform second harmonic generation or *frequency doubling* of the 1064 nm light. In this process, the susceptibility of the crystal which depends non-linearly on the electric field of the laser beam causes the generation of photons at half the fundamental wavelength [Rei04]. The used system is able to deliver up to 70 mJ per laser pulse at 532 nm with a beam diameter between 3 mm and 4 mm which was coarsely measured with burn paper. The 1064 nm beam is dumped such that only light at 532 nm leaves the laser head. This beam is widened by using two lenses acting as a telescope and fed into the dye laser in order to act as its pump source. The Nd:YAG laser head is actively water cooled with a chiller that is integrated in the laser power supply.

The tunable dye laser (*Sirah Lasertechnik:* Cobra Stretch) consists of three stages, the *oscillator*, the *pre-amplifier* and the *main amplifier*. The central parts of these stages are two rectangular dye cells which contain a solution of the laser dye DCM[3] in ethanol. For the oscillator and the pre-amplifier, a concentration of 0.3 g/l is used whereas the main amplifier cell is operated with 0.1 g/l. These solutions are circulated through the dye cells continuously and actively cooled with cooling water. The pump beam is guided and focussed onto narrow regions of the dye cells by using an arrangement of mirrors, beam splitters and cylindrical lenses. In these regions, a local population inversion is caused in the dye solution by the absorption of the pump laser by the dye molecules. The oscillator dye cell is illuminated at two positions serving both as laser medium and pre-amplification stage. The laser oscillator is built around the oscillator dye cell and consists of two end mirrors and a grating (2400 grooves/mm) between the mirrors, whereas the grating is used as a wavelength selective element. Tilting of the grating can be used in order to change the selected wavelength as the deflection angle of

---

[2] Lithium triborate, LiB_3O_5

[3] For details, refer to [Exc22]

the grating is strongly wavelength dependent. In this way, a laser beam with a wavelength between 606 nm and 627 nm[4] with a spectral bandwidth of 1.8 pm is generated. The beam is reflected back onto the first dye cell at the pre-amplifier position which causes amplification of the laser beam due to laser induced emission of photons. In an additional stage, the pre-amplified beam is guided onto the second dye cell which again causes amplification due to laser induced emission. This results in roughly 20 mJ per laser pulse.

The amplified beam is guided into the third stage of the laser system which is the THG unit. The 615 nm beam illuminates a BBO[5] crystal in order to produce its second harmonic at 307 nm.[6] The 307 nm beam and the remaining 615 nm beam are guided onto another BBO crystal in order to mix the two frequencies. Frequency mixing of two laser beams of unequal wavelengths λ_1 and λ_2 is another effect caused by the the non-linear susceptibility of the BBO crystal and results in photons at a wavelength λ_3 which satisfies [Rei04]

$$\frac{1}{\lambda_1} + \frac{1}{\lambda_2} = \frac{1}{\lambda_3}\,. \tag{4.1}$$

This results into the desired laser beam at 205 nm. However, for the frequency doubling and frequency mixing to be efficient, the *phase matching* condition needs to be fulfilled. This means that the wave vectors of the incident and produced beams need to satisfy the relation

$$\mathbf{k}_{\lambda_1} + \mathbf{k}_{\lambda_2} = \mathbf{k}_{\lambda_3}\,, \tag{4.2}$$

where $\mathbf{k}_{\lambda_1}$ and $\mathbf{k}_{\lambda_2}$ refer to the incident beams and $\mathbf{k}_{\lambda_3}$ refers to the frequency doubled/mixed beam. In case of frequency doubling, $\mathbf{k}_{\lambda_1} = \mathbf{k}_{\lambda_2}$. This relation is not fulfilled in general as the refractive index of BBO is wavelength dependent and the crystal is birefringent. In order to fulfil the phase matching relation, both BBO crystals are attached to step motors which alter the angle between the crystal optical axis and the laser beam in such a way that the phase matching relation is fulfilled which reflects in maximum energy per pulse of the produced beam. When changing the fundamental wavelength, the incident angles have to be adjusted due to the wavelength dependence of the refractive index. This is implemented and automatized within the laser operation software. Ultimately, 205 nm laser pulses at over 1 mJ per pulse can be produced with this system. However, it was

---

[4] For simplicity, it is referred to as 615 nm laser beam in the following.

[5] Barium borate, $Ba(BO_2)_2$

[6] Meaning between 303 nm and 314 nm

found that such high UV energies lead to localized heating within the frequency mixing crystal as light at this wavelength is absorbed slightly by BBO. This results in a loss of phase matching. Therefore, during the measurements shown in this work, the pump laser is operated at lower energy per pulse such that the UV output is kept at 600 µJ per pulse. In addition, the crystals are heated and stabilized at a temperature of 60 °C in order to increase the stability of the phase matching. The whole laser system needs a warm up time of around 1 h in order for the output energy per pulse to be stable. In this time, the temperatures of the internal components and the dyes equilibrate. In this state, the spread of energies was measured to be below 10 % whereas the UV beam profile was observed to be elliptical in the vertical direction with diameters of roughly 5 mm × 3 mm. Ordinary plain paper is used to observe the UV laser as it causes fluorescence on the paper. The accessible wavelength range of the UV output is between 202 nm and 209 nm. Within the laser setup, the laser beams at 615 nm and 307 nm are filtered out via an arrangement of four dichroic mirrors which exclusively reflect light at 205 nm while the other components pass the mirrors onto beam dumps.

Optical arrangement

The laser system is mounted on an optical table together with additional optics which are necessary for the TALIF diagnostic. The optical arrangement is depicted in figure 4.2. The laser beam is deflected by using dielectrically coated mirrors (*Laseroptik GmbH*) which have an experimentally determined reflectivity of 97 % for an incident angle of 45°. The reflectivity decreases strongly for other angles such that they can only be used for deflections of 90°. Different deflection angles are achieved by using right angle prisms (*Thorlabs*).

After the laser exit, the 205 nm laser beam is guided onto a variable attenuator which consists of a $\frac{\lambda}{2}$ plate (*Artifex Engineering*) followed by a Rochon polarizer (*Edmund Optics*). If linearly polarized light is guided onto a $\frac{\lambda}{2}$ plate, it introduces a phase shift of π between the two polarization components parallel and orthogonal to the crystal optical axis of the $\frac{\lambda}{2}$ plate. This causes a rotation of the polarization axis of the incident light which can be controlled by rotating the $\frac{\lambda}{2}$ plate around the optical axis. The Rochon polarizer consists of two connected birefringent MgF_2 crystals which are shaped and oriented in such a way that vertically polarized light passes the optic unaffected while horizontally polarized light is deflected with a slight angle of ~ 1.5°. In combination, the ratio of the vertically and horizontally polarized light is altered by the $\frac{\lambda}{2}$ plate which regulates the amount of light

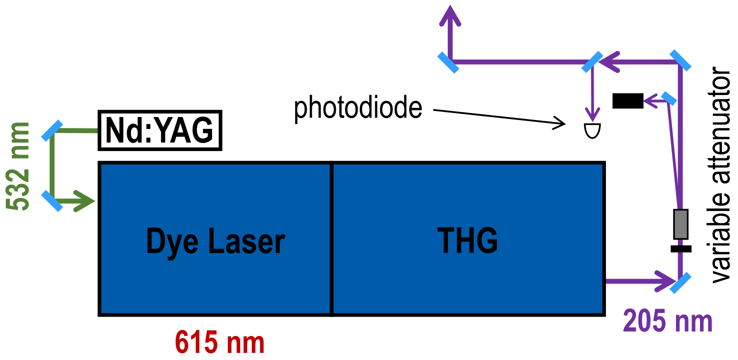

Figure 4.2: *Arrangement of the laser system in combination with the other optical components.*

unaffected by the Rochon polarizer. The vertical components is used for TALIF while the deviated light is guided into a beam dump. With this, the laser output can be attenuated from 72 % to below 5 % without changing operation parameters of the laser which is beneficial for the pulse-to-pulse stability of the laser system. The maximum transmission is limited as the optics are not anti-reflection coated such that this loss is inevitable. The $\frac{\lambda}{2}$ plate is mounted in a motorized optic holder (*Thorlabs:* SM1 Optics Rotator Kit) such that the rotation angle can be remotely controlled with high precision.

An UV fused silica window (*Thorlabs:* WG41050) is used as beam splitter. Its transmission is specified to be ~ 90 % such that around 5 % of the laser beam are reflected by the fused silica surface. That share of the light is guided onto a photodiode (*Alphalas GmbH*) in order to measure the time resolved laser intensity which is necessary to normalize the TALIF signal according to equation (3.8). For this it is assumed that the average laser intensity within the volume that is observed by the fluorescence collection optics is proportional to the measured photodiode current. A diffusor (*Thorlabs:* DGUV10-220) is used in order to protect the photodiode from overexposure. The diode has a bandwidth of > 1 GHz and is connected parallel to a 50 Ω resistor to an oscilloscope (*LeCroy:* LT264) with a bandwidth of 350 MHz. The oscilloscope measures the voltage across the resistor. With this combination, it is possible to resolve the laser pulse shape (length: several ns) to a satisfying degree. The main beam is guided towards the experiment.

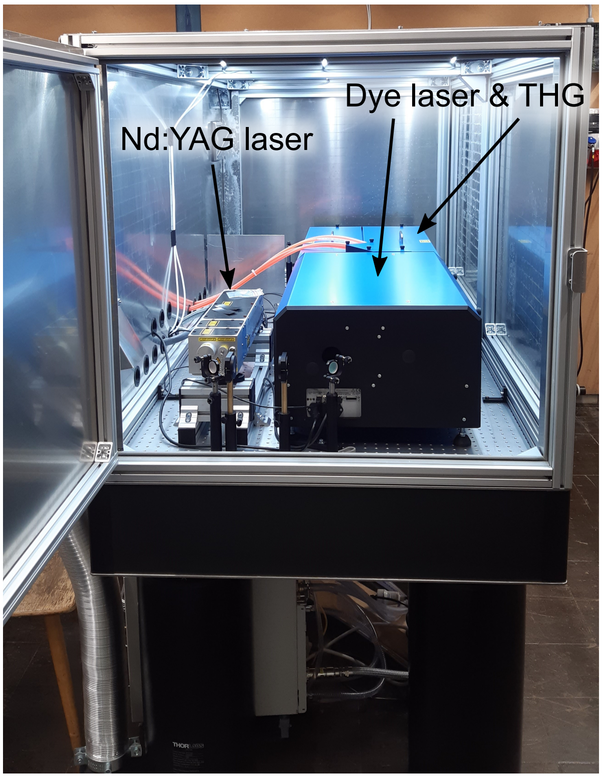

Figure 4.3: *Photograph of the laser inside the laser safety enclosure.*

Laser enclosure

As the laser is located in the BATMAN Upgrade operation hall, the whole hall needs to be closed if the laser is operated openly due to laser safety regulations. This is connected with considerable effort and interferes with the regular operation of the teststand. This is why the whole optical system is completely enclosed by a box made of stainless steel. A photograph of the construction can be seen in figure 4.3. The system could be accessed with doors which are connected with the interlock system of the Nd:YAG laser such that the laser stops operation as soon as one of the doors opens.

Laser operation

The Nd:YAG laser is operated with a computer program provided by the manufacturer which controls the pumping diodes, the Q-switch and the water cooling. The energy per pulse can be altered by changing the time delay between the pump laser diodes and the Q-switch. Another computer program is used in order to operate the dye laser and the THG unit. With this, the wavelength of the laser system and the phase matching can be controlled manually. The wavelength setting of the laser was calibrated before delivery such that its specified value is used for the line profile measurements in this work. In addition, LabVIEW routines are available to implement the dye laser control in home made programs.

5 TALIF characterization and results at ALFRED

5.1 The small scale experiment ALFRED

The TALIF system is first set up and characterized at the small scale experiment *ALFRED* (**A**nother **Pl**anar radio **fre**quency **d**ischarge). ALFRED is designed as ICP without Faraday shield and was constructed in the course of this work as a simple plasma experiment with easy access for diagnostics. It is based on the two similar plasma experiments ACCesS [FF14, HFF22] and PlanICE [MFB+21] which have the same geometry and operate within the same pressure and RF power range such that comparable plasma parameters are expected. ALFRED is built close to the laser system such that the laser can be used both for ALFRED and BATMAN Upgrade at the same position. A CAD explosion graph of ALFRED is depicted in figure 5.1. The plasma vessel is made of stainless steel and has a diameter of 153 mm and a height of 100 mm. The top and bottom end of the vessel are equipped with ISO-K DN 160 flanges and the bottom plate is a ISO-K DN 160 blind flange. In order to allow access to the plasma, eight tubes (4 × 28 mm diameter, 4 × 44.5 mm diameter) are attached to the vessel which are terminated with four ISO-KF DN 40 flanges at the larger and four ISO-KF DN 25 flanges at the smaller tubes. Quartz windows with a diameter of 40 mm are attached to the ISO-KF DN 25 flanges for optical diagnostics. The top plate is a Al_2O_3 ceramic plate with a diameter of 170 mm and a thickness of 5 mm. Al_2O_3 was chosen as it blocks the 205 nm laser light and therefore ensures laser safety. For this, the setup needs to be light-tight in general.

A vacuum pump system is connected to one of the ISO-KF DN 40 flanges. It consists of a rotary vane pump and a turbomolecular pump (pumping rate: 110 l/s) from the manufacturer *Pfeiffer*. This results in a background pressure on the order of 5×10^{-7} mbar. The gas inlet is located on the opposite side of the vessel at another ISO-KF DN 40 flange. Two calibrated mass flow controllers are

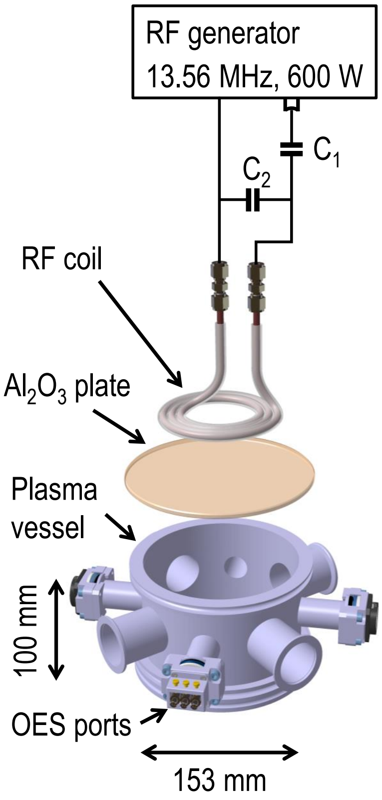

Figure 5.1: *CAD explosion graph of the small scale experiment ALFRED. CAD created by Andreas Oberpriller.*

attached to the gas inlet where one supplies Kr of He gas whereas the other is connected either to a H_2 or D_2 gas bottle. The gas pressure in the vessel can be controlled via a manual gate valve which is located between the plasma vessel and the vacuum pumps. For measuring the pressure, two pressure gauges are attached to the vessel. A combined cold cathode/pirani vacuum meter (*Leybold:* PENNINGVAC PTR 90 N) with a broad accessible pressure range is used in order to determine the background pressure whereas a capacitive pressure gauge (*Pfeiffer:* CMR375) is used to give a more exact value during plasma operation. The vessel is cooled with cooling water in order to prevent the sealing rings from melting. For this, copper tubes are attached to the bottom plate and the two ISO-K DN 160 flanges at the top and the bottom of the plasma vessel.

The plasma is generated with the aid of a planar coil which is located above the Al_2O_3 plate and has 2.75 windings. It consists of a copper tube which is enclosed with plastic in order to ensure insulation between the windings. The coil is connected to an RF generator which operates at 13.56 MHz and has a maximum output power of 600 W. Two tunable capacitors ($C \in [10\,\mathrm{pF}, 300\,\mathrm{pF}]$) between RF generator and coil are used to match the impedance of the coil and the plasma to the generator impedance (50 Ω) in order to prevent the RF power from being reflected back into the RF generator. The capacitors are arranged in the γ-type configuration. A Faraday shield is not used for the experiment in order to increase the coupling efficiency of the RF power to the plasma. In order to ensure inductive coupling, the forwarded RF power is increased during the startup phase of the experiment until the plasma operation jumps from the CCP mode into the ICP mode which is accompanied by a sudden increase in radiation due to the higher n_e value in inductive coupling mode.

In this work, the experiment is operated at pressures between 10 Pa and 2 Pa at RF output powers below 430 W. In this range, the electron temperature is observed to be above 2 eV for all operation parameters such that the plasmas operated in ALFRED are ionizing.

5.1.1 TALIF implementation

Laser connection to ALFRED

Figure 5.2 shows the beam path of the laser in ALFRED. It is focussed into the plasma vessel with a UV fused silica lens with a specified focal length of 500 mm (*Thorlabs*). At $\lambda = 205$ nm, the focal length was measured to be shorter at ~ 430 mm and the lens is positioned in such a way that the focal point is in the center of the vessel. This is the position with the highest laser intensity such that it is chosen as observation volume for the fluorescence. For this, a lens system consisting of two achromatic lenses (*Edmund Optics*) is mounted to one of the ISO-KF DN 25 flanges. The close achromatic lens has a focal length of 175 mm and is mounted such that its focal point coincides with the laser focus. In that way, the acceptance solid angle for the fluorescence photons is maximized. The second achromatic lens has a focal length of 85 mm and is used to focus the fluorescence light onto a fibre (diameter: 1 mm) which is connected to a photomultiplier (PMT). Between the two lenses, a band pass filter can be inserted in order to filter the fluorescence radiation against any background radiation. For the Kr fluorescence, a filter at 830 nm ± 10 nm (*Thorlabs:* FL830-10) is used and for the H fluorescence the used filter transmits at 650 nm ± 40 nm (*Thorlabs:* FB650-40).

The PMT (*Hamamatsu:* H11706-20) is used in order to observe the fluorescence radiation timely resolved. For this it is connected in parallel to a 50 Ω resistor to

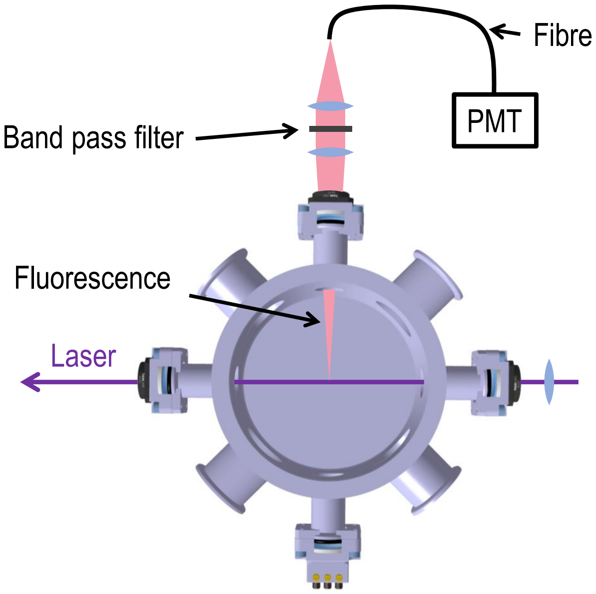

Figure 5.2: *Beam path of the laser inside ALFRED and arrangement of the fluorescence optics. CAD created by Andreas Oberpriller.*

the oscilloscope. The PMT has a specified rise time of 0.57 ns which translates to a bandwidth of roughly 600 MHz [Tho18]. The gain of the PMT (i. e. the proportionality constant between incident radiative power and PMT output current) is variable over almost three orders of magnitude. Its maximum average output current is 100 µA such that the average voltage measured at the oscilloscope must not be larger than 5 mV in order to prevent saturation of the PMT. In the case of the H_α background radiation during H_2 plasma operation, this is ensured by setting the gain to a value where this condition is met.

TALIF signal acquisition and evaluation

The principle of the signal acquisition and processing for the TALIF measurements is shown schematically in figure 5.3. Using the oscilloscope the waveforms of the photodiode $U_{\mathrm{PD}}(t)$ and the PMT signal $U_{\mathrm{PMT}}(t)$ are acquired. The oscilloscope is triggered to a trigger signal provided by the Nd:YAG laser power supply which occurs 200 ns before the laser pulse. Both waveforms are acquired for 300 consecutive laser pulses and an average over all acquisitions is taken. Afterwards, the present offsets are subtracted for both averaged waveforms.

Figure 5.4 shows two acquired signals of the PMT (upper graph) and the photodiode (lower graph) after performing offset correction. Here, TALIF was

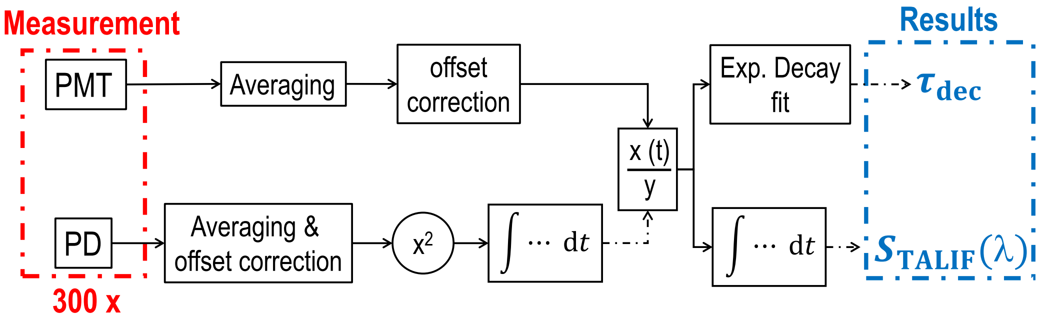

Figure 5.3: *Concept of the acquisition and processing of the PMT and photodiode data for the TALIF diagnostic. Full lines denote waveforms while dashed dotted lines denote scalars. PD: photodiode, PMT: photomultiplier.*

performed on a H_2 plasma in ALFRED at a pressure of 10 Pa and 370 W of applied generator power while the laser was operated at 205.08527 nm. An exponential decay function was fitted to $U_{\mathrm{PMT}}(t)$ revealing a decay time of 14.1 ns[1]. The decay behaviour of $U_{\mathrm{PMT}}(t)$ is described very well by the expected exponential decay function which reinforces the choice of the used hardware and the acquisition procedure for the PMT voltage. $U_{\mathrm{PD}}(t)$ reveals a FWHM of the laser pulse of 6.3 ns which matches very well with the specification of the laser manufacturer of 6 ns considering the elongation of the signal caused by the finite bandwidth of the photodiode and the oscilloscope. In the waveform, oscillations are apparent at 225 ns and 250 ns. These are probably caused by oscillations inside the acquisition circuit of the photodiode due to the fast voltage ramp up due to the laser. In order not to corrupt the measurement, the integration of $[U_{\mathrm{PD}}(t)]^2$ is performed in the interval $[t_{\mathrm{max}} - 10\,\mathrm{ns}\,, t_{\mathrm{max}} + 10\,\mathrm{ns}]$, where t_{max} is the time point of the maximum value of U_{PD}.

The photodiode waveform is squared and numerically integrated over time. The result of this treatment corresponds to $\int_0^\infty \langle I(t) \rangle^2 \,\mathrm{d}t$ in equation (3.8). $U_{\mathrm{PMT}}(t)$ is divided by this value which forms the intensity calibrated PMT voltage. Fitting an exponential function to this resulting waveform yields the decay time τ_{dec} of the excited state. The TALIF signal corresponding to $S_{\mathrm{TALIF}}(\lambda)$ in equation (3.8) is formed via

$$S_{\mathrm{TALIF}}(\lambda) = \int \left[\frac{U_{\mathrm{PMT}}(t)}{\int_0^\infty (U_{\mathrm{PD}}(t))^2 \,\mathrm{d}t} \right] \mathrm{d}t\,, \tag{5.1}$$

---

[1] The H atoms decay time as a function of operation parameters is further discussed in chapter 5.2.3

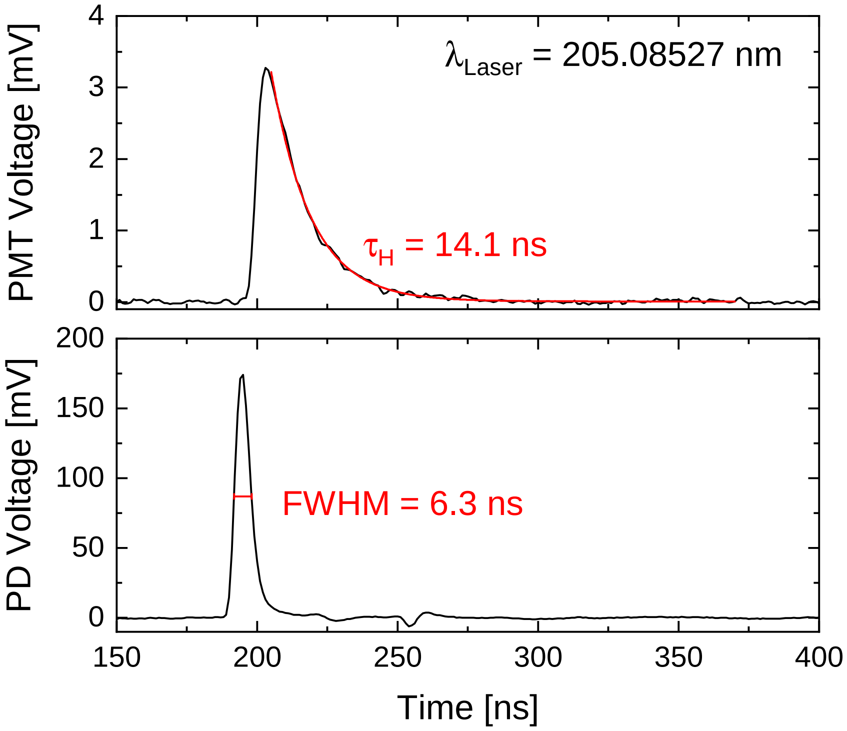

Figure 5.4: *Acquired waveforms from the photodiode and the PMT after taking the average of 300 waveforms and performing the offset correction. PD: photodiode, PMT: photomultiplier.*

where the numerical integration is performed over the whole waveform. This procedure is repeated for multiple wavelengths in order to capture the full two-photon absorption line profile. For TALIF on H, the step size between two consecutive wavelength values is 0.4 pm while for TALIF on Kr, the step size is 0.2 pm. With these, a sufficient resolution of the two line profiles can be achieved. For the acquisition of one H atom line profile, 41 wavelength steps are necessary while 51 steps are required for one Kr profile. The signal acquisition and wavelength change is fully automatized within a LabVIEW program which was developed for this work. For the evaluation, a python script is used. The acquisition of one hydrogen line profile takes roughly 5 minutes and is mainly limited by the duration of the wavelength change of the laser and the connectivity between the used PC and the oscilloscope.

5.1.2 Additional diagnostics

Optical emission spectroscopy

OES is applied to ALFRED as outlined in chapter 2.4 by measuring the emissivities of the Balmer lines α to ϵ as well as the Q branch of the diagonal transitions of the Fulcher-α band. From these, the plasma parameters T_{gas}, n_{e}, T_{e} and n_{H} are determined. In order to determine the role of photon re-absorption concerning the evaluation of the emission data with the CR model, both optically thin and optically thick datasets are used for this. The obtained values of n_{e} and T_{e} are used to give context to the TALIF measurement while the resulting n_{H} from OES is explicitly compared to the TALIF results. As the recorded emissivities are line of sight averaged values, also the resulting n_{e}, T_{e} and n_{H} should be treated as such. n_{e} and T_{e} generally exhibit a considerable local variation due to the presence of the sheath. H atoms recombine predominantly at the vessel wall such that their average lifetime is given by the time scale of diffusion allowing them to distribute evenly among the whole plasma volume. The n_{H} values as obtained by TALIF and OES can thus be compared. The application of the CR model is not part of this work but has been carried out by [Bri22]. The temperature T_{H} obtained with TALIF is compared to T_{gas} obtained by OES. As the latter reflects the ground state rotational population of H_2 molecules, it is denoted as molecular temperature T_{H_2} in the following.

The used spectrometer is a high resolution spectrometer (*Princeton Instruments:* Acton SpectraPro SP-2750). It is equipped with a reflection grating with 1800 grooves/mm, has a focal length of 0.75 m and its apparatus profile has a FWHM of 15 pm at 600 nm. A CCD camera is connected to the spectrometer in order to record the spectra. The light from the plasma is collected with an optical fibre which is on the one side connected to the entrance of the spectrometer and the other side is connected to a lens head which is attached to ALFRED. The viewing cylinder of the spectrometer has a diameter of roughly 5 mm and is slightly diverging towards larger distance. Figure 5.5 shows the location of the LOS in ALFRED. The lens head is attached on the opposite side of the fluorescence collection optics such that the LOS crosses the experiment horizontally through its symmetry axis. The system is calibrated for the Balmer lines α (at 656 nm) to ϵ (at 397 nm), between 600 nm and 636 nm for the Fulcher transition and between 805 nm and 860 nm for observing a Kr plasma. The obtained emissivities are associated with a relative error of ±10 %.

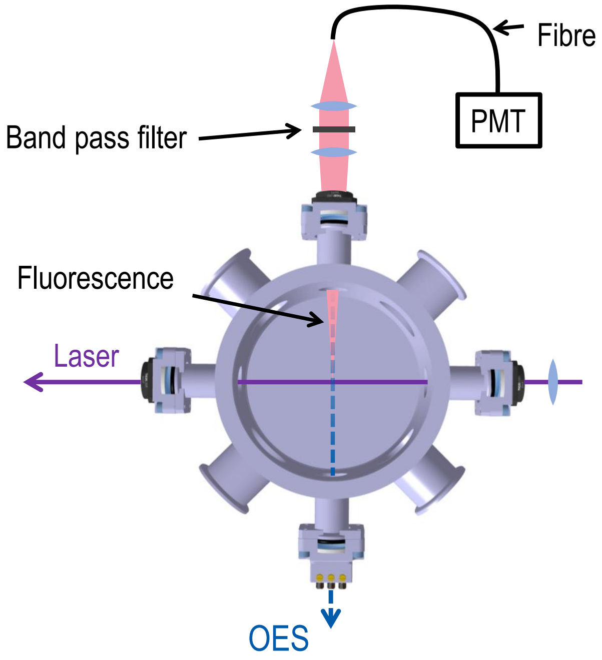

Figure 5.5: *Lines of sight of the OES, fluorescence collection optics and beam path of the laser used for TALIF. CAD created by Andreas Oberpriller.*

Coupling efficiency

The power P_{plasma} which is coupled to the plasma is generally not equal to the power P_{gen} which is supplied by the RF generator. This is due to ohmic losses within the electric lines and the RF coil as well as induced eddy currents in the vicinity of the RF coil. The share of RF power which is eventually coupled to the plasma is devoted as *coupling efficiency* η and is calculated via [Hop94]

$$\eta = \frac{P_{\mathrm{plasma}}}{P_{\mathrm{gen}}} = \frac{P_{\mathrm{gen}} - \frac{1}{2} I_0^2 R_{\mathrm{net}}}{P_{\mathrm{gen}}} \,. \tag{5.2}$$

I_0 is the amplitude of the current through the RF antenna and R_{net} is the network resistance which represents the sum of all ohmic losses in the RF network. In order to determine η, all of these parameters need to be measured. P_{gen} is measured by the internal electronics of the RF generator and I_0 is determined with a Rogowski coil positioned around one of the lines connected with the RF coil during plasma operation. R_{net} is determined while there is no running plasma discharge which is suppressed by stopping gas feeding to the vessel. In this configuration, a low RF power is applied from the RF generator and the generated I_0 is measured. This is repeated for various power values. The network resistance can be determined by plotting the supplied RF power as a function of $\frac{1}{2} I_0^2$ and performing linear regression on the data. R_{net} is given by the slope of this fit [BZRF22]. For ALFRED, the measured R_{net} value is about $0.19\,\Omega$.

This method generally overestimates the losses due to eddy currents as the screening effect of the plasma is not present during the determination of R_{net}. This means that the determined coupling efficiency can be understood as a lower limit. Hereafter, the stated power values are to be understood as power coupled to the plasma if not specifically stated otherwise. Typical values of the coupling efficiency at ALFRED range between 70 % and 82 %.

5.2 Characterization of the TALIF system

The TALIF system was purchased and assembled newly in the course of this work. Thus, a characterization of the system is necessary which is also used for optimizing the implementation of TALIF at BATMAN Upgrade. For this, the fluorescence collection system is investigated as well as exemplary TALIF measurements at H and Kr are shown. Finally, measurement errors are assigned to the determined properties.

5.2.1 Calibration of the fluorescence collection optics

Equation (3.9) gives the expression for the calculation of n_{H} from recorded TALIF signals. The part of that expression which depends on the fluorescence collection system are the ratios of the transmissions of the fluorescence detection system T_{Kr} and T_{H} as well as the detector sensitivities ξ_{Kr} and ξ_{H} evaluated at the wavelengths of the H atom and Kr fluorescence transitions.

The fluorescence collection system consists of the window which limits the plasma vessel, the lens system consisting of two achromatic lenses, the band pass filters, the optical fibre and the PMT. For the transmission of the collection system, the first four parts are relevant. The vacuum window is made of fused silica and the transmission is specified in its data sheet [Qio22] to be equal at the two wavelengths of the H and Kr fluorescence, 656.3 nm and 826.3 nm. The same holds for the achromatic lenses, which are specified in [Edm22]. The optical fibre has a specified attenuation of 3 dB/km at 656.3 nm and 12 dB/km at 826.3 nm [Tho22]. At a fibre length of 5 m, this translates to a transmission of 99.7 % and 98.6 %

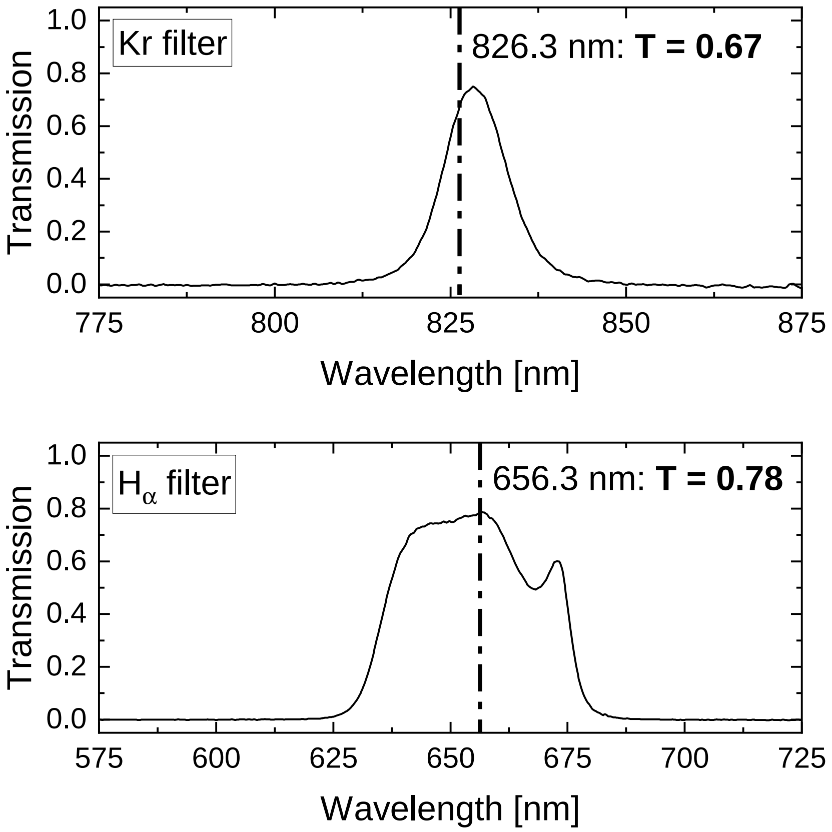

Figure 5.6: *Measured transmission of the two spectral filters used for the measurement of the fluorescence radiation.*

respectively. The spectral filters were calibrated with a Ulbricht sphere. For this the emission of the Ulbricht sphere is measured with a survey spectrometer (*Plasus:* SA Series) with and without the filters being inserted in the optical path. The transmission of one filter is given by dividing the spectrum obtained with the filter being inserted by the spectrum obtained without the filter. The result of this is shown in figure 5.6 for the two employed filters. At the wavelengths of the H and Kr fluorescence, the respective transmissions are 0.78 and 0.67 which differs significantly from the specified values of 0.68 and 0.52.

With this information, the detection system transmission ratio for the two wavelengths can be calculated. It is given by

$$\frac{T_{\mathrm{Kr}}}{T_{\mathrm{H}}} = 0.85\,.$$

The sensitivity of the PMT is characterized by the quantum efficiency of the PMT and its gain. Here, the quantum efficiency corresponds to the average number of electrons which are generated per impinging photon and the gain is the total electron amplification factor. As long as the gain is kept constant for a measurement on hydrogen and the corresponding calibration with krypton only the quantum efficiency is relevant for the detector sensitivity. The quantum efficiency is specified by the PMT manufacturer [Ham22] and the ratio of its values at the two observed wavelengths is $\frac{\xi_\mathrm{Kr}}{\xi_\mathrm{H}} = 0.5$. However, as seen for the filter transmission the specified values can deviate significantly for the specific device such that this ratio is assigned with a high error bar. Therefore, a calibration of the quantum efficiency ratio is carried out. This is done by observing a krypton and a hydrogen plasma with the PMT and comparing the measured voltages U^x_PMT ($x = \mathrm{H}, \mathrm{Kr}$) with spectra recorded by the absolute calibrated spectrometer. U^x_PMT is given by

$$U^x_\mathrm{PMT} \propto \epsilon^x_\mathrm{tot} \cdot \xi_x \,, \tag{5.3}$$

where ϵ^x_tot is the total plasma emission reaching the PMT. For this, it is assumed that this emission is originating only from a wavelength interval for that ξ_x is constant. In order to ensure this, the spectral filters are inserted in the fluorescence collection system during the measurements. The ratio of PMT sensitivities is then given by

$$\frac{\xi_\mathrm{Kr}}{\xi_\mathrm{H}} = \frac{U^\mathrm{Kr}_\mathrm{PMT}}{U^\mathrm{H}_\mathrm{PMT}} \cdot \frac{\epsilon^\mathrm{H}_\mathrm{tot}}{\epsilon^\mathrm{Kr}_\mathrm{tot}} \,. \tag{5.4}$$

The recorded spectra are depicted in figure 5.7 (a) and (b). In addition, the transmission of the respective used spectral filters as well as the resulting emission reaching the PMT is shown. For hydrogen, almost 90 % of the emission reaching the PMT is originating from the H_α transition whereas for krypton, 85 % of the radiation originates between 825 and 830 nm. Thus for both investigated spectra, the emission reaching the PMT is predominantly within a narrow spectral region. On the other side, the specified quantum efficiency of the PMT varies on a broader spectral scale [Ham22] of many 100 nm. Therefore, the assumption described prior is considered to be valid. The total emission reaching the PMT is $\epsilon^\mathrm{Kr}_\mathrm{tot} = 1.42 \times 10^{21}\,\mathrm{m}^{-3}\mathrm{s}^{-1}$ for the Kr plasma and $\epsilon^\mathrm{H}_\mathrm{tot} = 3.60 \times 10^{20}\,\mathrm{m}^{-3}\mathrm{s}^{-1}$.

The oscilloscope was used in order to measure the PMT voltage. The results are $U^\mathrm{Kr}_\mathrm{PMT} = 2.53\,\mathrm{mV}$ and $U^\mathrm{H}_\mathrm{PMT} = 2.83\,\mathrm{mV}$. Inserting these values into the above formula yields

$$\frac{\xi_\mathrm{Kr}}{\xi_\mathrm{H}} = 0.22 \,. \tag{5.5}$$

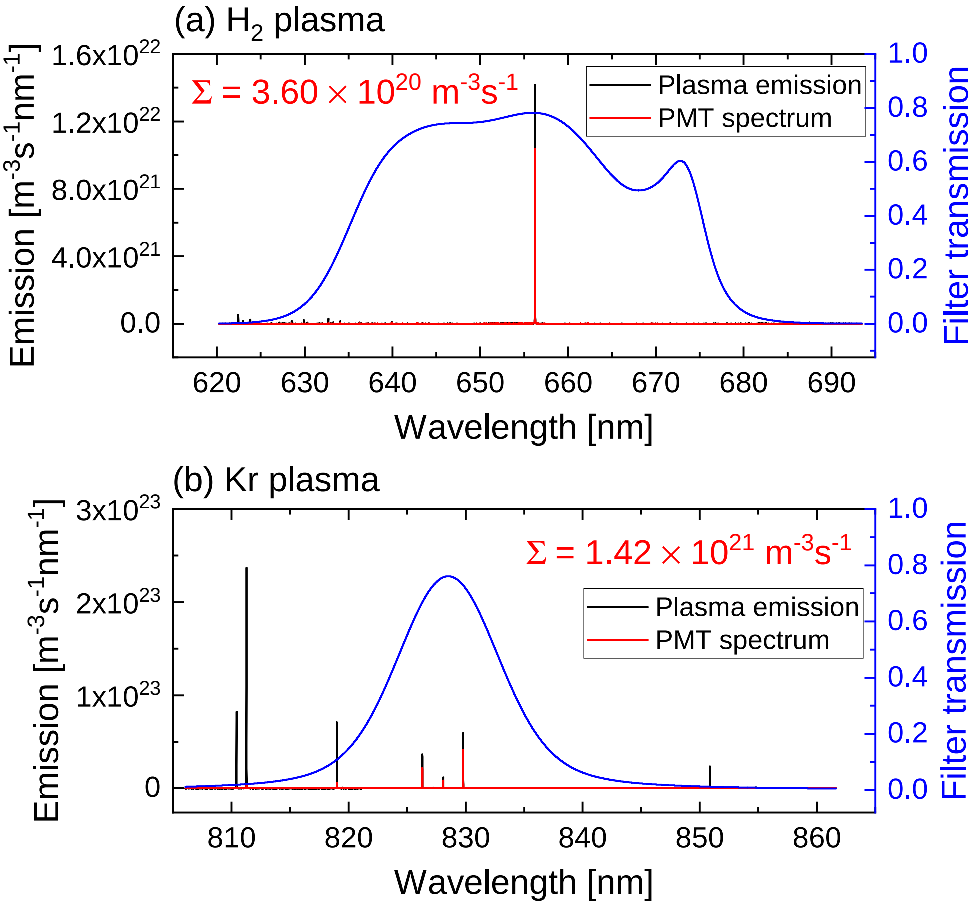

Figure 5.7: *Measured emission and spectrum reaching the PMT from (a) a* H_2 *plasma and (b) a Kr plasma. The transmission of the respective spectral filters is depicted for both spectra.*

This value is considerably smaller than the specified ratio of 0.5 underlining the necessity of such a calibration. Knowing the ratios of the detection system transmission and sensitivity, quantitative TALIF measurements are possible.

5.2.2 TALIF on krypton

Krypton line profile

TALIF on krypton is performed in order to calibrate the diagnostic enabling for the determination of absolute n_H values. For this, the line profile of the Kr two-photon transition is recorded which corresponds to a plot of $S_\mathrm{TALIF}^\mathrm{Kr}$ as a function of the laser wavelength. The TALIF measurements for this were performed at the two krypton pressures of 1 Pa and 10 Pa. The resulting normalized line profiles are depicted in figure 5.8. The measured line profiles are visibly non-Gaussian and

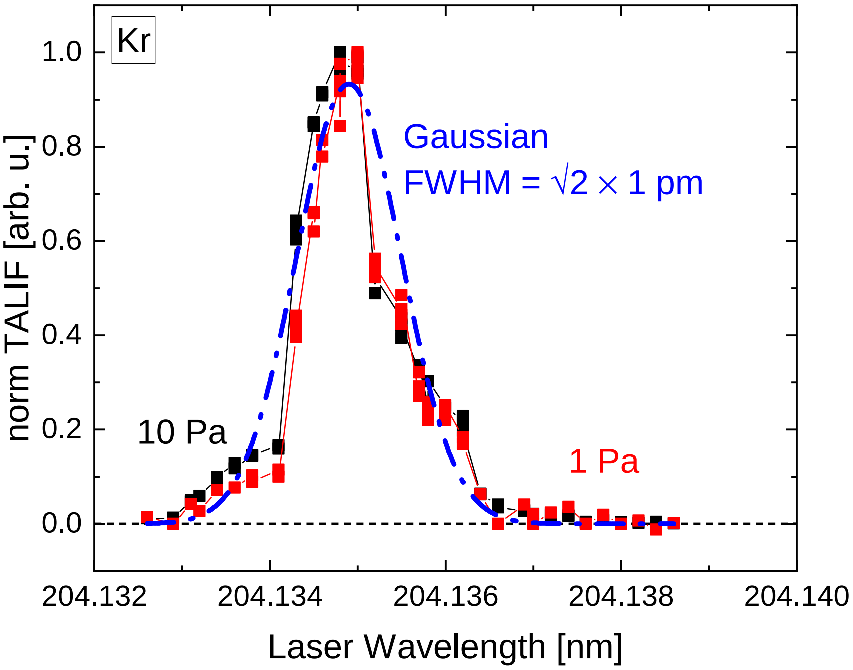

Figure 5.8: *Normalized two-photon absorption line profiles for Kr at the pressures of 1 Pa and 10 Pa. For comparison, a Gaussian with a FWHM of* $\sqrt{2} \times 1$ *pm is depicted.*

exhibit strong features both at their upper and lower edge. These features do not depend on the pressure within the investigated pressure interval.

According to equation (3.10), this measured profile is given by the double convolution of the two-photon absorption profile of krypton with the laser line profile. Taking equation (3.13) yields a FWHM between 0.27 pm and 0.28 pm of the Kr line profile arising from Doppler broadening which is considerably smaller than the width of the measured line profile which is $\gtrsim 1$ pm. The width of the structures is therefore dominated by the laser linewidth which is however specified to be 0.6 pm by the manufacturer. A possibility would therefore be that an energetic shift of the $5p'\,[3/2]_2$ level depending on the isotope could explain the apparent clearly non-Gaussian structure. This level is the upper level of the probed two-photon transition. Krypton gas consists of the isotopes ^{78}Kr (0.35 %),^{80}Kr (2.25 %), ^{82}Kr (11.6 %), ^{83}Kr (11.5 %), ^{84}Kr (57 %) and ^{86}Kr (17.3 %). However, comparing the $5p'\,[3/2]_2$ energies as specified in [Sal07] for the two isotopes ^{84}Kr and ^{86}Kr (which make up almost three quarters of the Kr composition on earth) reveals an energy difference which corresponds to a shift of 0.13 pm in wavelength of the two-photon transition which is one order of magnitude smaller than the structure size.

This leaves the laser itself as the cause of the apparent spectral shape caused by the presence of multiple laser modes. Multiple laser modes are possible, if the laser condition is met for multiple wavelengths [Rei04]. These modes are also subject of inter-mode mixing in the course of the frequency doubling and mixing in the THG unit such that a non-trivial mode structure results in the laser emission [Sir21].

As the laser line profile is clearly not Gaussian, equation (3.11) can generally not be applied in order to determine the H atom two-photon absorption line width $\Delta\lambda_{2\text{PA}}^{\text{H}}$. However, it is possible to estimate the influence of the laser line profile on the measured H atom line profile based on equation (3.10). For this, a Gaussian line profile with the FWHM of $\Delta\lambda_{2\text{PA}}$ (representing a Doppler broadened H atom line profile at a set of reasonable temperatures) is convoluted twice with the laser line profile. The broadening caused by this convolution can be quantified by fitting another Gaussian to the result yielding the resulting FWHM $\Delta\lambda$. Putting these into equation (3.11) and solving for $\Delta\lambda_{\text{Laser}}$ gives an *effective* laser linewidth which accounts for the broadening of the two-photon absorption line due to the laser line profile. With that, equation (3.11) can be applied despite the laser line profile not being Gaussian.

As the krypton line profile at room temperature is reasonably narrow compared to the measured line profile, figure 5.8 represents approximately the convolution of the laser line profile with itself. The described procedure can therefore be performed by simply convolving the Gaussian with the profile from figure 5.8. Doing this yields an effective laser linewidth of $\Delta\lambda_{\text{Laser}} = (1 \pm 0.1)$ pm. In figure 5.8, a Gaussian with a FWHM of $\sqrt{2} \times 1$ pm is depicted representing the expected profile for a laser with $\Delta\lambda_{\text{Laser}} = 1$ pm. The factor $\sqrt{2}$ stems from the double convolution of the laser line profile with itself. Such a Gaussian fits reasonably well to the observed line profile. Further, the structure of the laser line profile does not alter the resulting two-photon line profile shape. This is is because the H atom two-photon line profile for a temperature of 650 K is 3.75 pm. Using equation (3.11) gives $\Delta\lambda = 4$ pm which corresponds to a broadening by 7 % such that the laser line profile is almost negligible compared to the H atom two-photon line profile. For the evaluation of the H atom temperature, equation (3.11) is therefore used with $\Delta\lambda_{\text{Laser}} = (1 \pm 0.1)$ pm for the line profile correction.

Scan of the laser energy per pulse

The quadratic regime for krypton can be identified by performing TALIF measurements on krypton while varying the energy per laser pulse. This was done at

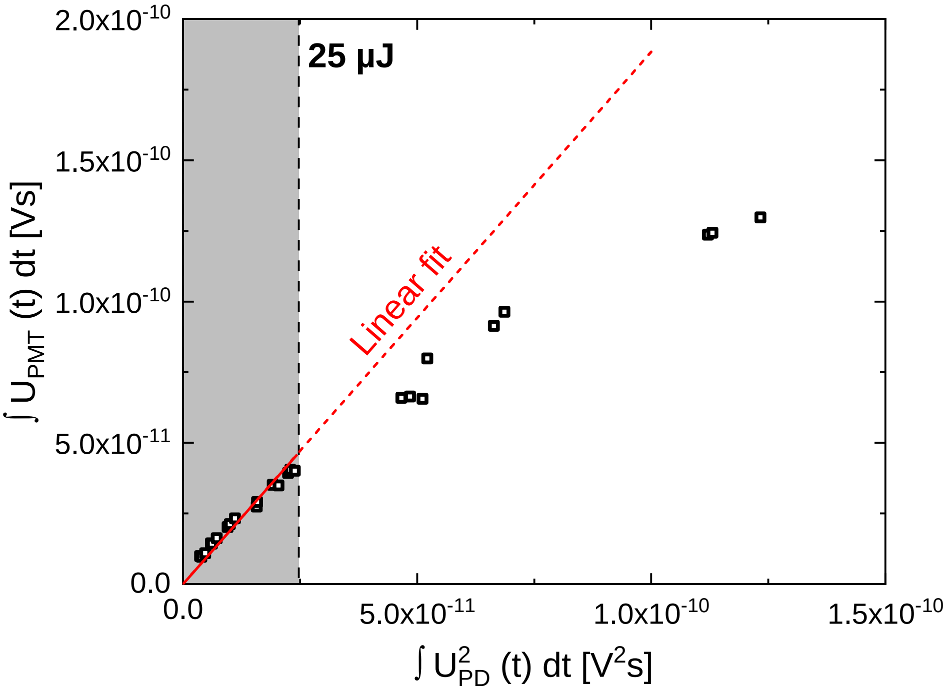

Figure 5.9: *Integrated PMT Voltage from TALIF on krypton as a function of* $\int [U_{PD}(t)]^2\,dt$ *and a linear fit to the data in the linear regime (grey shaded area).*

a Kr pressure of 6 Pa and the result is depicted in figure 5.9. This figure shows the integrated PMT voltage $\int U_{\mathrm{PMT}}(t)\,\mathrm{d}t$ as a function of $\int [U_{\mathrm{PD}}(t)]^2\,\mathrm{d}t$. In the quadratic regime, the correlation between the two quantities is linear which is the case for the grey shaded area at low energies below 25 µJ. This is illustrated by a linear fit to the data points. At high energies, the saturation of the TALIF signal is apparent. The physical reason of the saturation in the case of TALIF on krypton is evaluated in [GAP+21] and its reason is attributed to photon-induced ionisation of the excited atoms. For calibration, the TALIF measurements are therefore always performed at energies below that value.

Decay time of the fluorescence signal

In order to exclude quenching as a source of uncertainty in the TALIF measurements on krypton, the decay time of the $5p'\,[3/2]_2$ state was measured for the krypton pressure range between 1 Pa and 10 Pa, whereas the result is depicted in figure 5.10. For the whole pressure scan, the energy per laser pulse was kept at 13 µJ. The decay time is constant for the whole investigated pressure range and very close to the value of $\tau_{\mathrm{Kr}} = 28.5$ ns which is specified by [NIST]. Therefore, quenching of the $5p'\,[3/2]_2$ state is not apparent in the investigated pressure range

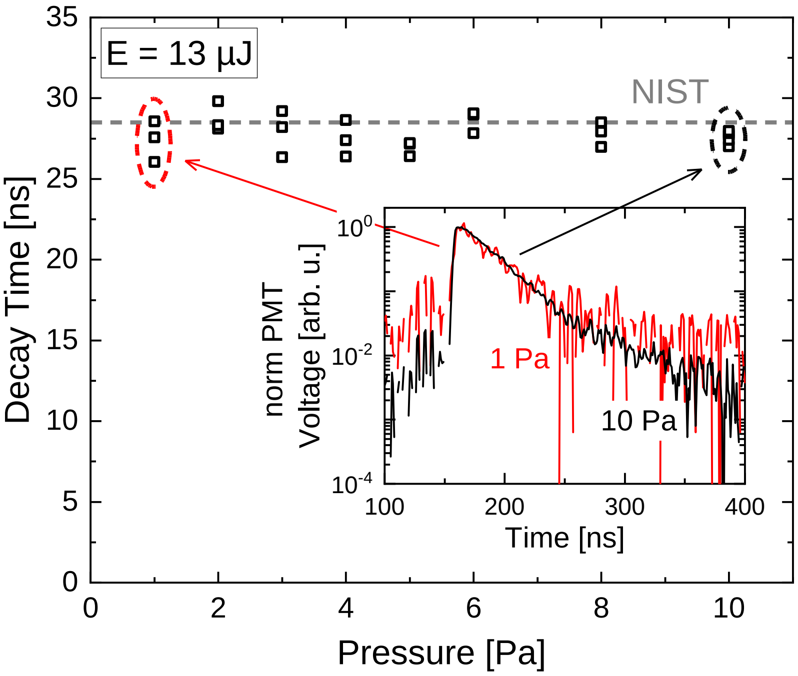

Figure 5.10: *Measured life time of the* $5p' \, [3/2]_2$ *state as a function of Kr pressure and exemplary normalised PMT signals for the pressures 1 Pa and 10 Pa.*

which validates the calculation in chapter 3.4.1. In addition, figure 5.10 shows two normalised PMT voltages which exhibit the same shape and can be well described by a single exponential decay function.

5.2.3 TALIF on hydrogen

H atom line profile

For the determination of n_{H}, the line profile of the two-photon transition is measured. This is done equivalent to the measurements on krypton by plotting $S^{\mathrm{H}}_{\mathrm{TALIF}}$ against the used laser wavelength. An exemplary line profile measurement is shown in figure 5.11. Here, a H_2 plasma at a pressure of 10 Pa and a plasma power of 300 W was investigated. In addition, a Gaussian fit to the TALIF data points is depicted. The shown profile is wider than the found laser line profile such that its shape is dominated by the Doppler broadened line profile of the two-photon transition. Given this, the good match between the fit and the data means that the H atoms clearly follow a Maxwell-Boltzmann energy distribution. This is observed for all measured spectra in the investigation at ALFRED. The FWHM $\Delta\lambda$ of the measured profile is determined as a result of the fitting procedure and has a value of 3.95 pm in the shown case. The Doppler FWHM $\Delta\lambda_{\mathrm{2PA}}$ is

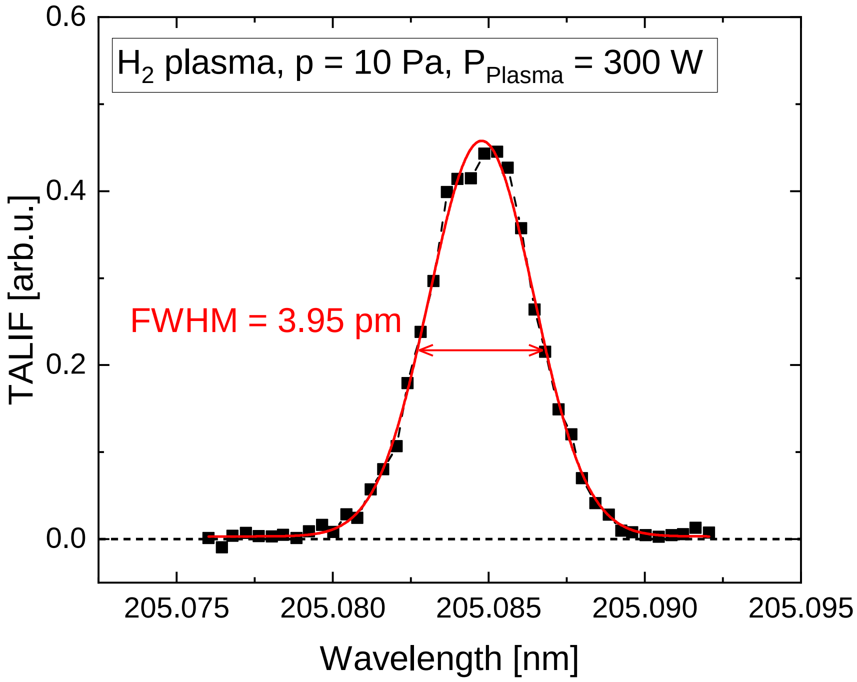

Figure 5.11: *Two-photon absorption line profile for Hydrogen atoms and a Gaussian fit to the data.*

determined by applying equation (3.11) with the previously examined value of $\Delta\lambda_{\mathrm{Laser}}$. Inserting the result into equation (3.13) and solving it for the H atom temperature T_{H} gives

$$T_{\mathrm{H}} = \left(\frac{\Delta\lambda_{\mathrm{2PA,Dop}} \cdot c}{\lambda_0^{(2)}} \right)^2 \cdot \frac{m_{\mathrm{H}}}{8\,\ln(2)\,k_{\mathrm{B}}}\,, \tag{5.6}$$

which is 650 K in the shown case. n_{H} is determined by taking the integral of the line profile.

Scan of the laser energy per pulse

The quadratic regime for TALIF needs to be determined on hydrogen as well. Figure 5.12 shows the integrated PMT voltage $\int U_{\mathrm{PMT}}(t)\,\mathrm{d}t$ as a function of $\int [U_{\mathrm{PD}}(t)]^2\,\mathrm{d}t$. The measurement was performed at a H_2 plasma at 5 Pa and a plasma power of 275 W. The stability of the plasma during the measurement was checked by observing the plasma with a survey spectrometer. For an energy per laser pulse below 100 µJ, the correlation between the two values is linear such that the quadratic regime is located in this energy region. In figure 5.12, this is illustrated by a linear fit to these data points. At higher energy per laser pulse,

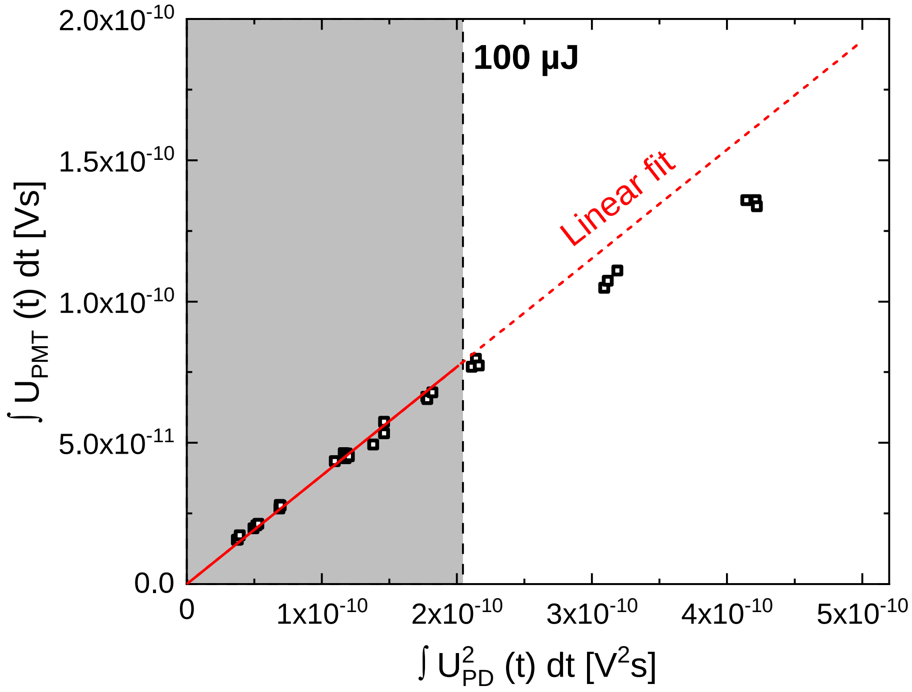

Figure 5.12: *Integrated PMT Voltage from TALIF on hydrogen as a function of* $\int [U_{PD}(t)]^2\, dt$ *and a linear fit to the data in the grey shaded area.*

the PMT data deviates from this fit. TALIF is therefore performed at a laser energy per pulse of 80 µJ for the measurements at ALFRED.

Decay Time of the Fluorescence signal

For TALIF on H atoms, the decay time of the fluorescence signal is of special relevance since it gives knowledge about the branching ratio which is necessary for the calculation of the absolute H atom density as it is described in chapter 3.4.1. In the literature, multiple values for the fluorescence decay time for the same TALIF scheme have been communicated, which are for example 17.6 ns [NSD01], 10 ns [vdHBM+00, BMB+02] or 20.9 ns [BKHMJ88]. These are explained by the presence or absence of l state mixing. Throughout the measurements conducted in this work, the measured fluorescence decay times varied between 11 ns and 14 ns. Thus, the presence of state mixing and therefore the branching ratio needs to be assessed more closely. This is done by plotting the measured fluorescence decay times throughout this work against the measured H atom density in the corresponding plasmas which is shown in figure 5.13. The measurements were performed at H_2 plasmas at varying pressure (marked in blue), a mixture of

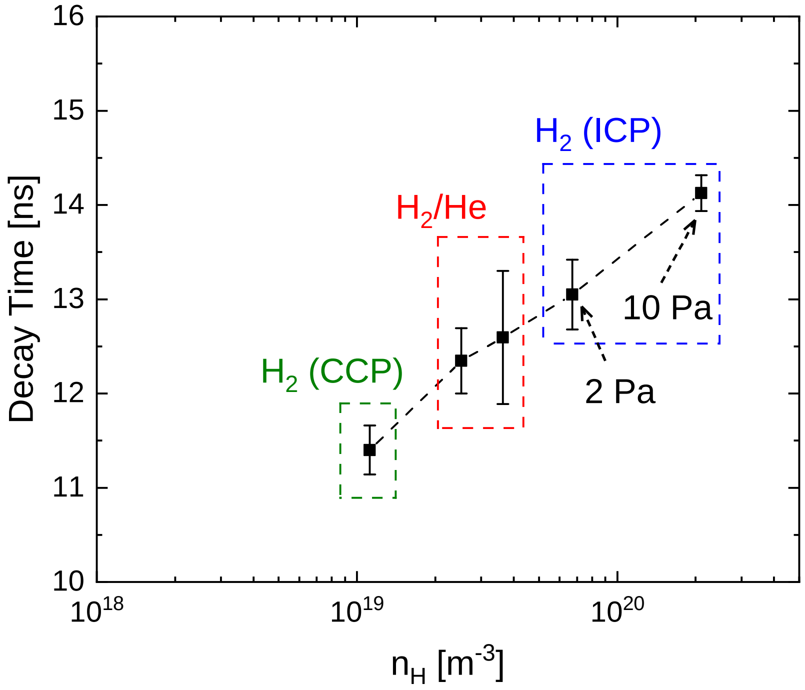

Figure 5.13: *Measured decay time of the detected H atom fluorescence signal as a function of the H atom density as determined with TALIF. ICP: inductively coupled plasma, CCP: capacitively coupled plasma.*

H_2 and helium as working gas (marked in red)[2] and an H_2 plasma operated in capacitive coupling mode (marked in green) exhibiting low n_e values and a low dissociation degree.

From the figure it is apparent, that the fluorescence decay time increases from 11.5 ns to above 14 ns with increasing atomic hydrogen density. Such behaviour has also been observed in the literature [vdHBM+00, Ell20]. In [vdHBM+00], a cascaded arc plasma has been investigated. Here, the photon re-absorption of Lyman-β photons is given as the probable reason for this behaviour. They are emitted by H atoms in the $3^2P_{1/2}$ and $3^2P_{3/2}$ states which are previously populated via state mixing. The photon re-absorption causes the Lyman-β photons to be trapped inside the plasma which effectively causes an elongation of the life time of $n = 3$ H atoms [Iro79b, Phe58]. This effect is stronger for an increasing density of ground state hydrogen atoms.

In [Ell20], the transition of a capacitively coupled plasma to an inductively coupled plasma by increasing the applied RF power at constant pressure yields an increase of the fluorescence decay time which is similar to figure 5.13. In this

---

[2] The results of the two campaigns are shown in more detail in the following chapters 5.4 and 5.3

case, no state-mixing is assumed and the increase of the fluorescence decay time is attributed to a lesser influence of collisional quenching when the plasma is in inductive coupling mode. In that mode, the density of H_2 molecules which act as quenching partner is argued to be smaller. This explanation does not hold for the data shown in 5.13 since for example the increase of the fluorescence decay time for the H_2 plasma in inductive mode (blue region) was observed for increasing the pressure from 2 Pa to 10 Pa at constant power leading to an increasing density of hydrogen molecules. In contrast, the effect of increased quenching should lower the fluorescence decay time. This is why quenching is ruled out for the τ_H behaviour leaving the explanation given in [vdHBM+00] of photon re-absorption prolonging τ_H. Therefore, also perfect l state-mixing is assumed for the evaluation of the H atom density with the according branching ratio of 0.441.

However, from the presence of photon re-absorption follows inevitably a change of the branching ratio as it effectively reduces the transition strength of the Lyman-β transition [Phe58, SCBL02]. This can be visualized by computing the H_α branching ratio $a(\mathrm{H}_\alpha)$ while applying the escape factor method following equation (2.34) as is done in [Phe58]:

$$a(\mathrm{H}_\alpha) = \frac{g_s \cdot A^s_{\mathrm{Bal}-\alpha} + g_p \cdot A^p_{\mathrm{Bal}-\alpha} + g_d \cdot A^d_{\mathrm{Bal}-\alpha}}{g_s \cdot A^s_{\mathrm{Bal}-\alpha} + g_p \cdot A^p_{\mathrm{Bal}-\alpha} + g_d \cdot A^d_{\mathrm{Bal}-\alpha} + g_p \cdot A^p_{\mathrm{Ly}-\beta} \cdot \Theta} \,. \tag{5.7}$$

Here, g_i $(i = s, p, d)$ are the statistical weights of the fine structure states with $l = 0, 1, 2$, $A^i_{\mathrm{Bal}-\alpha}$ $(i = s, p, d)$ are the corresponding Einstein coefficients for the H_α transition, $A^p_{\mathrm{Ly}-\beta}$ is the Einstein coefficients for the Lyman-β transition and Θ is the escape factor accounting for the weakening of the Lyman-β transition. The population of the fine structure states with $l = 0, 1, 2$ is assumed to follow their statistical weights due to perfect state-mixing. In the extreme case of complete radiation trapping (i. e. $n_\mathrm{H} \to \infty$ and therefore $\Theta \to 0$), the branching ratio of the H_α transition is 1. The corresponding expected fluorescence decay time is 22.7 ns. These numbers correspond to the case when disregarding the Lyman-β transition, thus only considering the H_α transition for radiative decay. For declining influence of photon re-absorption, the value of Θ rises and approaches 1 causing a decrease of $a(\mathrm{H}_\alpha)$. In the other extreme of photon re-absorption not at all playing a role (i. e. $n_\mathrm{H} \to 0$ and therefore $\Theta \to 1$), a branching ratio of 0.441 with the corresponding fluorescence decay time of 10 ns is expected.

The value of Θ in the experiment could be assessed by solving the Holstein-Biberman equation [MO99]. This integro-differential equation takes the three-dimensional shape of the excitation region, the geometry of the plasma experiment as well as the spatial distribution of ground state H atoms into account. For these, not all data is available such that calculations rely on assumptions and the non-trivial geometry makes them computationally very expensive such that this treatment is not carried out in this work. As the measured fluorescence decay times are closer to the optically thin case ($\tau_\mathrm{H} = 10\,\mathrm{ns}$), a branching ratio of 0.441 is used for the n_H calculation throughout this work. However, it should be noted, that the true branching ratio is likely to be higher, such that the shown n_H values correspond to an upper limit of the density.

5.2.4 Measurement uncertainty

In order to assess the uncertainty of the n_H measurement, each term in equation (3.9) needs to be evaluated individually. Generally, two kinds of errors can be distinguished: the *systematic error* which emerges from the parameters at a fixed value and the *random error* which emerges from the quantities which are determined individually for each measurement. Therefore, the two errors are assigned with two separate error bars. For both kinds, the overall error bars are computed by following the Gaussian error propagation. The following error sources are considered for the systematic error bar:

- The transmissions of the band pass filters were determined in chapter 5.2.1 with an Ulbricht sphere and a survey spectrometer. The determined values are assigned with a relative uncertainty of ±10 %.

- The ratio $\frac{\xi_\mathrm{Kr}}{\xi_\mathrm{H}}$ of the PMT quantum efficiencies was also determined in chapter 5.2.1 after equation (5.4). Therefore, its total uncertainty emerges from the uncertainties of the single quantities. The resolution of the oscilloscope is 0.03 mV such that this value is used as ΔU for the measured voltages. The total emission of the plasma reaching the PMT is the product of the plasma emission as determined with the spectrometer and the transmission of the fluorescence collection optics. Both values are assigned with an uncertainty of ±10 % such that the relative emission uncertainty is 14 % following Gaussian error propagation. Thus, the relative uncertainty of $\frac{\xi_\mathrm{Kr}}{\xi_\mathrm{H}}$ is ±20 %.

- The relative uncertainty of $\frac{\sigma^{(2)}_\mathrm{Kr}}{\sigma^{(2)}_\mathrm{H}}$ is ±50 % according to [NSD01].

In total, this corresponds to a total uncertainty of $\frac{\Delta n_{\mathrm{H,sys}}}{n_{\mathrm{H}}} = 55\,\%$ accounting for the systematic error which consists mainly on the uncertainty of $\frac{\sigma^{(2)}_{\mathrm{Kr}}}{\sigma^{(2)}_{\mathrm{H}}}$. The systematic uncertainty has no influence on the relative behaviour of the displayed data points.

The random uncertainty consists of the following sources:

- The density of krypton atoms for calibration is deduced via the ideal gas law from the pressure measured with the capacitive pressure gauge under the assumption of the gas being at room temperature. This temperature is at 20 °C and varies within ± 3 °C within a day. The pressure gauge uncertainty is specified to be ±0.15 %. The uncertainty Δn_{Kr} is therefore ±1 %.
- For TALIF on hydrogen atoms, the spectral integration of $S^{\mathrm{H}}_{\mathrm{TALIF}}(\lambda)$ is carried out by fitting a Gaussian function to the line profile. The uncertainty of the integral is a direct result of the performed fitting routine. On average, a relative uncertainty of 10 % is obtained from this.
- For TALIF on krypton, the spectral integration of $S^{\mathrm{Kr}}_{\mathrm{TALIF}}(\lambda)$ is performed numerically from the obtained data points. The uncertainty of the integral was determined by performing multiple line profile measurements and computing the standard deviation of the data points. The result is a relative uncertainty of ±15 %.

This results in a total value of the uncertainty of $\frac{\Delta n_{\mathrm{H,rand}}}{n_{\mathrm{H}}} = 18\,\%$ accounting for the random error. The temperature of hydrogen atoms is determined after equation (5.6) from the Doppler FWHM which is in turn calculated after equation (3.11). The uncertainty of T_{H} is determined by Gaussian error propagation of the uncertainties of the FWHM of the measured line profile and the laser line width. The former is another result of the fitting applied to the line profile whereas the latter is estimated to be ±0.1 pm.

5.3 Measurements in H_2 plasmas

H atom density

The experiments on H_2 plasmas are carried out for a varying pressure between 2 Pa and 10 Pa while keeping the RF power coupled to the plasma at a constant value of $P_{\mathrm{plasma}} = 310\,\mathrm{W}$. For this, the forwarded RF power is adjusted accordingly

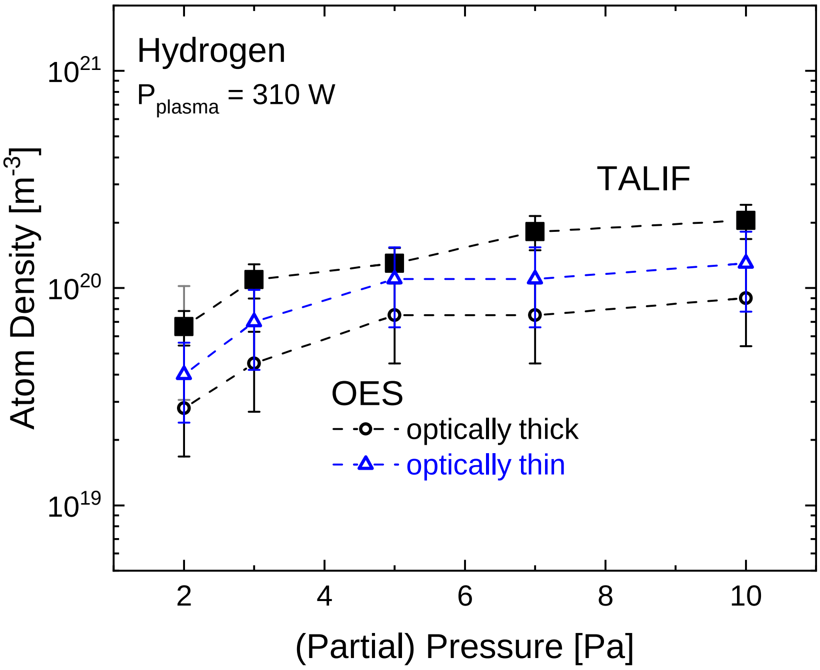

Figure 5.14: *H atom density measured via TALIF and OES (optically thick and optically thin) as a function of pressure.* $P_{plasma} = 310$ *W for all pressure points.*

for each pressure value which is necessary since the coupling efficiency rises from 70 % to 82 % for increasing pressure. The n_H values as measured both by means of TALIF and OES are depicted in figure 5.14. Regarding the TALIF results, the small error bars correspond to the random error, while the large error bar is the systematic error. The latter is shown as an example for the 2 Pa data point but it is assigned to all points. For OES both optically thick and optically thin results are shown.

n_H is found to increase by a factor of three with increasing pressure. This is observed by both diagnostics such that the relative trends found by TALIF could be well reproduced with OES. Concerning the absolute results, the TALIF values are within a range of $7 \times 10^{19}\,m^{-3}$ and $2 \times 10^{20}\,m^{-3}$. This is a factor of 2.5 higher compared to the optically thick OES result. This factor is constant throughout the pressure scan within the respective error bars. In order to assess this difference between the two diagnostics, a closer look has to be taken on the influence of photon re-absorption on the n_H value resulting from OES.

If photon re-absorption is not considered for the evaluation of the OES results, the resulting n_H value rises by a factor of 1.5 being therefore closer to the TALIF results as can be extracted from figure 5.14. This demonstrates the big impact of this effect on the n_H value which is obtained via OES. Its influence on the population of excited H atom states is twofold:

- The H atom state with $n = 2$ gains an additional population channel due to photon re-absorption such that the according calculated density increases drastically due to photon re-absorption [BF00]. This also applies to the state $n = 3$ but only to a lesser degree since the Einstein coefficient of the Lyman-β transition is smaller compared to the one of the Lyman-α transition.

- The H atom states with $n \geq 4$ are not directly populated by photon re-absorption since the according Einstein coefficient of their Lyman transitions are not sufficiently high. However, redistribution of excited atoms with $n = 2$ or $n = 3$ into those states leads to an additional population. Therefore also the population of the states with $n \geq 4$ is affected by photon re-absorption.

Overall, the presence of photon re-absorption therefore causes an increased population of all excited H atom states. In the OES evaluation, this causes that a lower n_H value is required to account for an observed emissivity of one of these states which therefore leads to a drop of the resulting n_H if photon re-absorption is considered. However, as the plasma is clearly opaque at the observed H atom density values (see for example [WBFF21]), the optically thick result is considered to be closer to reality. Nevertheless, an overestimation of the influence of photon re-absorption could cause an underestimation of n_H explaining the difference between the results obtained by TALIF and OES partly. This should vanish at low values of n_H such that a comparison of the two diagnostics in such a condition could quantify the this influence experimentally.

The TALIF result also suffers from uncertainties which have an influence on the absolute n_H value:

- The OES data lies generally on the edge of the systematic error bar which mainly consists of the uncertainty of $\frac{\sigma^{(2)}_\mathrm{Kr}}{\sigma^{(2)}_\mathrm{H}}$ as determined by [NSD01]. If in reality, this value is smaller than the stated value of 0.62, the resulting n_H from the TALIF measurement drops accordingly.

- TALIF as performed in this work overestimates the n_H value caused by the branching ratio in the n_H calculation. An overestimation by a factor of 2.5 is, however, not possible. This value would correspond to a fluorescence decay time of 22.5 ns that is clearly not observed. This is why the overestimation due to this reason is expected to be smaller.

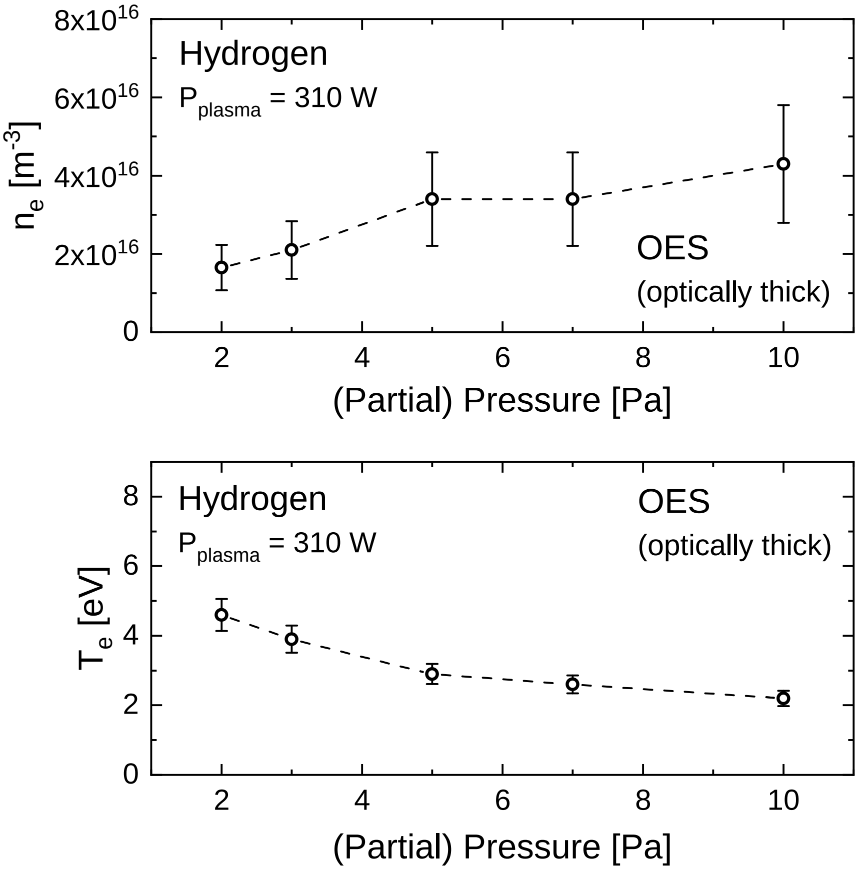

Figure 5.15: *Electron density and temperature measured via OES (optically thick evaluation) as a function of pressure.*

In context of these uncertainties, also the absolute values of the two diagnostics agree reasonably well.

Electron density and temperature

The n_e and T_e determined by OES are shown in figure 5.15. For the evaluation, the optically thick calculations of Yacora H and H_2 were used. Here, n_e is found to increase from a value below $2 \times 10^{16}\,m^{-3}$ towards above $4 \times 10^{16}\,m^{-3}$ for increasing pressure while T_e drops from 4.5 eV towards 2 eV. For the two pressure points at 5 Pa and 7 Pa, the measured n_e value is the same. This is due to the limited resolution in n_e of the performed forward calculations by Yacora H and H_2. The T_e drop follows the behaviour outlined in chapter 2.1.2. The rise in n_e can be explained by evaluating the power balance equation (2.18). As the power coupled to the plasma is kept constant throughout the pressure scan, the left hand side of

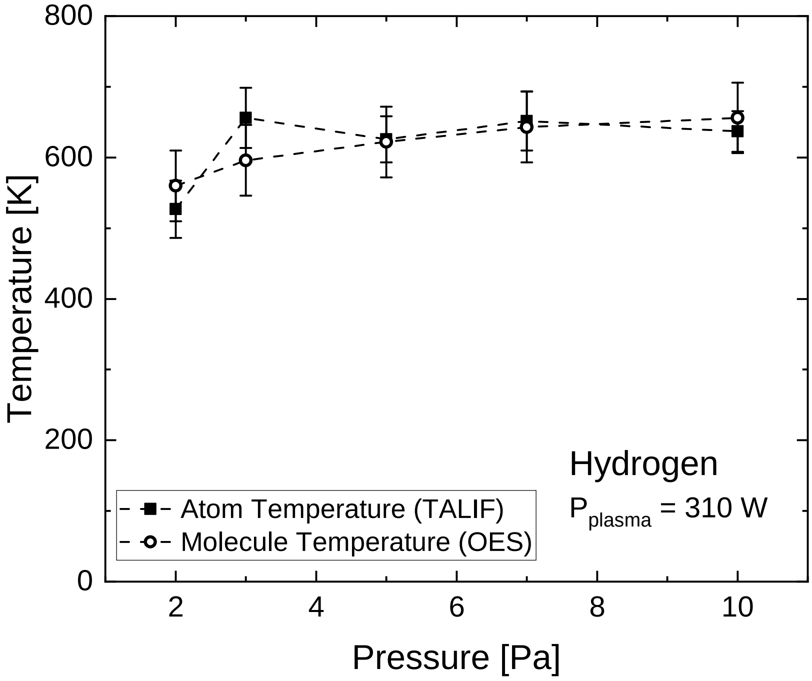

Figure 5.16: *H atom temperature (determined by means of TALIF) and H_2 temperature (determined by means of OES) as a function of pressure at constant power coupled to the plasma.*

the equation can be kept constant. In the right hand side, the T_e drop leads to a decrease of the reaction rates which needs to be compensated for by increasing n_e.

Atomic and molecular hydrogen temperature

The temperatures of hydrogen atoms and hydrogen molecules are depicted in figure 5.16. Both temperatures agree well within their respective error bars and have values between 550 K and 650 K throughout the pressure scan. The two species can thus be considered to be thermalized. The two temperatures rise throughout the pressure increase which can be attributed to an increasing number of collisions between the heavy particles and electrons. First, this causes increased dissociation of H_2 molecules which produces energetic H atoms (due to the Franck-Condon energy). As H and H_2 are thermalized, this causes a heating of all both particle species leading to an increased temperature. Secondly, the increased collisionality between electrons and heavy particles causes heating of the cold heavy particles due to elastic collisions.

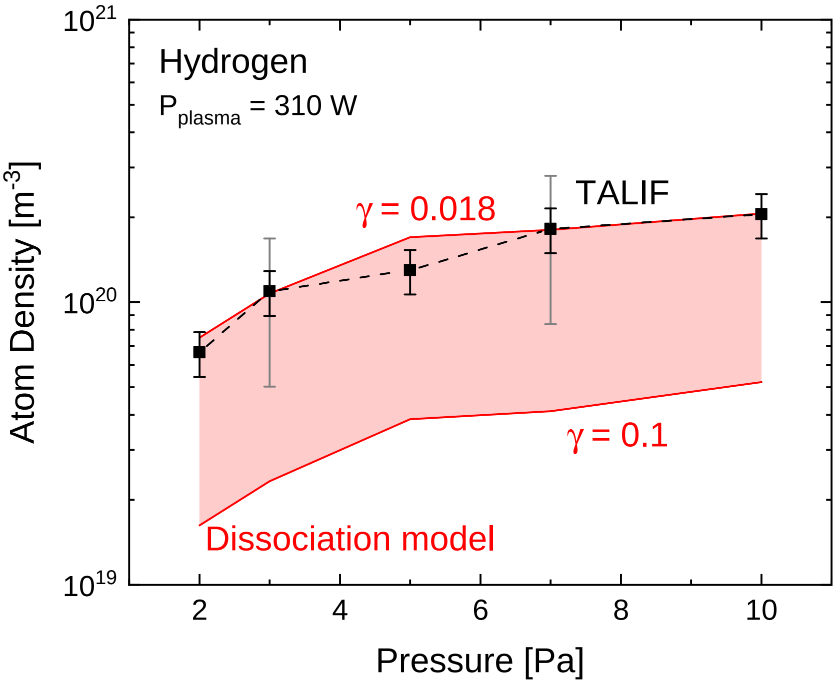

Figure 5.17: *Result of the n_H calculation of the dissociation model in comparison with the corresponding value as measured by TALIF.*

Discussion of the relative n_H behaviour

The obtained values of n_e and T_e can be utilised in order to explain the relative behaviour of n_H. For this, calculations with the dissociation model described in chapter 2.3.2[3] are performed and the n_H results are compared to the value as determined by TALIF. Subsequently, this comparison serves as a benchmark of the dissociation model itself. The experimentally determined n_e, T_e and T_{gas} as well as the operation pressure are used as input parameters of the calculations. An open parameter is the wall loss coefficient γ. Here, two different values are used. In ALFRED, the wall material of the vessel and the bottom plate is stainless steel, the top plate is made of Al_2O_3 ceramic and the windows are made of quartz. The value of γ depends mainly on whether the surface is metallic or dielectric, such that γ is comparable for quartz and Al_2O_3 ceramic. Metals generally exhibit a larger wall loss coefficient than dielectrics. The value of γ in ALFRED is expected to be a weighted sum of γ for all plasma facing materials. As a lower boundary, the wall loss coefficient $\gamma = 0.018$ after [YKC+21] is used which is determined for quartz as surface material. As an upper boundary, the value $\gamma = 0.1$ after [MM71, MDZ99] for stainless steel is chosen.

---

[3] The model calculations were carried out by [Bri22].

The results of the dissociation model calculation is depicted in figure 5.17 in comparison to the results from TALIF. Both model results follow the relative n_{H} behaviour as determined by TALIF very well. Concerning the absolute value, the larger one of the dissociation model results (corresponding to $\gamma = 0.018$) matches the TALIF results very closely. The value of γ has a very big influence and causes an absolute shift of the H atom density as can be seen in the figure where an increase of γ by a factor of five in turn causes a decrease of n_{H} by another factor of five. It is therefore the biggest source of uncertainty of the dissociation model. In addition, the model does not consider any spatial profiles of the plasma parameters as well as the effect of the surface temperature or impurities on γ are neglected. Further, also the variation of the H_2 dissociation cross section depending on the vibrational level is not included in the calculations. Considering these simplifications, also the absolute n_{H} values resulting from the model fit reasonably well to the results of the TALIF measurement.

5.4 Measurements in H_2/He plasmas

The investigation of plasmas consisting of mixture of H_2 and He is motivated twofold. Helium is chosen as gas admixture in order to lower the H atom density in the plasma as only a low H_2 content is chosen in the mixture. These low H atom densities can be used to investigate the discrepancy between TALIF and OES in the n_{H} determination further. Secondly, these low H atom densities are used in order to provide a regime with similar H densities as expected in BATMAN Upgrade. The capabilities of the TALIF system in the n_{H} determination in this regime are therefore of high relevance.

H_2 and He are fed into the plasma vessel simultaneously and experiments with H_2 admixtures of 5 % and 10 % are investigated. The total pressure is kept at 5 Pa and the forwarded RF power is 240 W for both discharges. This procedure results into the two partial hydrogen pressures 0.25 Pa and 0.5 Pa which are within the pressure range in which BATMAN Upgrade is operated.

A limiting factor regarding the TALIF capabilities was found to be the offset in the PMT signal caused by background radiation of the plasma. Helium has a transition at 667 nm which is within the spectral transmission interval of the H_α filter. The ratio of the fluorescence signal height to the background emission (TALIF-to-background ratio) was found to be 0.4 and 0.2 for the 10 % and 5 % H_2 admixtures respectively. At such low signals, the evaluation of the data acquired as described in chapter 5.1.1 was not possible due to the noise of the background radiation. This was overcome by increasing the number of considered laser shots for one acquisition to respective values of 500 and 1000. This causes an increase of the acquisition time of one hydrogen line profile to 9 min and 15 min respectively. The stability of the plasma during this time was verified with a survey spectrometer. Performing experiments at lower admixtures of H_2 was, however, not possible due to the even lower TALIF-to-background ratio.

H atom density

Figure 5.18 shows the result of the n_H measurements for the H_2/He plasma. The results of the H_2 plasma are shown for comparison. The density as measured by TALIF rises from $2.5 \times 10^{19}\,\mathrm{m}^{-3}$ to $3.5 \times 10^{19}\,\mathrm{m}^{-3}$ for the rising H_2 admixture whereas the result from OES is smaller by a factor of 1.6. This factor is smaller compared to the difference between TALIF and OES for the pure H_2 plasmas (i. e. 2.5) which can have two causes. Firstly, the influence of photon re-absorption on the results of Yacora H is smaller at lower n_H. An overestimation of this effect would therefore lead to a smaller underestimation of the resulting n_H value. Secondly, the branching ratio which is used for the TALIF evaluation alters due to photon re-absorption. If in this effect is less pronounced as is also indicated by the lower fluorescence decay time observed in figure 5.13, the true branching ratio is closer to the value of 0.441 which is used for the TALIF evaluation. The overestimation of n_H due to this reason is therefore less pronounced.

Electron density and temperature

Compared to the H_2 plasma, the resulting n_H values are smaller as expected. However, $n_\mathrm{H}/n_{\mathrm{H}_2}$ has values of 0.8 and 1.7 for the 10 % and 5 % H_2 admixtures respectively which is considerably higher when compared to the pure H_2 case which range between 0.2 and 0.4. This can be understood with the results of the n_e and T_e measurements, which are shown in figure 5.19 again compared to the results of the H_2 campaign. n_e is found to be in the same order of magnitude as for the lowest pressures in the H_2 plasma between $1 \times 10^{16}\,\mathrm{m}^{-3}$ and $2 \times 10^{16}\,\mathrm{m}^{-3}$. The smaller electron density at increasing H_2 admixture is caused as outlined in the evaluation of the power balance in chapter 2.1.2. A higher fraction of the molecular species H_2 in the He plasma opens an additional sink of power being vibrational excitation and dissociation such that a lower amount of power is left

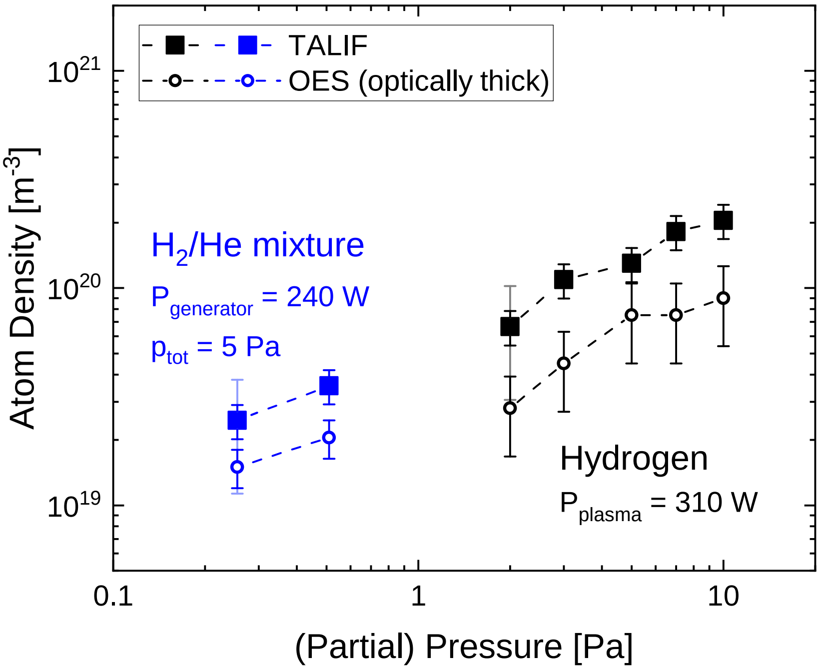

Figure 5.18: *H atom density measured via TALIF and OES (optically thick case) for the H_2/He mixture at two mixing ratios. The results of the campaign with H_2 plasmas are shown for comparison.*

for ionization leading to a reduction of n_e. T_e is considerably higher compared to the pure H_2 plasma with values around 7 eV for both H_2 admixtures. This is the cause of the high dissociation degree of H_2 molecules. The cause of this is in the differing ionization energies between HE and H. The value of this energy for helium atoms is 24.6 eV [NIST] which is considerably higher compared to atomic or molecular hydrogen (13.6 eV and 15.4 eV respectively). Fulfilling the ionization balance in chapter 2.1.2 requires therefore a high electron temperature as only then the ionization rate is sufficiently high. This is due to the small fraction of electrons reaching the kinetic energy of 24.6 eV at small T_e.

Atomic and molecular hydrogen temperature

The determined atomic and molecular hydrogen temperatures are shown in figure 5.20. Both temperatures are in the range between 400 K and 550 K whereas the atomic temperature tends to be lower than the molecular temperature.

If at all a difference between the atomic and molecular hydrogen temperature is expected, the atomic temperature is expected to be higher compared to the molecular temperature. This is due to the Franck-Condon energy of 2 eV which is released during dissociation as kinetic energy. Energy exchange collisions lead

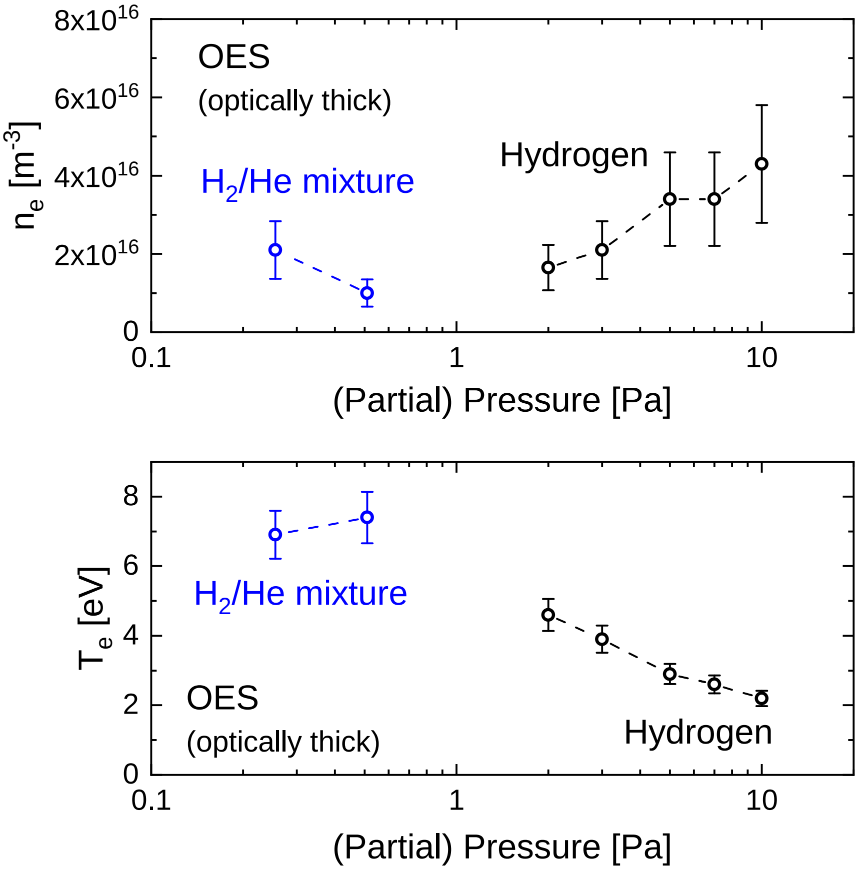

Figure 5.19: *Electron density and temperature measured via OES (optically thick case) for the H_2/He mixture at two mixing ratios. The results of the campaign with H_2 plasmas are shown for comparison.*

to a transfer of this energy to other heavy particles which eventually leads to thermalisation of heavy particles. If the collision rate between H atoms and H_2 molecules is not sufficient, they can not thermalise before wall recombination of H atoms. That would result in a higher H atom temperature compared to the H_2 temperature which is for example observed in [TDFP07]. However, in the observed H_2/He plasmas the opposite is the case and the cause of this is unknown. As the temperatures are close nevertheless, the temperature difference is attributed to the measurement uncertainty of the two temperatures and a common temperature is assumed.

5.5 Measurements in D_2 plasmas

In BATMAN Upgrade, plasmas are also operated with D_2 as this is the working gas which is foreseen for an NBI system in a fusion application. The effect of

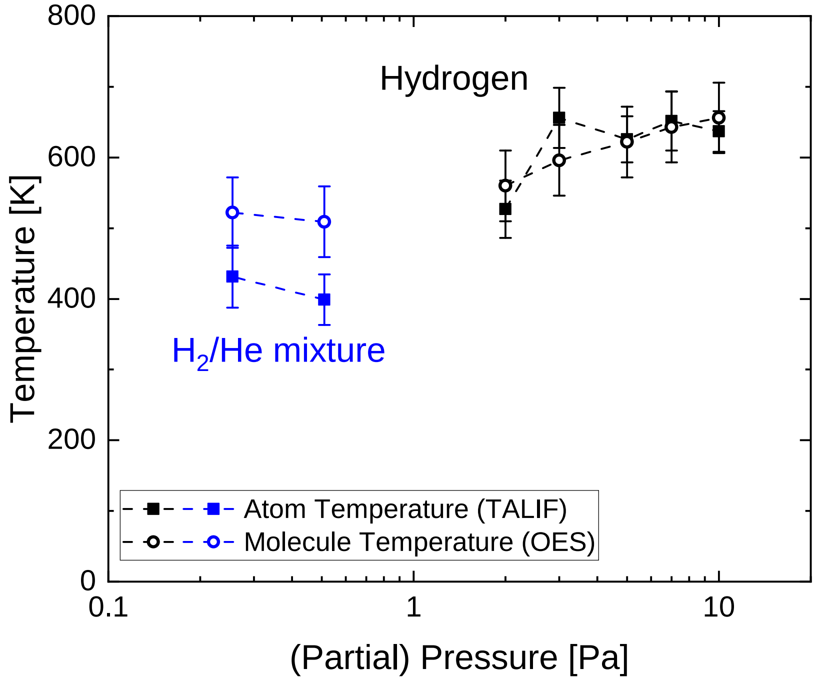

Figure 5.20: *H atom temperature (determined by means of TALIF) and* H_2 *temperature (determined by means of OES) for the* H_2*/He mixture at the two mixing ratios. The results of the campaign with* H_2 *plasmas are shown for comparison.*

changing the isotope on the atomic density is therefore a subject of investigation in ALFRED. For this, D_2 plasmas are operated at the three different pressure values of 2 Pa, 5 Pa and 10 Pa at a constant power coupled to the plasma of 215 W. P_{plasma} is lower in the deuterium campaign compared to the hydrogen campaign due to the brighter plasma emission causing saturation of the PMT at higher power values which has to be prevented.

For performing TALIF, the same transition is probed as for hydrogen. However, the absorption wavelength is shifted from 205.08 nm to 205.03 nm due to the isotopic shift of the energy level of the $n = 3$ levels. The two-photon absorption cross section $\sigma_{\mathrm{D}}^{(2)}$ as well as its ratio to the corresponding krypton cross section $\sigma_{\mathrm{Kr}}^{(2)}$ are assumed to be equal to the ones for hydrogen. This is justified as two-photon absorption is a process located in the electron shell such that changes of the nucleus are not expected to alter $\sigma^{(2)}$. The quadratic regime for performing TALIF is depicted in figure 5.21 which shows the integrated PMT voltage $\int U_{\mathrm{PMT}}(t)\,\mathrm{d}t$ as a function of $\int [U_{\mathrm{PD}}(t)]^2\,\mathrm{d}t$ for TALIF on D atoms. From this is apparent that the quadratic regime for deuterium is located at energies below 70 µJ. This value is smaller compared to the threshold value of 100 µJ which was found for TALIF on H. This threshold is determined by the validity regions of the two

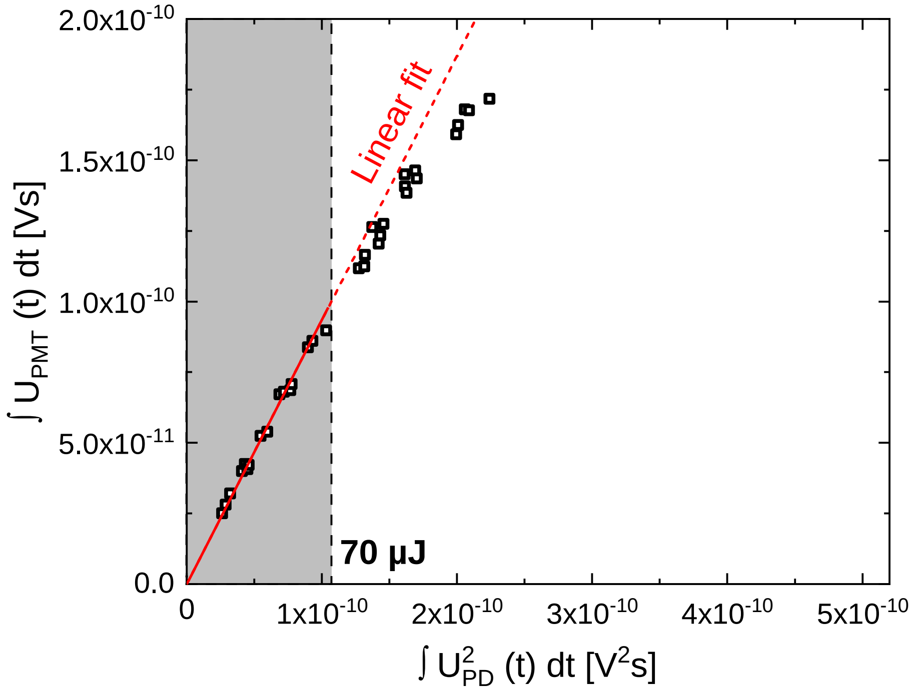

Figure 5.21: *Integrated PMT voltage from TALIF on deuterium as a function of* $\int [U_{PD}(t)]^2\,dt$ *and a linear fit to the data.*

conditions (3.21). The saturation region moves to smaller energies, if one of them is violated for a smaller energy per pulse. In this particular case, this means that either the excitation rate $R_{2\mathrm{PA}}$ or the photoionization rate Γ are higher for TALIF on deuterium compared to hydrogen.

In the case of Γ, equation (3.18) does not reveal an isotopic mass dependence. Thus, this contribution to saturation is equal for both isotopes. However, $R_{2\mathrm{PA}}$ is indeed larger in the case of deuterium as the absorption line profile $g(\lambda)$ depends on the mass of the absorbing particle. Its Doppler width is proportional to $\sqrt{\frac{1}{m_{\mathrm{H/D}}}}$ such that the profile is more narrow for deuterium at the same temperature and $g(\lambda)$ has a higher value in the line center. This would lead to a significant depopulation of the atomic ground state already at lower energy per laser pulse. On the other hand, this depopulation is only present for atoms with a velocity parallel to the laser beam $v_\parallel$ close to the according Doppler shifted laser wavelength according to equation (3.14). As the velocity distribution function of D atoms is more narrow due to the Doppler broadening, the amount of atoms within the relevant $v_\parallel$ interval is larger compared to hydrogen atoms. That would in turn lead to a larger necessary energy per laser pulse for ground state depopulation such that the two described effects cancel each other. For single photon laser absorption spectroscopy, this effect is known as the presence of *Bennet holes* in the VDF and it is studied extensively in [Shi83]. Also in this treatment, no isotopic mass dependence on the depopulation of the ground state is found. The lower boundary of the quadratic regime for TALIF on deuterium is thus not resolved, but the result of the measurement is treated as valid hereafter. For TALIF, the used energy per pulse is therefore 60 µJ for deuterium.

D atom density

The measured atomic deuterium density is shown in red in figure 5.22 whereas the results of the two previous campaigns are also depicted for comparison. n_D as measured with TALIF rises from just below $2 \times 10^{20}\,\mathrm{m}^{-3}$ to above $5 \times 10^{20}\,\mathrm{m}^{-3}$ which is higher by a factor of 2.5 compared to the corresponding hydrogen campaign despite a lower power coupled to the plasma denoting a strong isotope effect. This result compares well to other experiments at similar pressures where deuterium and hydrogen plasmas are compared [RBF17] as well as results from BATMAN [FSW13]. n_D as determined by OES is lower than the corresponding TALIF result by a factor of 3 to 3.5 throughout the pressure scan. The relative behaviour of n_D is very well reproduced by OES.

The factor between TALIF and OES is bigger for the D_2 plasma campaign compared to the H_2 plasmas. This bigger difference can have two causes. Firstly, the evaluation of the OES data is carried out with CR models which are only established for hydrogen. Changes of the cross sections of reactions involving deuterium molecules or molecular ions can result in an underestimation of n_D. Secondly, the absolute D atom density is bigger than the corresponding H atom density such that an underestimation of the atomic density by OES due to the presence of photon re-absorption is expected to be more pronounced. Lastly, the increased influence of photon re-absorption in the D_2 plasma also affects the true branching ratio of the D_α line in the TALIF evaluation. Fluorescence decay times above 16 ns at 10 Pa enforce this such that a stronger overestimation of n_D by TALIF due to this is expected compared to the H_2 plasma.

Electron density and temperature

In order to assess the increase of the atomic density in the D_2 plasma compared to the H_2 plasma, n_e and T_e are evaluated. These two parameters are shown in figure 5.23 together with the respective results of the campaigns with the H_2

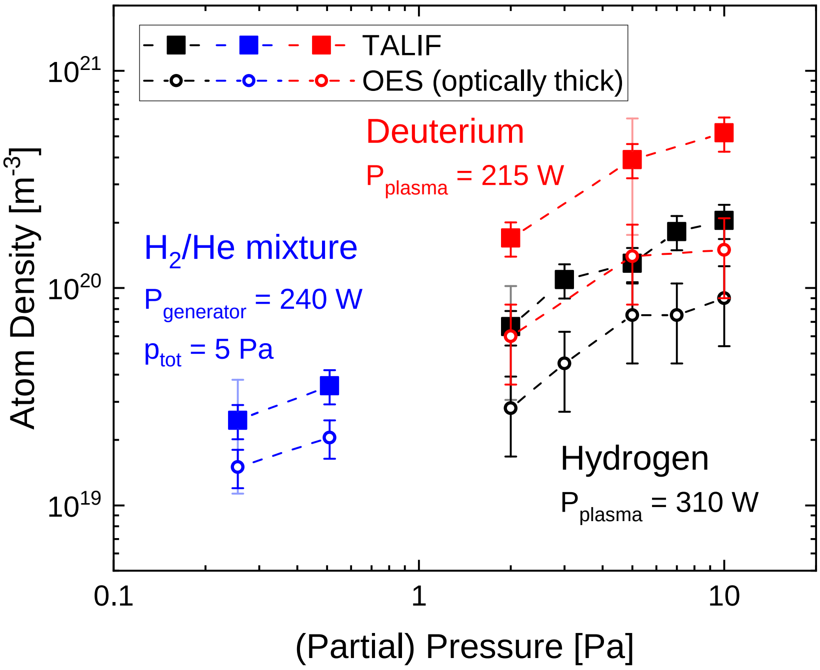

Figure 5.22: *D atom density measured via TALIF and OES (optically thick case) for the D_2 plasma campaign. The campaigns with H_2 and the H_2/He mixture are shown for comparison.*

plasma and the H_2/He mixture plasma. This reveals n_e values between $1 \times 10^{16}\,\mathrm{m}^{-3}$ and $4 \times 10^{16}\,\mathrm{m}^{-3}$ which are lower compared to the conducted H_2 campaign which is due to the lower value of power coupled to the plasma in this case. T_e is, however, elevated by 5 – 15 % in the D_2 plasmas compared to the H_2 plasmas.

Comparison of n_D with n_H

An increase in T_e causes stronger dissociation with a steep dependence. However, the observed T_e difference is so small that this is not expected to be the sole reason for the higher atomic density in the D_2 plasmas compared to H_2. On top, n_e is smaller in the investigated D_2 plasmas which causes less dissociative collisions between electrons and D_2 molecules.

The cross section of electron impact dissociation is calculated in [SFK+21] for H_2 and D_2. Here, it is shown that the slight isotope dependence of the cross sections in combination with the altered vibrational structure of the molecules could cause an increase of the electron impact dissociation rate by 10 %. This calculation is performed under the assumption of thermal equilibrium for the population of the vibrationally excited molecule states. However, the order of magnitude of this effect is small compared to the found increase of a factor of 2.5.

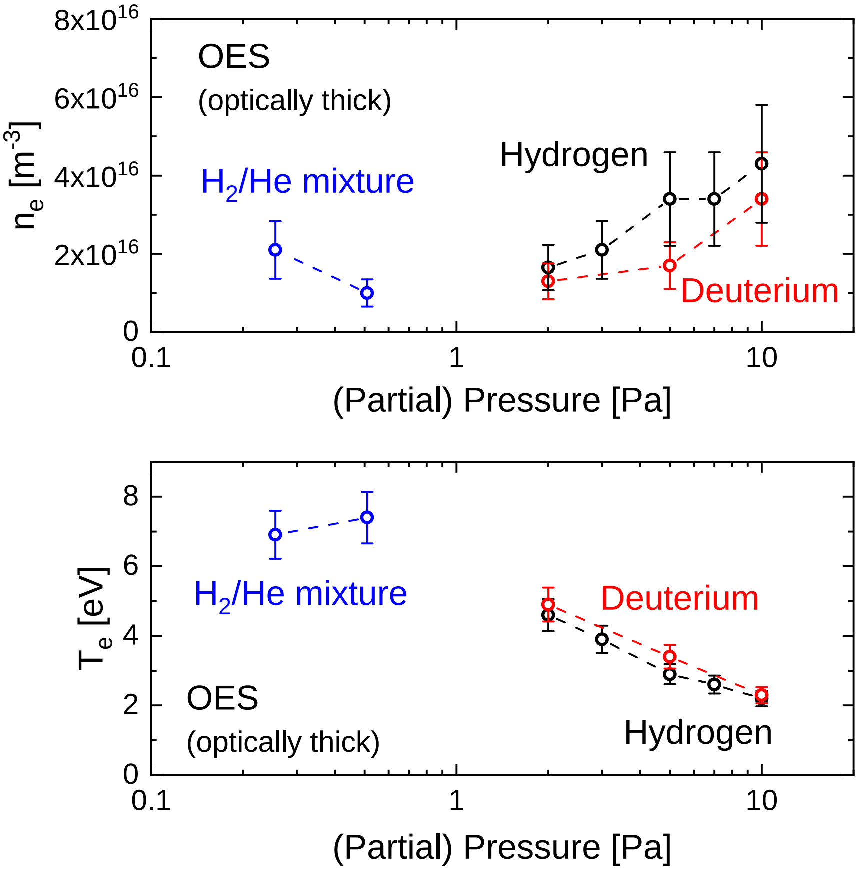

Figure 5.23: *Electron density and temperature as determined with OES (optically thick case) for the D_2 plasmas. For comparison, the corresponding results of the campaigns with H_2 and H_2/He plasmas are shown.*

The loss rate of atomic deuterium at the walls of the plasma vessel is dominated by the diffusion of atoms rather than the wall recombination process for the investigated pressure range. As was already elaborated in chapter 2.3.1, its mass dependence causes a decrease of 30 % of the diffusion coefficient. Inserting this into equation (2.22) yields that the D atom loss rate K_{loss} drops by 30 % compared to atomic hydrogen. This causes in turn a higher density of atomic deuterium in the plasma but can not explain the factor of 2.5 which is observed such that a further effect has to play a role which could not be resolved in these investigations.

Atomic and molecular deuterium temperature

The temperature of deuterium atoms and molecules is depicted in figure 5.24 together with the results of the previous campaigns conducted with H_2. The temperature value of deuterium atoms is between 530 K and 610 K and thus slightly

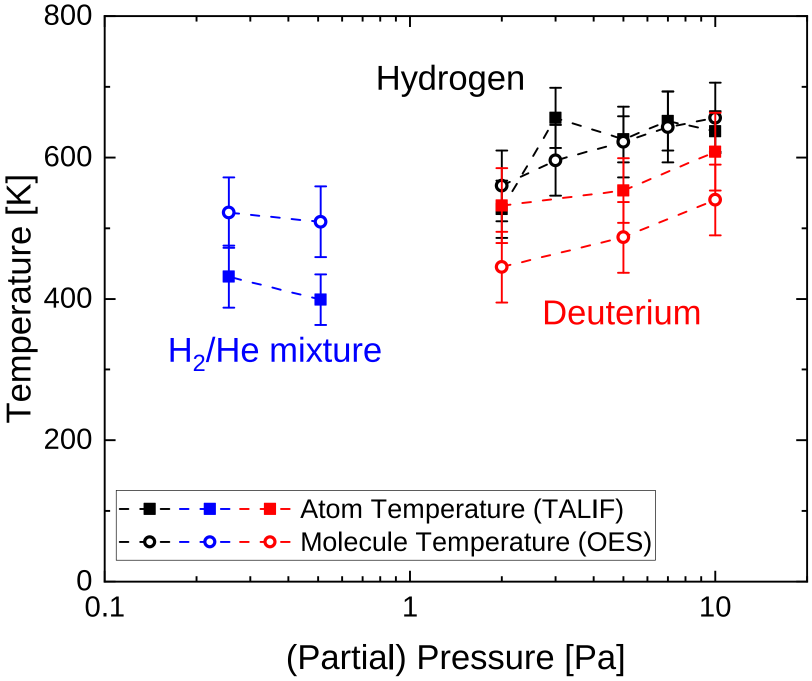

Figure 5.24: *D atom temperature (determined by means of TALIF) and D_2 temperature (determined by means of OES) for the conducted D_2 plasmas. The results of the preceding campaigns using H_2 are depicted for comparison.*

lower than the range that was observed in the H_2 plasma. The D_2 molecular temperature is lower and is between 450 K and 550 K. Both temperatures rise for increasing pressure which can again be attributed to the increased number of collisions between electrons and neutral particles. The difference of atomic and molecular temperature could be explained qualitatively due to the Franck-Condon energy that is released during D_2 dissociation as outlined in chapter 5.4. The observed difference between atomic and molecular temperature hints towards an insufficient thermalisation of the two species. In order to confirm this, measurements at higher pressure are necessary which are expected to show equality of the two temperatures. This is, however, out of scope for the present experimental setup. Nevertheless, the two temperatures are close to each other, such that a common temperature again is a reasonable approximation.

5.6 Conclusions for the application of TALIF to BATMAN Upgrade

The TALIF setup was successfully comissioned and reproducible measurements were possible. For the application of TALIF to BATMAN Upgrade, the following experience was gained:

- The fluorescence collection optics could be calibrated regarding their transmission and the calibration can be directly transferred to BUG.
- The influence of the emission line width of the laser can be compared to a Gaussian line profile with $\Delta\lambda_{\mathrm{Laser}} = (1 \pm 0.1)\,\mathrm{pm}$. With this, the VDF of hydrogen and deuterium atoms in BUG can be determined.
- The H fluorescence decay time is found to depend on the density of H atoms. At the low density values which are expected at BUG, a decay time close to 10 ns is expected which is connected to a branching ratio of $a_{\mathrm{H}_\alpha} = 0.441$.
- TALIF signals can be measured despite a TALIF-to-background ratio of 0.2 by increasing the number of laser pulses considered for one acquisition. However, this comes with an increased length of the acquisition time. In BUG, plasmas can presently be operated only up to 100 s which puts a hard limit to the acquisition time.
- The lowest measured hydrogen density is $2.5 \times 10^{19}\,\mathrm{m}^{-3}$ which is still higher than the densities expected at BUG. Due to the variable gain of the PMT, also lower densities can be assessed by the TALIF system as long as the H_α background can be suppressed sufficiently.
- The acquisition time of one TALIF line profile with the built system is on the order of 5 minutes or longer which is larger than the length of a plasma pulse at BATMAN Upgrade. A single line profile can therefore not be recorded within a single plasma pulse.

6 TALIF at BATMAN Upgrade

6.1 The BATMAN Upgrade test facility

BATMAN (**Ba**varian **T**est **Ma**chine for **N**egative Ions) Upgrade (short: BUG) is a test facility for the investigation of the generation and extraction/acceleration of negative hydrogen ions. It is equipped with a negative ion source which is 1/8 the size of the source which is planned for ITER. The predecessor teststand BATMAN is in operation since 1997 [KSB+18] and could demonstrate the requirements of ITER for a negative ion source for NBI concerning the extracted negative ion current density and the ratio of co-extracted electrons and negative ions for a pressure of 0.3 Pa [HFK+17].

6.1.1 Experimental apparatus

BATMAN Upgrade consists of the RF prototype negative hydrogen ion source, an extraction and acceleration system and a vacuum vessel behind the source (called *tank*) in which the accelerated ion beam is dumped and investigated. Figure 6.1 shows a CAD drawing of the ion source. It is equipped with a cylindrical driver which has a diameter of 24 cm and a length of 17 cm. A coil with six windings is wound around the driver and acts as RF antenna. Cooling water flows through the coil in order to cool the heat induced by ohmic losses within the coil. The plasma is driven by an RF generator which is connected to the coil via a matching network. A maximum power of 100 kW is applied at 1 MHz. The driver consists of a quartz ceramic cylinder and a Faraday shield is attached to the inner side of the driver walls. This shield suppresses capacitive coupling which would cause a high potential difference between the plasma and the vessel walls. This would cause a damage to the walls due to accelerated positive ions and protects the quartz cylinder from direct plasma contact. This is of particular importance as any sputtered impurities heavily affect the Cs conditioning causing temporal instabilities in the extracted negative ion current.

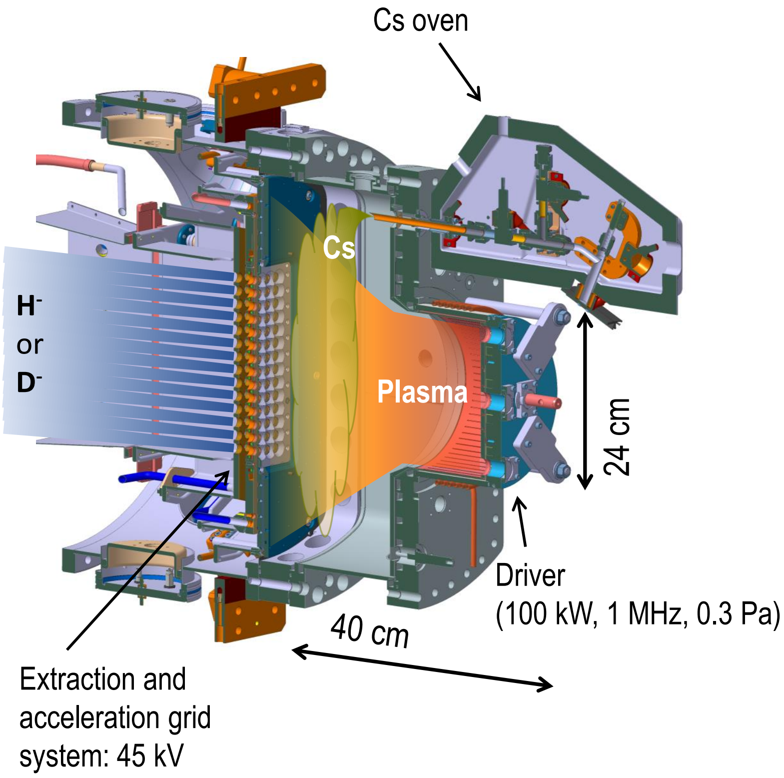

Figure 6.1: *Vertical cut through BATMAN Upgrade ion source with the exctraction and acceleration system. CAD created by Markus Fröschle.*

Above the driver, a Cs oven is attached to the ion source which evaporates Cs into the expansion region towards the PG by heating a liquid Cs reservoir and thus controlling the Cs vapour pressure. The Cs is redistributed within the chamber by the plasma. The expansion region is roughly cuboid and has dimensions of w × h × l = 31 × 58 × 23 cm^3. The filter field in the expansion region is generated by a current of up to 3 kA flowing vertically through the PG and two return conductors outside at the driver side of the expansion vessel. The latter lowers the magnetic field inside the driver to allow operation in low pressure. Converting the current into a magnetic field strength, 1 kA corresponds to roughly 2 mT (horizontally oriented) in the center of the vessel in a distance of 2 cm to the plasma grid. In [Mar20], a plasma asymmetry is observed which arises from a drift of both positive ions and electrons which is caused by the magnetic filter field. Due to this drift, the density of charged particles is generally higher in the top half of the ion source which als reflects in the spatial extracted negative ion profile.

The extraction and acceleration system was upgraded in 2016 and is oriented at the grid system as planned for ITER regarding shape and arrangement. It represents almost one beamlet group of the ITER source [FBF+19] and is depicted in figure 6.2. The left part of the figure depicts the plasma grid which is partly covered by the bias plate. The distance between the two parts is 4 mm. The right part shows the arrangement of the PG, the EG and the GG whereas the three grids are used for the extraction and acceleration of the negative ions. The negative ions are extracted from the plasma via a voltage between the PG and the EG of up to 10 kV. This happens through apertures in the grid system which have a diameter of 14 mm. The total available acceleration voltage is 45 kV. Here, the tank and the GG are kept at ground potential whereas the source is operated at the negative high voltage potential. Permanent magnets are embedded in the EG in order to deflect co-extracted electrons onto the EG which is actively cooled in order to prevent melting due to the high power load. Both BP and PG are electrically insulated from the source walls and can be biased positively with respect to them. In the latter case, this acts for suppressing the co-extracted electrons [WF16a]. In the standard configuration which was also present in this work, the BP is connected to the outer source walls via a 1 Ω resistor thus having a potential between the source walls and the floating potential. The PG and BP can be heated to a temperature between 150 °C and 250 °C in order to control the Cs dynamics whereas the source walls are kept at 35 °C which prevents the development of cold spots which lead to an accumulation of Cs at these spots.

The negative ion beam is accelerated into a large tank (length: 2 m, base area: 1 m^2) in which diagnostics on the beam can be performed. The teststand is pumped predominantly with a cryo pump which is attached to the tank. Two additional pump stands are attached to the teststand in order to lower the pressure sufficiently such that the cryo pump can work. Each consists of a backing pump in combination with a turbomolecular pump. With this pump system, a background pressure of 3×10^{-7} mbar is reached. Hydrogen or other gases like krypton for TALIF calibration can be fed into the experiment via a connection in the backplate of the driver.

6.1.2 BATMAN Upgrade operation

A typical pulse of BATMAN Upgrade is illustrated in figure 6.3 which shows time traces of the source pressure (p_{source}), extracted ion current (I_{ion}), RF power

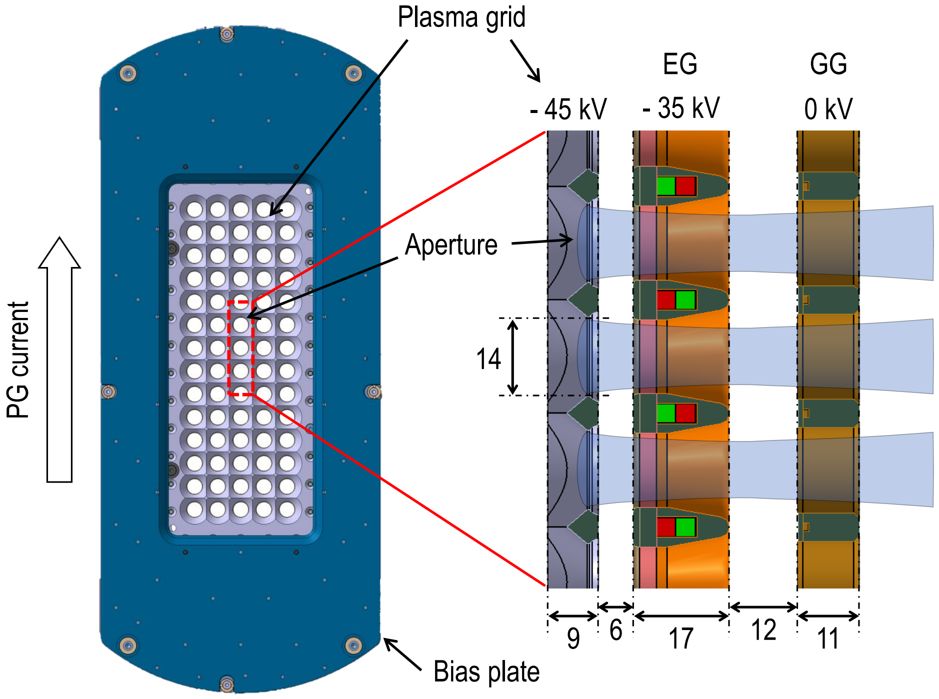

Figure 6.2: *CAD drawing of the plasma grid and bias plate as seen from the driver (left) and cross section through the grid system (right). EG: extraction grid, GG: grounded grid. Picture after [KSB⁺18], dimensions in mm. CAD created by Markus Fröschle.*

(P_{RF}), applied high voltage (U_{HV}) and the H_α emission which was measured by a photodiode that is observing the driver plasma.

A pulse starts by a gas puff which releases H_2/D_2 gas into the source. Still at high pressure, 20 kW of RF power are applied for ignition. Subsequently, the pressure is reduced and the RF power is increased such that both parameters are at the desired value which are 0.3 Pa and 70 kW in this example. The time period in which RF power is supplied to BUG is denoted as *RF phase*. The H_α signal shows the ignition process as a strong increase of the radiation. After a specified time period which is sufficient for the plasma to stabilize (i. e. the H_α emission becomes widely stable), the extraction and acceleration of negative ions is started. For this, U_{HV} is set to the desired value, entering the *high voltage phase*. After a pre-set time, the extraction and acceleration voltages are set to 0 again stopping the ion extraction. The RF phase is prolonged for a short while longer and eventually terminates when the pulse is finished. In the current state of the experiment, the pulse length is limited by the heat-up of the plasma grid and the bias plate during the RF phase to a maximum RF phase length of 100 s at, however, reduced RF power.

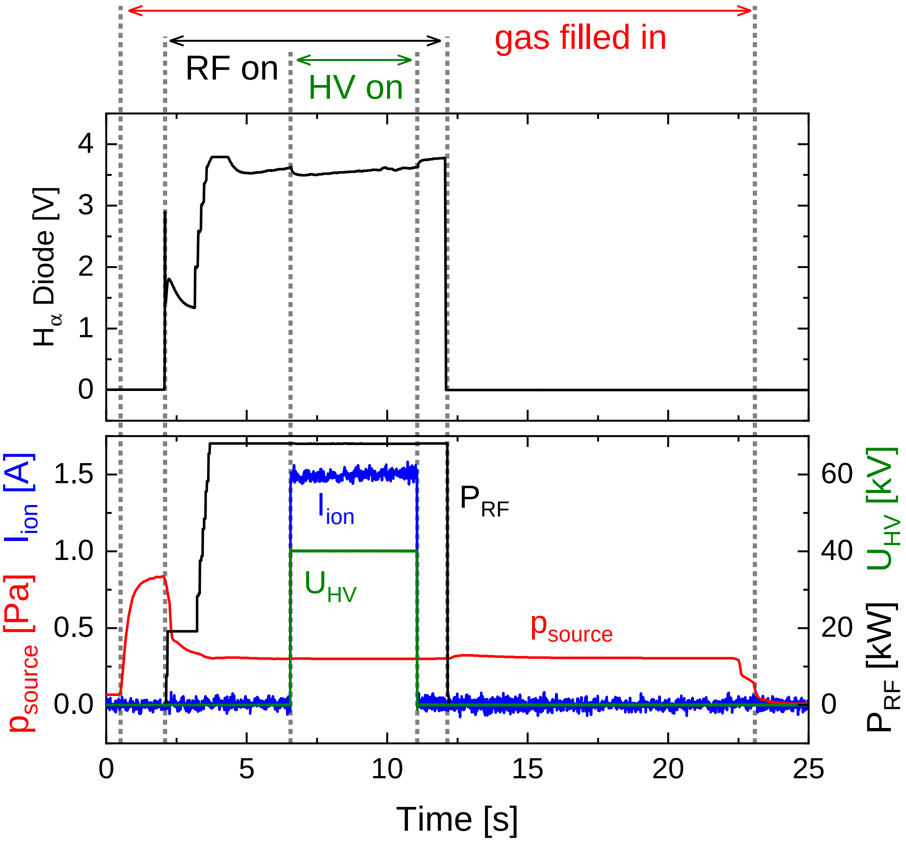

Figure 6.3: *Time traces of the H_α emission, the source pressure (p_{source}), extracted ion current (I_{ion}), RF power (P_{RF}) and applied high voltage (U_{HV}).*

The presence of Cs in the plasma can have an effect an the plasma parameters in H_2 plasmas which is investigated in [Fri13]. Among these, especially the effect of Cs on the H atom density is of relevance. Here, a decrease of the H atom density by up to 50 % is observed at sufficient Cs density. For deuterium, this effect is less pronounced. This is explained by the effect of H atom gettering of Cs at the walls of the plasma vessel. In negative hydrogen ion sources, this effect is known as *over-conditioning* and causes a decrease of the current of extracted negative ions [FBH+21] due to the excessive gettering of H atoms at the source walls. Over-conditioning is accompanied by a decrease of the H_α emission such that this emission is recorded with a survey spectrometer (*Plasus:* SA Series) in order to avoid this state.

6.1.3 OES at BATMAN Upgrade

OES is performed at BATMAN Upgrade regularly in order to determine plasma parameters n_e, T_e and n_H in different regions of the ion source of BATMAN

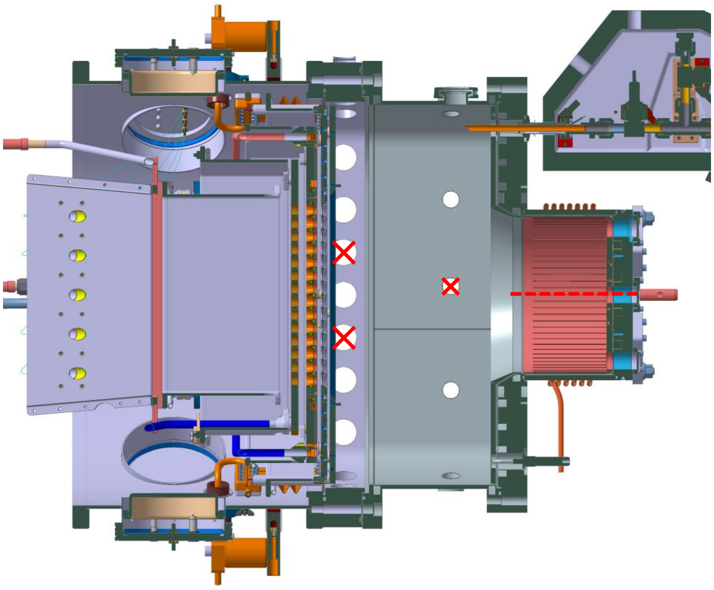

Figure 6.4: *Lines of sight for the OES employed at BATMAN Upgrade. CAD created by Markus Fröschle.*

Upgrade. For this, a high resolution spectrometer (*Princeton Instruments:* Acton SpectraPro SP-2750) is connected to four lines of sight (LOS) at the ion source. They are depicted in figure 6.4. Two LOS are employed close to the plasma grid while the expansion region and the driver are monitored with one LOS respectively. The light is collected with lens heads and optical fibre which are connected to the spectrometer.

With this setup, the Balmer lines α to δ are investigated for atomic hydrogen and the Q branches of the first four diagonal vibrational transitions of the Fulcher-α band are observed for molecular hydrogen. The obtained results are used in order to determine n_e, T_e and n_H via a comparison to the CR models Yacora H and H_2. Again, the application of the CR model has been carried out by [Bri22]. For the evaluation of the spectra at BATMAN Upgrade, only optically thin Yacora H and H_2 calculations have been used. For the BATMAN Upgrade geometry, no population escape factors have been calculated yet. This is because of the complex geometry and spatial emission profile as also emission originating in the driver reaches the positions in the expansion region and close to the PG. These points make the calculation of population escape factors computationally very expensive. The resulting n_H values are therefore likely to overestimate the true density value present in the plasma as outlined in chapter 5.3.

6.2 TALIF connection and implementation

The laser is located roughly 12 m away from the ion source of BATMAN Upgrade on a different level of the building due to the considerations outlined in chapter 4. This distance needs to be overcome by the laser beam while maintaining the stability of the laser position within BUG. For this, a laser beamline was constructed using guiding mirrors.

The full laser beamline can be seen in figure 6.5. Here, the laser beam is guided from the laser enclosure to BUG by using four mirrors in total. In the course of this, the beamline is completely enclosed by PVC tubing which was prior tested for laser safety. This tubing serves on the one side as laser enclosure which ensures a safe working environment and is on the other side used for fixing the beamline to the ceiling and the ground of the operation hall in order to minimize vibrations. The mirrors are held within PVC cross pieces. A close view of the first mirror after exiting the laser enclosure is depicted in figure 6.6. The mirror is mounted within a standard *Thorlabs* mirror mount which is attached to a 3D printed mount holder. The latter is used for a coarse alignment of the mirror. O-rings are used in order to seal the space between the mount holder and the PVC cross piece. Fine alignment of the mirror can be achieved by using the alignment screws on the left side of the mirror mount. The cross piece can be closed after alignment with a 3D printed plug which is sealed with O rings.

The beam is guided into the ion source from below and focussed into the vertical center by using a UV fused silica lens with a specified focal length of 750 mm. As negative hydrogen ions are produced on the plasma grid, the n_{H} measurement is desired close to the PG. The position of the laser beam above the PG can be seen in figure 6.7. For entering the vacuum vessel, one of the vertical access flanges is used. This leads to a distance of 25 mm between laser beam and PG. The fluorescence is collected perpendicular to the laser beam at a horizontal port which is located at half the height of the chamber which is between the two LOS which are use for OES. The resulting n_{H} values are considered to be comparable despite the vertical asymmetry of the plasma in front of the PG. This is because the H atoms are predominantly produced in the driver and diffuse subsequently into the expansion chamber towards the PG without being affected by the plasma drift as they are neutral particles. An asymmetry n_{H} could arise from collisions of H atoms with ions which are affected by the drift or the predominant wall recombination of positive ions in the upper half of the chamber. However, since this asymmetry is not a direct consequence of the plasma drift, it is smaller compared to the electron

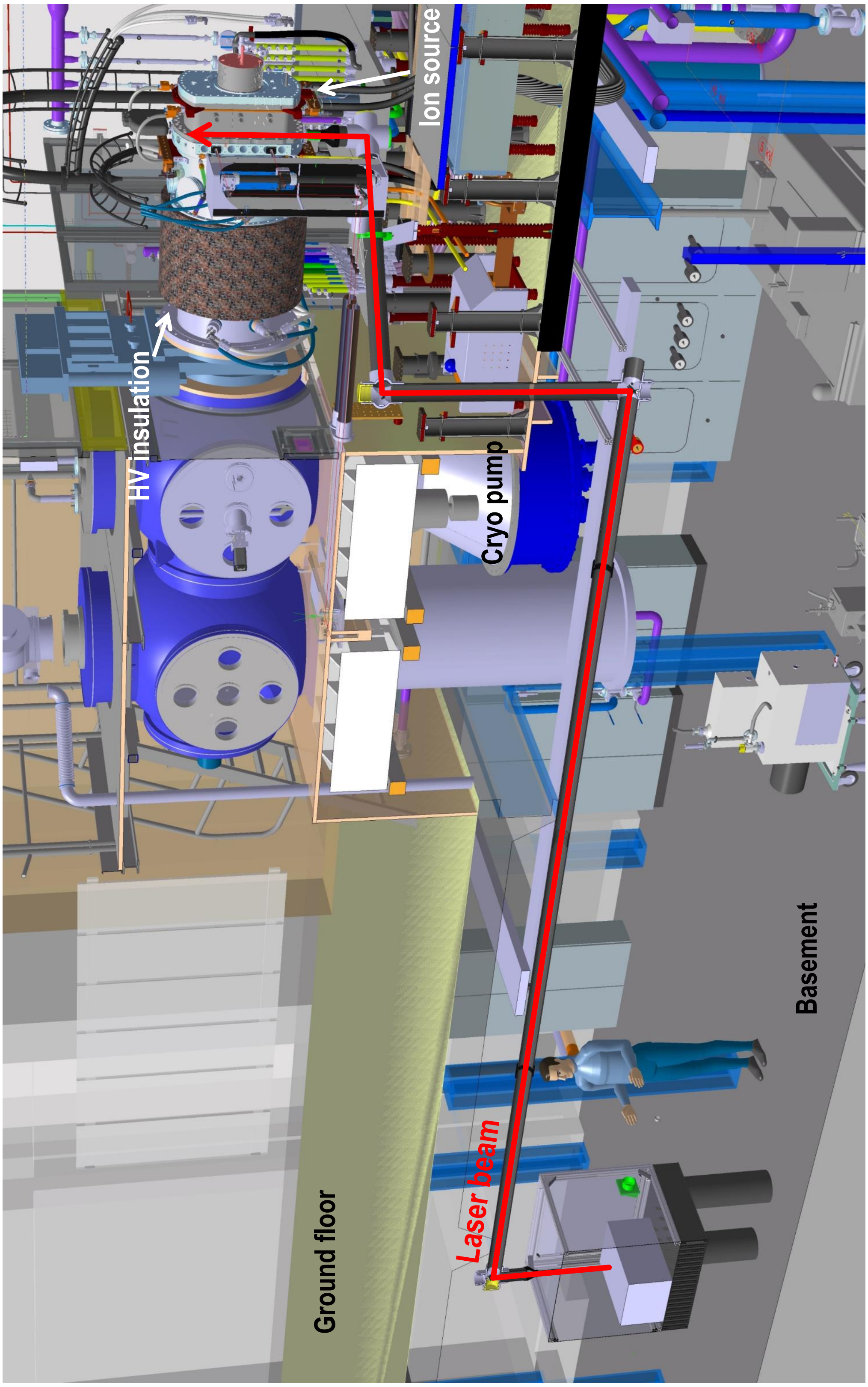

Figure 6.5: *Path of the laser beam within the BATMAN Upgrade operation hall guided from the laser enclosure to the ion source. Human for scale. CAD created by Andreas Oberpriller.*

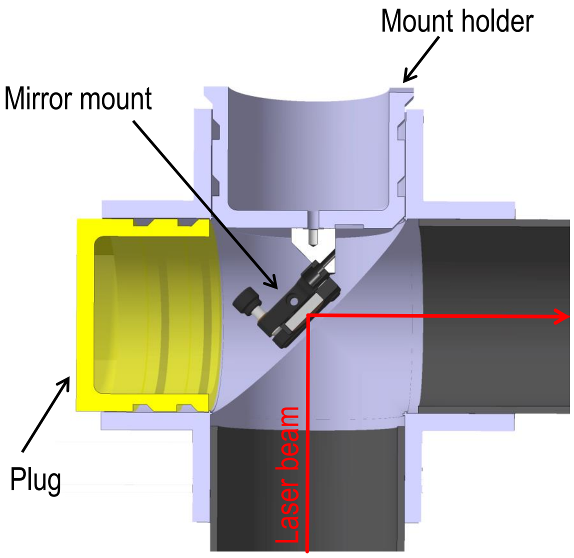

Figure 6.6: *Close view to one of the PVC crosses which are used for holding the laser mirrors. CAD created by Andreas Oberpriller.*

and ion density. Further, the n_H values as obtained from the two LOS of the OES can be compared in order to assess the asymmetry.

The fluorescence light is collected by using an achromatic lens (focal length: 85 mm) which focusses the fluorescence light onto a fibre with a diameter of 1 mm. A 3D printed aperture with a slit width of 3 mm is used for spatial filtering the plasma radiation. For this, the slit is aligned in parallel to the laser beam which causes the observed volume to be vertically elongated to roughly 25 mm. This apparatus is attached to the ion source at a horizontal port. Spectral filtering is performed with two filters at 830 nm ± 10 nm (*Thorlabs:* FL830-10) for Kr measurements and 650 nm ± 40 nm (*Thorlabs:* FB650-40) for H measurements which are installed between the aperture and the achromatic lens. The fibre is connected to the PMT (*Hamamatsu:* H11706-20). After crossing the vacuum vessel, the laser is dumped in a beam dump.

In the laser enclosure, the optics are arranged similar to the arrangement which is introduced in chapter 4.2. The changes to the system are depicted in figure 6.8. A telescope system made of two focussing lenses (focal length: 200 mm) is inserted into the optical system. This is due to alter the divergence of the laser beam such that the beam is fairly collimated. Otherwise, the laser beam size exceeds the mirror size before reaching the ion source which causes losses of laser energy. Resulting from this, the laser beam diameter close to the ion source can be adjusted

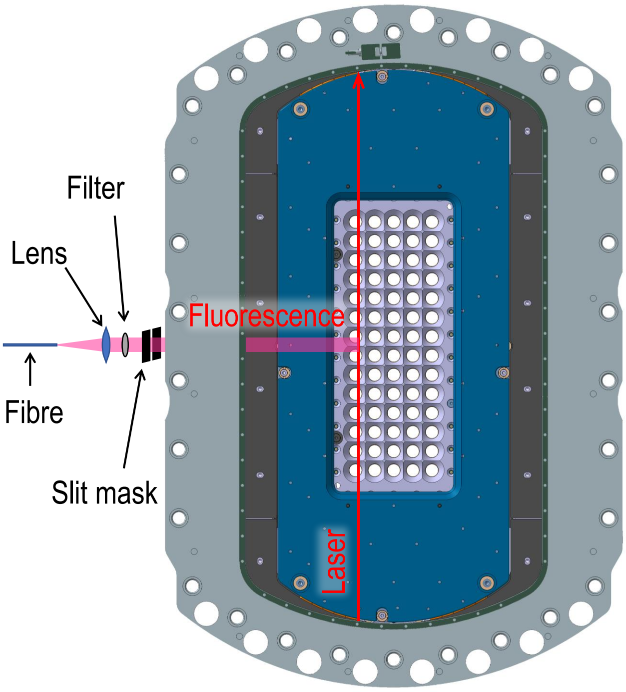

Figure 6.7: *Laser beam path in front of the plasma grid and arrangement of the optics for collection of the fluorescence light. CAD created by Markus Fröschle.*

to roughly 1 cm. Again, the variable attenuator is used in order to control the energy per laser pulse and the laser intensity is monitored by the photodiode.

The resulting energy per laser pulse at BATMAN Upgrade has a maximum value of 200 µJ which corresponds to 30 % of the energy leaving the laser system. The losses consist of multiple contributions:

- the maximum transmission of 72 % of the variable attenuator
- the reflectivity of 97 % of the mirrors (in total seven mirrors correspond to a total laser beamline transmission of 81 %)
- the beam splitter in front of the photodiode with a total transmission of ~ 90 %
- reflections at the uncoated surfaces of the telescope lenses, the focussing lens and the window used for entering the ion source
- scattering losses in air which were observed visibly
- absorption of UV radiation in moisture in the air [Ste21]

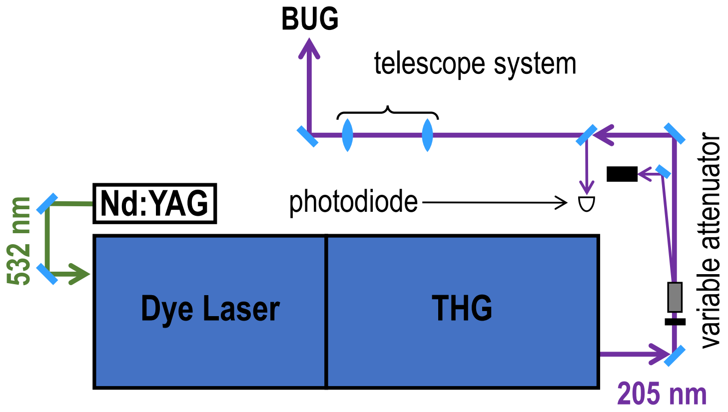

Figure 6.8: *Optical arrangement of the laser system and the additional optics for the connection of the laser beam to BATMAN Upgrade.*

The laser beam position was observed to be very stable within the ion source such that re-alignment of the optics has to be carried out only on a weekly basis and the system is considered to be stable within one day.

6.3 Characterization of the TALIF system

6.3.1 Acquisition procedure and resulting signals

The TALIF-to-background ratio for the measurements during plasma operation was observed to be below 0.1 for the shown arrangement of the fluorescence optics despite the spatial filtering with the slit mask. Without slit mask, no signal could be observed against the background radiation. In order to resolve the signal against the noise of the background, 4000 laser pulses are necessary for one TALIF signal acquisition. Figure 6.9 shows the result of such a measurement. Here, the timely resolved PMT signal is depicted after subtraction of the H_α background. The laser wavelength is set to a value in the center of the transition. This figure marks the first time that TALIF was applied to a negative hydrogen ion source.

The resulting signal to noise ratio is 4 which is lower than observed for the measurements at ALFRED. The source of the increased noise level could be due to two reasons. Firstly, the ratio of signal to the H_α background is lower such that the noise of the background radiation is more relevant in relation to the fluorescence signal. Secondly, the RF noise for the measurements at BATMAN Upgrade was observed to be higher compared to ALFRED, which is mainly due to the higher RF power in the former case. The first problem could be tackled by

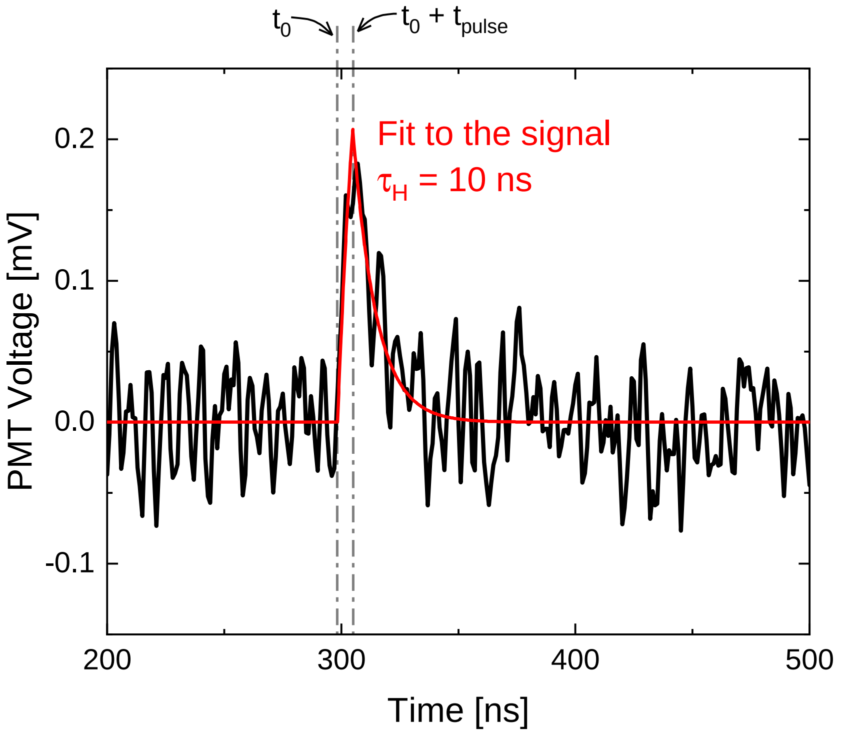

Figure 6.9: *Exemplary PMT signal $U_{PMT}(t)$ obtained at BUG.*

increasing the fluorescence signal in relation to the background radiation. Better shielding of the PMT and the oscilloscope against RF coupling could improve the RF noise.

The increased noise level puts difficulties to the further data processing. Especially in the wings of the line profile at low signal strength, numerical integration of the PMT signal is considered unreliable. Noise filtering techniques such as Fourier analysis or Savitzky-Golay filtering are not possible with the acquired waveforms due to the lack of temporal resolution which is only 1 ns for the used oscilloscope. Therefore, the signals are evaluated by fitting an expected fluorescence signal to the obtained PMT data. This function is obtained as the solution of equation (3.4) for a laser beam with a rectangular temporal intensity profile while assuming a constant density of the ground state. The PMT signal is proportional to $n_2(t)$ such that it is given by

$$U_{\mathrm{PMT}}(t) = \begin{cases} 0 & , t < t_0 \\ C \cdot \left[1 - \exp\left(-\frac{t-t_0}{\tau_{\mathrm{H}}}\right)\right] & , t_0 \leq t < t_0 + t_{\mathrm{pulse}} \\ C \cdot \left[1 - \exp\left(-\frac{t_{\mathrm{pulse}}}{\tau_{\mathrm{H}}}\right)\right] \cdot \exp\left(-\frac{t-(t_0+t_{\mathrm{pulse}})}{\tau_{\mathrm{H}}}\right) & , t \geq t_0 + t_{\mathrm{pulse}} \,. \end{cases} \tag{6.1}$$

Here, C is a proportionality constant which is used as fitting parameter, t_0 is the starting time of the laser pulse and t_{pulse} is the pulse length. τ_{H} is the fluorescence decay time of the signal. Before the laser pulse ($t < t_0$), no excitation of ground state atoms takes place resulting in the value 0 of the PMT voltage. During the pulse ($t_0 \leq t < t_0 + t_{\mathrm{pulse}}$) the fluorescence follows a restrained growth function resulting from the balance of two-photon excitation and spontaneous emission. After the laser pulse ($t \geq t_0 + t_{\mathrm{pulse}}$), the fluorescence follows an exponential decay function.

This fitting function was tested on PMT signals obtained at ALFRED with a very good signal to noise ratio. The resulting integrated signals agree with the numerically integrated values within 3 % such that this method is considered as reliable. A small overestimation of the fluorescence strength is present due to the assumed temporal intensity profile of the laser which differs from the experimentally observed one that is shown in figure 5.4. For the evaluation of signals as obtained at BUG, the two parameters t_{pulse} and τ_{H} are chosen as fixed values. t_{pulse} is obtained from a fit of the function to data obtained at ALFRED and has the value $t_{\mathrm{pulse}} = 6.5\,\mathrm{ns}$. Following the line of argument of chapter 5.6, $\tau_{\mathrm{H}} = 10\,\mathrm{ns}$ is expected. This leaves C and t_0 as open parameters that can be optimized in the fitting routine. The result of this procedure is shown in figure 6.9 in red. This fit describes the obtained signal reasonably well. Integration of the fit result gives the value of $\int U_{\mathrm{PMT}}(t)\,\mathrm{d}t$. The uncertainty of this procedure is assessed via the standard variation of C which is another result of the fitting procedure, such that $\frac{\Delta C}{C}$ is added to the random error bar.

The acquisition of a single data point requires a total time of 80 s which is close to the maximum plasma pulse length possible at BATMAN Upgrade. Therefore, a line profile is obtained by performing TALIF measurements at subsequent plasma pulses with the maximum length of 100 s while changing the laser wavelength between two pulses. The presence of Cs in the ion source and its redistribution during the plasma pulse cause a temporal instability during such long pulses which manifests itself in a temporal variation of the emission of a Cs emission line at 852 nm and the current of co-extracted electrons [WWR+21]. In order to guarantee stable conditions during the TALIF measurements, Cs is not fed into BUG during the conducted measurement campaign. Due to the high amount of co-extracted electrons otherwise, no ion beam is extracted during the measurement campaign at BUG. In order to put the measured H and D atom densities into context of the extracted ion currents, the latter need to be determined for BUG pulses at equal source parameters while the source is cesiated and negative ions are extracted.

In order to compare the TALIF results to OES measurements or the extracted ion current obtained at the teststand with a cesiated ion source, the state of over-conditioning has to be avoided. This is ensured by comparing the survey spectrometer results on the H_α of the two BUG shots that are to be compared.

6.3.2 Saturation correction of the TALIF signals

In order to obtain a sufficient fluorescence strength such that the TALIF signal is distinguishable against the H_α background, a laser energy of at least 120 µJ per pulse is necessary which was also used for the data in figure 6.9. This energy is in the saturated regime such that the resulting H and D atom densities as determined via TALIF would be underestimated. The saturation of the TALIF signal can be assessed with a method introduced in [MRD+16]. Here the fluorescence signal F is described by

$$F = \frac{\alpha\, E_\mathrm{L}^2}{1 + \beta\, E_\mathrm{L}^2}\,. \tag{6.2}$$

E_L is the used energy per laser pulse in [MRD+16]. α corresponds to the proportionality constant between integrated PMT signal and the squared laser intensity. For a given atomic species, it depends on the transmission properties of the fluorescence collection system, its observed volume and the efficiency of the PMT. β describes the strength of the saturation and it depends solely on the atomic species which is probed with the laser. In the TALIF diagnostic applied in this work, E_L^2 translates to $\int [U_\mathrm{PD}(t)]^2\,\mathrm{d}t$ while F translates to $\int U_\mathrm{PMT}(t)\,\mathrm{d}t$. A saturated TALIF signal $S_\mathrm{TALIF}^\mathrm{H}$ can be corrected by multiplying it with the factor $(1 + \beta \int [U_\mathrm{PD}(t)]^2\,\mathrm{d}t)$.

In [MRD+16], the values of β for Kr and H atoms are determined by performing a scan of the energy per laser pulse and fitting equation (6.2) to the $F(E_\mathrm{L})$ data. For the TALIF at BATMAN Upgrade, this is not possible since the quadratic regime could not be reached due to the high H_α background. This would lead to a high uncertainty for the determined β values. Instead, a scan of the energy per laser pulse is performed for Kr with the TALIF system installed at BUG and equation (6.2) is fitted to the resulting data giving $\beta_\mathrm{BUG}(\mathrm{Kr})$. The same is done with the energy scans performed at ALFRED with Kr, H and D atoms giving

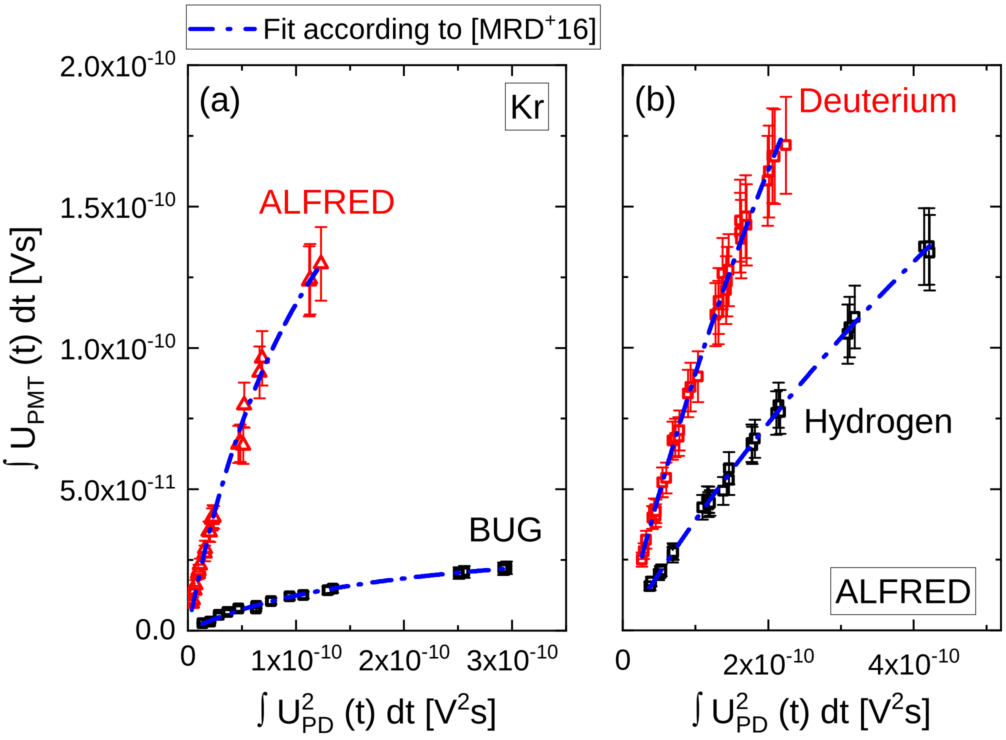

Figure 6.10: *Integrated PMT voltage as a function of* $\int [U_{PD}(t)]^2\,dt$ *and fit of equation* (6.2)*. (a) Results for TALIF on Kr atoms at ALFRED and BUG. (b) Results for TALIF on D and H atoms at ALFRED.*

$\beta_{\mathrm{ALFRED}}(\mathrm{Kr})$, $\beta_{\mathrm{ALFRED}}(\mathrm{H})$ and $\beta_{\mathrm{ALFRED}}(\mathrm{D})$. $\beta_{\mathrm{BUG}}(\mathrm{H/D})$ is then calculated by scaling the β values via

$$\beta_{\mathrm{BUG}}(\mathrm{H/D}) = \frac{\beta_{\mathrm{ALFRED}}(\mathrm{H/D})}{\beta_{\mathrm{ALFRED}}(\mathrm{Kr})} \cdot \beta_{\mathrm{BUG}}(\mathrm{Kr})\,. \tag{6.3}$$

For this scaling it is assumed that the saturation occurs at the same laser intensity in both experiments. It is necessary due to the differing conversion factors between laser intensity at the experiment and the voltage measured by the photodiode. The described fits are performed in figure 6.10 (a) and (b). In (a) the two energy scans performed with Kr atoms both at BUG and ALFRED are shown while in (b) the energy scans on H and D atoms at ALFRED are depicted. Each graph contains the fit of equation (6.2) to the data points.

In general, the fits work very well for all four energy scans. With this the two β factors for H and D atoms are determined to be

$$\beta_{\mathrm{BUG}}(\mathrm{H}) = 4.9 \times 10^{8}\,(\mathrm{V}^2\mathrm{s})^{-1} \quad \text{and} \quad \beta_{\mathrm{BUG}}(\mathrm{D}) = 9.3 \times 10^{8}\,(\mathrm{V}^2\mathrm{s})^{-1}\,.$$

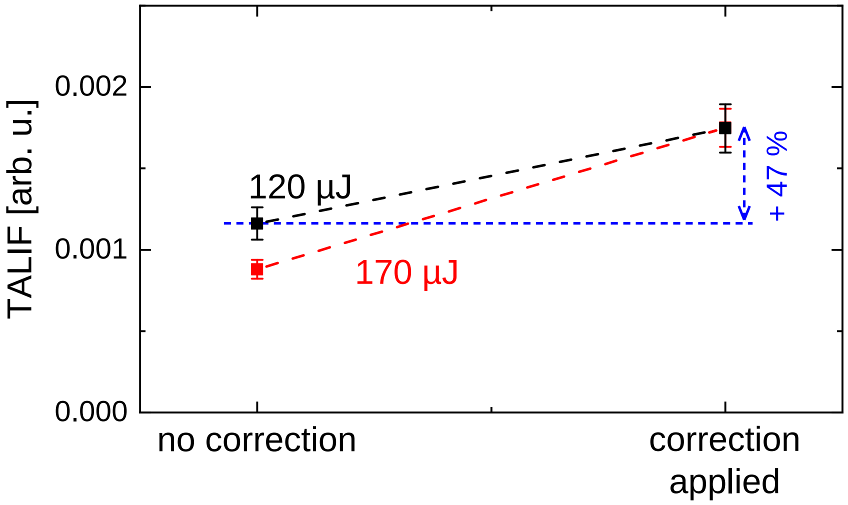

Figure 6.11: *Two TALIF signals S^{H}_{TALIF} observed at BUG for equal ion source parameters but for differing values of the laser energy per pulse of 120 µJ and 170 µJ. The saturation correction after [MRD+16] is applied to the right data points while the left data points are uncorrected.*

At the energy per laser pulse of 120 µJ, this corresponds to a correction factor of 1.5 in the case of H atoms and 1.9 in the case of D atoms. This is in the same range as the corrections applied in [MRD+16] which implies that the correction procedure is valid in general. The difference between the two correction factors for H and D atoms is due to the observed difference of the quadratic regimes as discussed in chapter 5.5. A benchmark of the saturation correction procedure is depicted in figure 6.11 which shows two exemplary TALIF signals $S^{\mathrm{H}}_{\mathrm{TALIF}}$ which were recorded for two BUG pulses with an H_2 plasma at the same source parameters but with the two differing laser pulse energy values of 120 µJ and 170 µJ. On the left side, no correction is applied to the two measurements reflecting in a differing result of the measurement. The data point obtained for 170 µJ is below the data point obtained for 120 µJ confirming the saturation regime. When the correction is applied to both data points considering their respective values of $\int [U_{\mathrm{PD}}(t)]^2 \, \mathrm{d}t$, excellent agreement of the data is observed. The correction procedure is therefore considered reliable within the considered range of energy per laser pulse.

With this procedure, a quantitative evaluation of the TALIF signals is possible despite the low signal to background ratio by operating at elevated laser energies in the saturated regime. The uncertainty of the β values for H and D atoms is determined from the uncertainties obtained by the fitting of the respective energy scans and summing them up with Gaussian error propagation. They are considered as systematic errors and are added to the uncertainty that is outlined

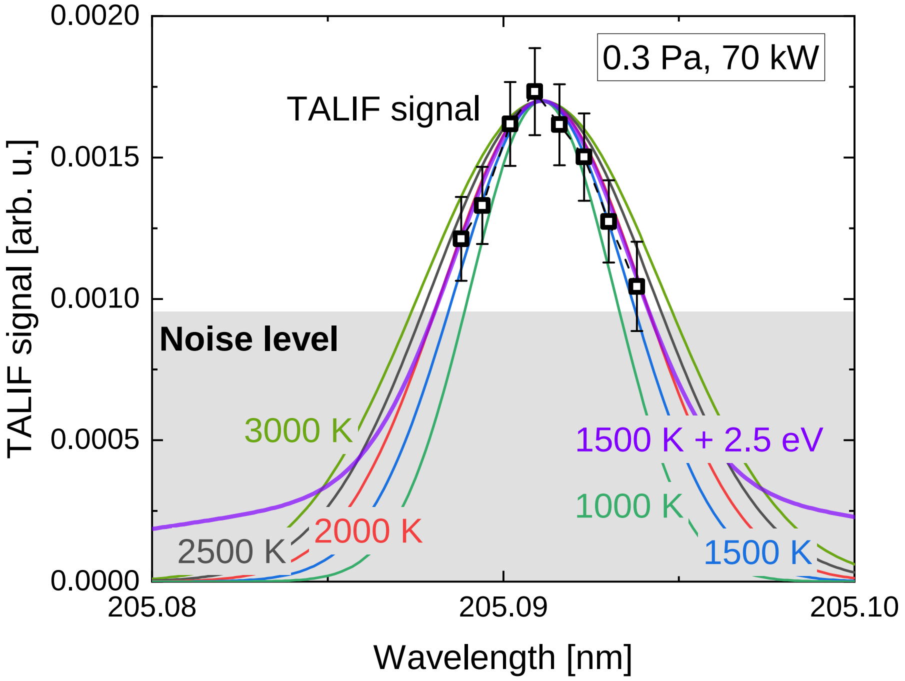

Figure 6.12: *Two-photon absorption line profile measured at BUG in a H_2 plasma at* 0.3 *Pa and 70 kW. Several line profiles are additionally depicted for comparison.*

in chapter 5.2.4. For H atoms, the additional uncertainty is 13 % and for D atoms, it is 15 %.

6.3.3 Observed line profiles

The two-photon absorption line profile as observed at BATMAN Upgrade for a H_2 plasma with a pressure of 0.3 Pa and an RF power of 70 kW is depicted in figure 6.12. In the wings of the profile, no evaluation of the TALIF signal could be performed due to the noise level such that only the central part of the profile can be measured reliably. For pressures between 0.3 Pa and 0.6 Pa at 70 kW no substantial changes regarding the line profile were observed.

In addition, multiple calculated line profiles are depicted in order to assess the temperature of H atoms. These represent convolutions of a Doppler broadened line profile at a given temperature with the laser line width according to equation (3.10). Within their error bars, the measured data points agree fairly well with the single temperature line profiles for temperatures between 1500 K and 2500 K while the profile arising from 2000 K fits best to the measured data points. This coincides with the value 2200 K of the cold temperature that is reported in [FBH+21]. The hot temperature that was determined in this study is 2.5 eV with a ratio between the two populations between 0.3 and 1. Assuming a two-temperature distribution among the H atoms with this hot temperature of 2.5 eV, the data points can be well reproduced with the additional cold temperature of 1500 K assuming a ratio of 1 between the hot and the cold populations. The resulting line profile is also shown in figure 6.12. However, due to the noise level, a hot share would not be detectable for the TALIF system. A two-temperature distribution of H atoms can therefore neither be verified nor falsified with the installed TALIF system.

For the evaluation of the TALIF signals in order to determine n_{H}, it is assumed that the line profile follows a Gaussian as suggested by the line profile center. Compared to this, the shown two-temperature distribution would cause an increase of the determined H atom density by 50 %. This is determined by the ratio of the areas of the corresponding line profile with the line profile for 2000 K.

Line profiles were only recorded for a variation of pressure between 0.3 Pa and 0.6 Pa at an RF power of 70 kW. For all other conditions investigated in this work, TALIF is only performed at the line profile center due to time constrains. In those cases, a line profile needs to be assumed for the determination of n_{H}. As all observed line profiles had the same shape, a Doppler broadened line profile at 2000 K is taken for this. Due to this, an additional uncertainty is assigned to the random error which is computed by varying the assumed temperature within 1500 K and 2500 K giving an upper and a lower boundary for the determined n_{H}. The error is the average deviation of the two n_{H} values from the one determined for 2000 K and has a value of roughly 15 %.

For the operation of BUG with D_2, at 0.6 Pa and 70 kW a line profile was observed which also resembles a Doppler broadened line profile for a D temperature of 2000 K in the line center. Also here, the wings of the line profile could not be resolved such that a two-temperature distribution of deuterium atoms can neither be verified nor falsified. For the other ion source parameters investigated for D_2, TALIF was therefore only performed with a wavelength at the center of the line profile and a Gaussian line profile for 2000 K is used for the evaluation.

6.4 Variation of pressure and RF power

In order to investigate the behaviour of $n_{\mathrm{H/D}}$ in the BATMAN Upgrade ion source, two parameter variations are conducted. For H_2 as working gas, these are a scan of the RF power between 20 kW and 70 kW at the two pressures 0.3 Pa and 0.6 Pa and a scan of the ion source pressure between 0.3 Pa and 0.6 Pa at a constant value

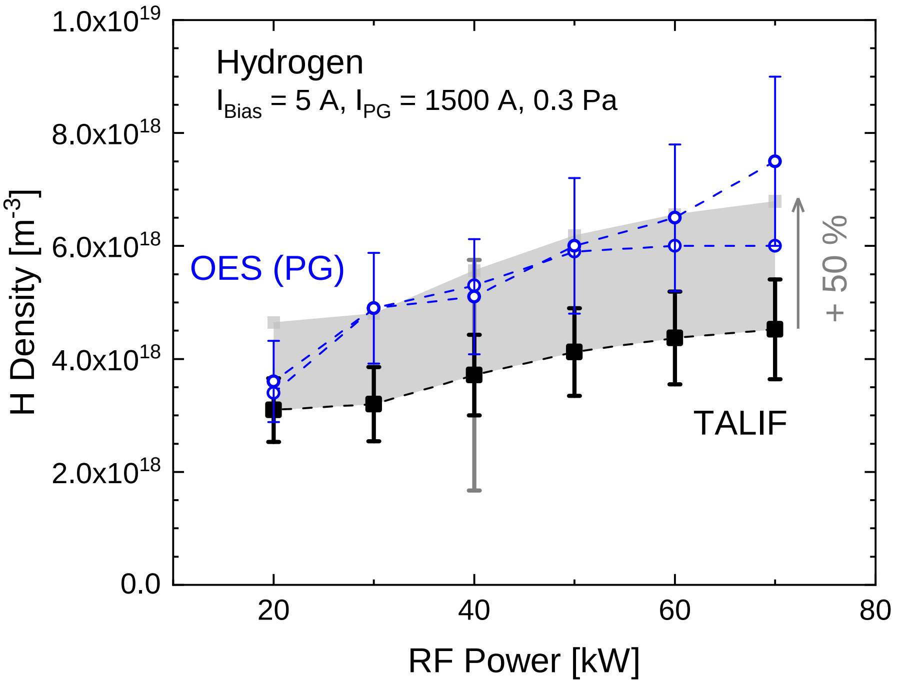

Figure 6.13: *Atomic densities in BUG determined via TALIF and OES for the variation of the RF power at a pressure of* 0.3 *Pa.*

of the forwarded RF power of 70 kW. In D_2, only the pressure scan is performed. For all conducted experiments, the bias current to the PG is fixed at 5 A and current through the plasma grid (I_{PG}) is kept at a value of 1.5 kA for H_2 and 2.2 kA for D_2 respectively. These are typical values that are applied during ion beam operation. The higher I_{PG} for the operation with deuterium is necessary in order to limit the co-extracted electron current which is generally higher when BUG is operated with deuterium [WWR+21].

6.4.1 Variation of the RF power

Comparison to OES

The n_H values obtained for the scan of the RF power at a pressure of 0.3 Pa are depicted in figure 6.13. Both the results of TALIF and OES are shown. In the case of OES, only the results of the two LOS close to the PG are shown in order to compare them to the TALIF result. The two OES results agree well besides the data points at 70 kW such that the H atom density is considered uniform within the region observed by TALIF and OES.

While the n_H values obtained by TALIF rise from $3 \times 10^{18}\,m^{-3}$ to $4.5 \times 10^{18}\,m^{-3}$ throughout the power scan, the values found with OES are systematically higher by

~ 50 %. This condition is the opposite as was observed in chapter 5.3 at ALFRED. The relative behaviour observed with the two diagnostics is similar. Two points can be raised in order to assess the difference between the two diagnostics observed here:

- The TALIF density values that are shown here are measured only at the center of the transition line profile and a Gaussian line shape at a temperature of 2000 K is assumed for the evaluation. A two-temperature profile as suggested by OES would lead to an increase of n_H by 50 % which is assigned in figure 6.13 with the gray shaded area. In that case, TALIF and OES coincide.
- The OES is evaluated using optically thin Yacora H and H_2 results. On the other side, the influence of photon re-absorption causes the resulting n_H value to drop as pointed out in chapter 5.3. The shown OES results therefore overestimate the true H atom density in the plasma.

Adding the contributions of the two points, the OES value is again lower than the result obtained by TALIF as is expected from the measurements at ALFRED. However, the impact of both effects is uncertain. The stated value of 50 % refers to a density ratio of cold and hot H atom population of 1. TALIF measurements at a higher signal to noise ratio are required in order to determine the full line profile to assess this. The impact of photon re-absorption on the determined n_H can not be estimated due to the complex geometry and spatial emission profile. Despite this, the resulting n_H values obtained with TALIF and OES are reasonably close such that agreement between the two diagnostics is found.

Measurements in hydrogen at 0.3 Pa and 0.6 Pa

The n_H values as determined by TALIF for the power scans at the two pressures of 0.3 Pa and 0.6 Pa are shown in figure 6.14. As discussed earlier, n_H rises from $3 \times 10^{18}\,\mathrm{m}^{-3}$ to $4.5 \times 10^{18}\,\mathrm{m}^{-3}$ for 0.3 Pa (factor 1.5) while it rises from $4 \times 10^{18}\,\mathrm{m}^{-3}$ to $10 \times 10^{18}\,\mathrm{m}^{-3}$ for 0.6 Pa (factor 2.5) such that the H atom density increase is weaker for the lower pressure.

An increase of n_H with rising forwarded RF power as observed for both pressures is generally expected in LPLT plasmas. This is due to the increase of n_e (outlined in chapter 2.1.2) enhancing the electron impact dissociation rate in the plasma. The fact that this increase of n_H is less pronounced for 0.3 Pa compared to 0.6 Pa

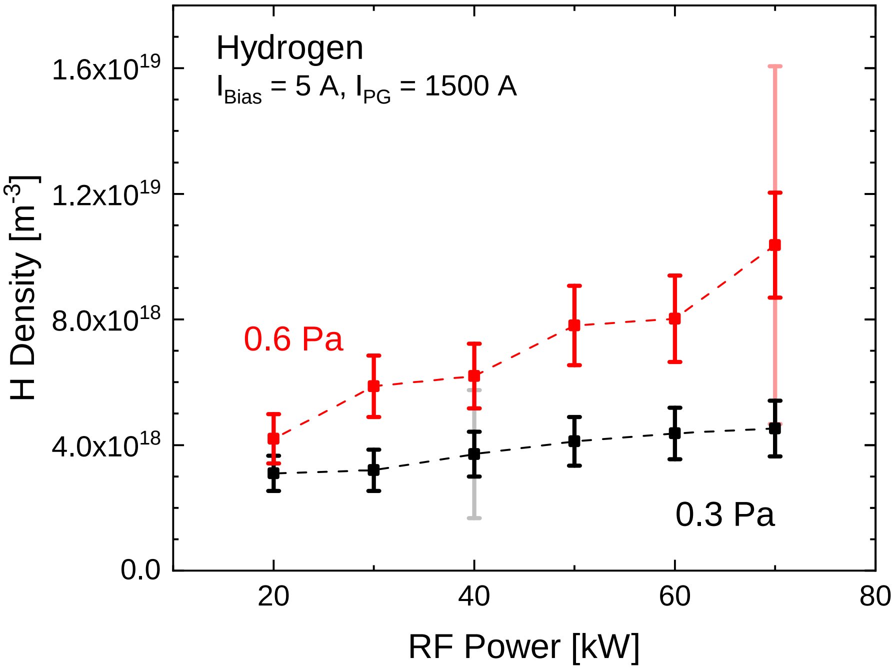

Figure 6.14: *Atomic densities in BUG determined for the variation of the RF power for hydrogen at the two ion source pressures* 0.3 *Pa and* 0.6 *Pa.*

can be attributed to *neutral depletion* which was already observed in BUG in earlier studies [MW11, FGH+17, ZBLF22]. This effect describes the reduction of the neutral particle densities in the plasma center compared to the region close to the vessel walls and it is broadly reviewed in [Fru17]. The depletion of neutrals can be caused by several possible mechanisms being elevated electron pressure in the discharge center, heating of the neutral particles or strong ionization of the neutrals within the plasma center. All of these are present at high RF power and low pressure explaining the behaviour of n_H at 0.3 Pa compared to 0.6 Pa. In [MW11], the atomic to molecular hydrogen density fraction $\frac{n_H}{n_{H_2}}$ is determined both in the driver and close to the PG for a variation of the forwarded RF power at 0.3 Pa. Here, $\frac{n_H}{n_{H_2}}$ is determined by measuring the ratio of the H_γ line emissivity to the emissivity of the total Fulcher radiation and it is found to follow the relative behaviour of n_H at 0.3 Pa in figure 6.14 closely. In [FGH+17], a scaled version of the ion source of BATMAN Upgrade is modelled with a DSMC (direct simulation Monte Carlo) code which models among others the H atom density and its energy distribution function. A variation in power for different filling pressure values gives a similar behaviour of n_H as in figure 6.14. Ultimately, in [ZBLF22], the ion source of BUG is modelled with a fluid model simulating the spatially resolved properties of neutrals, electrons and ions. For a modelled pressure of 0.3 Pa and

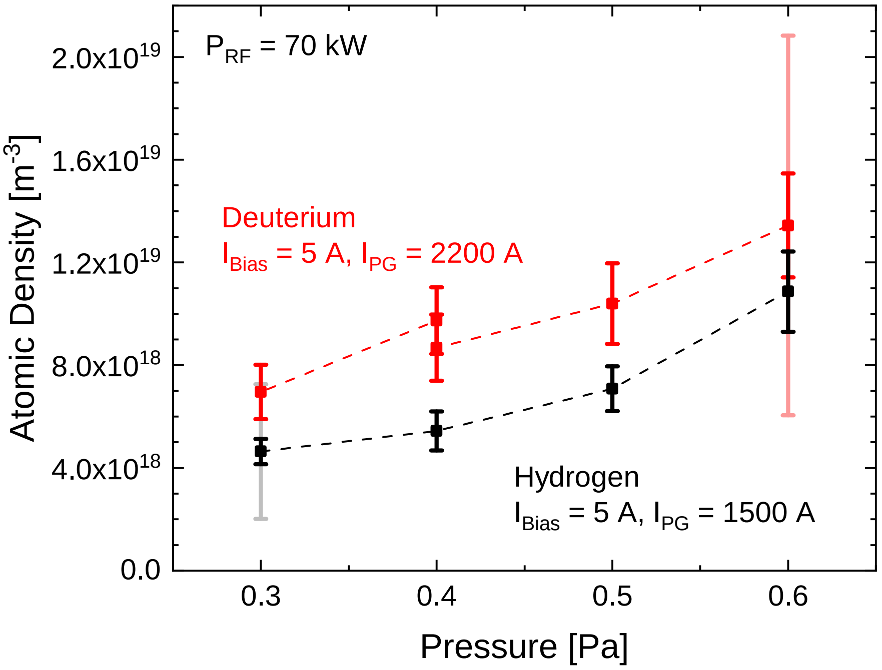

Figure 6.15: *Atomic densities in BUG determined for the variation of the ion source pressure for hydrogen and deuterium.*

varying RF power, the density of neutrals (sum of atoms and molecules) in the ion source is observed to lower for increasing power.

6.4.2 Variation of the source pressure

The result of the TALIF measurements for the variation of the pressure in the ion source is shown in figure 6.15. In general, the atomic density rises for both isotopes, from $4.5 \times 10^{18}\,\mathrm{m}^{-3}$ to $1.1 \times 10^{19}\,\mathrm{m}^{-3}$ for the operation with hydrogen and from $7 \times 10^{18}\,\mathrm{m}^{-3}$ to $1.3 \times 10^{19}\,\mathrm{m}^{-3}$ for the operation with deuterium. The obtained values for the hydrogen plasma agree well with the previous results in figure 6.14.

The atomic density increase of deuterium compared to hydrogen corresponds to a factor of 1.5 to 1.2 which coincides well with the value of 1.5 which is reported in [FFF+06]. Again, several reasons can cause this isotope effect being the slower diffusion of deuterium atoms to the vessel walls prior to recombination, the altered electron impact dissociation cross section and a higher electron density which is found in the driver for D_2 plasmas [ZBF21].

6.5 Discussion of the obtained results

The results of the TALIF measurements of n_H and T_H need to be checked for consistency with the *extracted* negative ion current. In [WFA+17], it is shown that the extracted negative ion current scales with the atomic to molecular hydrogen fraction. However, the influence of n_H and T_H on the ion current is by no means straightforward. Although these parameters determine the flux of H^- ions that is produced at the PG surface, the transportation of H^- from the PG towards the apertures contains more complexity. This process is investigated in [GWF09, GWF10] exhibiting a strong dependence of the H^- extraction probability on the starting energy of the H^- as well as their starting position and ion source parameters such as the filter field strength. Following this, the negative ions are extracted from the plasma. The extraction of negative ions is investigated for example in [WML+21] while considering the complex magnetic field structure close to the PG and showing its influence on the extraction of negative ions. Summing up these considerations leads to a probability of H^- extraction of ~ 30 % [GWF09, GWF10] depending on the position of the H^- creation.

For the performed estimation, these effects are omitted due to their complexity. Physically speaking, an extraction probability of 1 for the H^- that are produced at the PG surface is assumed. H^- ions that are produced at other surfaces in the ion source are not considered for this estimation as their path to the extraction apertures is long such that the extraction probability is even lower compared to the PG. The produced H^- flux leaving the PG is calculated using equation (2.28) with input parameters of the TALIF measurements at 0.3 Pa and 70 kW. Integrating this flux over the total area of the PG gives the extracted ion current for an extraction probability of 1. The resulting H^- flux is

$$\Gamma_{\mathrm{H}^-} = 6.5 \times 10^{17}\,\mathrm{m}^{-2}\mathrm{s}^{-1}\,.$$

This calculation depends on the negative ion conversion yield $\beta^-(v_x)$ and the perpendicular velocity distribution function $f_{v_x,\mathrm{H}}(v_x)$ of the H atoms. The used $\beta^-(v_x)$ is taken from [SCI+96] and is shown in figure 2.4. It corresponds to a work function of 1.5 eV. $f_{v_x,\mathrm{H}}(v_x)$ is calculated for a Maxwell-Boltzmann VDF at $T_\mathrm{H} = 2000\,\mathrm{K}$ and $n_\mathrm{H} = 5 \times 10^{18}\,\mathrm{m}^{-3}$. For this, isotropy of the H atoms is assumed since the H atom temperature determined by TALIF corresponds to the VDF parallel to the laser beam which is parallel to the PG surface whereas the VDF for the velocity perpendicular to the PG is used in equation (2.28). Setting Γ_{H^-} in relation to the impinging flux of H atoms on the PG surface yields a conversion yield of below 0.01 %. The resulting H$^-$ current density is 0.1 Am^{-2}. The dimensions of the PG are 305 mm × 125 mm. Obviously, no H$^-$ can be produced in the aperture holes such that their area is subtracted from the available area. Out of 70 apertures, 10 were masked during the conducted experiments such that a total area of 0.029 m^2 is left for H$^-$ production. The total H$^-$ current that is produced at the PG is

$$I^{\mathrm{H}^-}_{\mathrm{prod}} = 0.0029\,\mathrm{A}\,.$$

This value needs to be compared to the extracted H$^-$ current from a BUG pulse at comparable ion source parameters in a caesiated environment. This means also that the work function is expected to be similar to the value that is used for the calculation. In order to ensure that the presence of Cs in the plasma does not affect the plasma in such a way that the two BUG pulses are not comparable, the emissivities of the Balmer lines α to γ as well as the total Fulcher emission are recorded with the survey spectrometer. The difference in the emissivities is below 15 % for each line and the respective line ratios $\frac{\epsilon_\alpha}{\epsilon_\beta}$, $\frac{\epsilon_\alpha}{\epsilon_\gamma}$ and $\frac{\epsilon_\gamma}{\epsilon_{\mathrm{Ful}}}$ are equal within less than 10 %. Thus, the two pulses are considered as comparable. Under caesiated conditions and applying an extraction voltage of $U_{\mathrm{ext}} = 6\,\mathrm{V}$, the teststand yields an extracted H$^-$ ion current of

$$I^{\mathrm{H}^-}_{\mathrm{ext}} = 1.5\,\mathrm{A}$$

which exceeds the estimated total produced H$^-$ ion current by more than two orders of magnitude. Even using the highest values of n_{H} and T_{H} within their error bars ($n_{\mathrm{H}} = 7.5 \times 10^{18}\,\mathrm{m}^{-3}$ and $T_{\mathrm{H}} = 2500\,\mathrm{K}$) gives a total produced current of only 0.014 A emerging from the steep incident energy dependence of the conversion yield. At higher temperature, more energetic H atoms impinge the conversion surface leading to a strongly increased amount of produced H$^-$ ions. The discrepancy between the estimated and the measured H$^-$ current could be accounted for by mainly three points.

- The presence of a hot share of H atoms is reported in [FBH+21]. The two-temperature distribution of H atoms that is depicted in figure 6.12 with a hot temperature of 2.5 eV and a cold temperature of 1500 K gives a value of the produced H$^-$ current of

$$I_{\mathrm{prod}}^{\mathrm{H}^-} = 10.2\,\mathrm{A}\,.$$

For this calculation, the H atom density is evaluated for the two-temperature line profile which leads to an increase of 50 % of the total H atom density whereas the ratio of the hot and the cold population is 1:1. This estimate is more compatible with the measured extracted ion current since generally an extraction probability considerably lower than 1 is expected [GWF09, GWF10]. The presence of a highly energetic share of H atoms is further backed by the results of the DSMC code modelling a scaled version of the ion source of BATMAN Upgrade reported in [Koh15]. From the modelled velocity distribution function of H atoms near the PG, the generated flux of H$^-$ is calculated to be 700 Am^{-2} at a H atom density of $9.3 \times 10^{18}\mathrm{m}^{-3}$. Scaled to the density which is observed in this work and integrated over the PG surface, this corresponds to a produced H$^-$ current of

$$I_{\mathrm{prod}}^{\mathrm{H}^-} = 10.8\,\mathrm{A}\,,$$

which is also compatible with the observed extracted negative ion current. In general, a hot share of H atoms could therefore close the gap between the extracted H$^-$ current and the expected surface-produced current from the PG based on the observed central part of the H atom line profile.

The presence of this hot population of H atoms could not yet be verified in the experiment directly as OES only investigates excited state atoms. This verification is possible with TALIF as these atoms are visible in the wings of the observed line profile. In that region, the noise level is very high and measures must be taken against it to carry out this verification. These could be an improvement of the light collection, the data acquisition and the evaluation procedure.

- Fast positive ions could play an important role i nthe formation of negative ions at the PG. They can be accelerated by the plasma potential within the ion source which drops between the driver region and the expansion region towards the PG. This potentially leads to an acceleration of positive ions towards the PG [Bac12]. This could lead to high fluxes of energetic positive ions which leads to a considerable production of negative ions. A thorough treatment of this matter results in a minor role of positive ions in the H^- production [WSM+12] which is also backed by the result of the DSMC model in [Koh15]. However, quantitative measurements of the positive ion flux on the PG have not yet been conducted at BATMAN Upgrade such that these findings are not fully validated yet. Such measurements could help in order to understand the relevance of this process.

- The calculations of the expected extracted H^- current are based on the negative ion yield that is calculated in [SCI+96] for a work function of $\chi = 1.5\,\mathrm{eV}$. Recent measurements of the work function in a H_2 plasma environment revealed work functions down to 1.25 eV [HFF22]. According to equation (2.27), a lower value of χ leads to an exponential growth of the conversion yield such that a higher negative ion flux is expected if a work function on the order of 1.25 eV is present at the surface of the PG. In [BW13], negative ion yields are estimated for varying work function values between 1.4 eV and 2.2 eV. Extrapolating the obtained results down to $\chi = 1.25\,\mathrm{eV}$ and comparing this to the result for $\chi = 1.5$ gives an increase of the yield by a factor of less than 2 which is not sufficient in order to explain the orders of magnitude that are required in the present case.

Thus, the apparent discrepancy between the H^- current that is expected from the measured n_H and T_H and the extracted H^- current can be resolved on multiple ways such that the measured data is reasonable in the context of the other parameters that are known from the ion source. The most promising being the presence of highly energetic H atoms which dramatically increases the conversion yield due to its strong dependence of the incident H atom energy. These energetic atoms could be verified by improving the sensitivity of the TALIF system.

7 Summary and Conclusions

One of the key components of the experimental nuclear fusion reactor ITER that is currently under construction is the neutral beam injection (NBI) which is used in order to sustain the temperature of 150 million °C within the fusion plasma and to drive a current in the plasma center. The ITER NBI is based on a source of H^-/D^- ions which are accelerated with a high voltage of up to 1 MeV and subsequently neutralised in a gas target. The negative ion source has to satisfy high demands concerning the delivered ion beam current, its uniformity and temporal stability during pulses of up to one hour length. It is built after the tandem principle where an inductively coupled hydrogen[1] plasma is created in the driver and expands in turn towards the plasma grid. During the expansion, electrons are cooled due to the presence of a magnetic filter field such that an environment is created close to the plasma grid which reduces the destruction of H^- by electron collisions. H^- is believed to be predominantly created at the plasma grid surface via the conversion of hydrogen atoms. In order to enhance the probability of this process, the plasma grid is covered with caesium lowering the work function of the plasma grid surface. Subsequently, the produced H^- is extracted through the plasma grid and accelerated towards the desired energy.

The teststand BATMAN Upgrade is operated in order to conduct research and development aimed towards further optimisation of the ion source towards ITER and beyond. The ion source of BATMAN Upgrade (1/8 the size of the ITER NBI ion source) is operated with an RF power of up to 100 kW and the ions are extracted and accelerated with a high voltage of up to 45 kV. It can be operated with both H_2 and D_2 from the ITER-relevant pressure of 0.3 Pa to 0.6 Pa. The produced H^- flux from the PG surface into the ion source depends directly on the H atom density and temperature (n_{H} and T_{H} respectively) such that the knowledge of these parameters in the vicinity of the plasma grid and their dependence on the ion source parameters is of great importance for further optimisation of the source. Until now, these parameters were determined indirectly

---

[1] The term hydrogen denotes the two isotopes hydrogen and deuterium in the following.

via optical emission spectroscopy (OES). n_H was determined by comparing the plasma emission originating from the region close to the plasma grid to a collisional radiative model and T_H results from the broadening of the Balmer lines. In earlier studies, values of n_H between $6 \times 10^{18}\,\mathrm{m}^{-3}$ and $2 \times 10^{19}\,\mathrm{m}^{-3}$ have been found close to the plasma grid depending on the source operation parameters. In the case of T_H, a two-temperature distribution among H atoms was found suggesting a hot share of H atoms at a temperature of 2.5 eV while the cold temperature is at 2200 K. However, the plasma close to the plasma grid is recombining such that the plasma emission depends on multiple further species densities and temperatures. This allocates the determination of n_H via OES with high error bars. T_H is determined strictly speaking only for the excited state H atoms as their emission is investigated. This temperature is not necessarily equal to the ground state temperature. A direct determination of n_H and T_H is therefore strongly desired. The aim of this work was therefore the installation of a *two-photon absorption laser induced fluorescence* (TALIF) diagnostic at BATMAN Upgrade offering this direct access. This technique is well established for hydrogen plasmas but has never been demonstrated at negative hydrogen ion sources so far.

TALIF is based on the excitation of ground state H atoms into the $n = 3$ state via the simultaneous absorption of two photons at 205.08 nm emitted by a laser. Subsequently, the excited H atoms decay in the course of the H_α transition at 656.3 nm and the generated fluorescence is collected by a photomultiplier tube (PMT). The fluorescence signal is measured for varying the laser wavelength such that the two-photon absorption line profile is recorded. From this, the temperature of H atoms can be deduced if Doppler broadening is the main broadening mechanism and spectral integration of the line profile yields the H atom density. For absolute density values, the TALIF system needs to be calibrated. For this, krypton gas at a known density is filled into the investigated experiment as it exhibits a two-photon transition at 204.14 nm within the spectral range of the laser. This transition is probed and the recorded signal of the resulting fluorescence at 826 nm is compared to the hydrogen signal for calibration. The two-photon absorption cross section is very low such that a pulsed laser system is necessary for the generation of a laser beam at sufficient intensity. This system consists of multiple laser stages and further optics are employed for the diagnostic such as attenuation optics and the PMT. These need to be adjusted and tested prior to the measurements which is barely possible directly at the ion source due to the harsh RF and high voltage environment limiting the access to the ion source. Therefore, TALIF was assembled and tested thoroughly at the small-scale inductively coupled plasma experiment ALFRED which was specifically built for this during this work. In a second step, the diagnostic was transferred to BATMAN Upgrade and installed there.

The TALIF system which was assembled consists of a three-stage laser system containing a frequency doubled Nd:YAG laser (100 Hz repetition rate) seeding a dye laser. The output of the dye laser is frequency tripled resulting in the laser pulses around 205 nm. The laser was operated at an output energy per laser pulse of 600 µJ. After the laser exit, a $\lambda/2$ plate and a Rochon polarizer serve as a variable attenuator and a photodiode is used in order to monitor the laser intensity. The optical system can be connected to BUG and ALFRED with a laser beam guided built of multiple mirrors. At the respective experiment, the fluorescence is collected with a lens system and optical fibre equipped with spectral filters for the H and Kr fluorescence. A PMT is connected to the other end of the fibre serving as a light detector.

At ALFRED, the fluorescence collection system was calibrated concerning its transmission which consists of the filter transmissions and the transmission of the fibre for the H and the Kr fluorescence. In addition, the sensitivity of the PMT at the two fluorescence wavelengths of H and Kr is cross calibrated with the spectrometer which is used for OES. Both for the filter transmissions and the PMT sensitivities, a considerable deviation from the specified values was observed underlining the need for this calibration. Preliminary TALIF experiments were performed on krypton with the aid of testing the measurement procedure and determining the line profile of the laser. A fluorescence decay time close to the literature value of 28.5 ns was observed for Kr pressures between 1 Pa and 10 Pa demonstrating the absence of quenching in this pressure range. Saturation of the TALIF signal was observed for a laser energy per pulse higher than 25 µJ. The line shape of the laser was found to cause an effective broadening of the hydrogen absorption line profile of 1 pm which is corrected for the T_H determination. TALIF measurements on hydrogen exhibited a fluorescence decay time that depends on the density of H atoms and is between 11 ns at $n_\mathrm{H} \sim 10^{19}\,\mathrm{m}^{-3}$ and 14 ns at $n_\mathrm{H} \gtrsim 2 \times 10^{20}\,\mathrm{m}^{-3}$. This hints towards the presence of l-state mixing causing a decay time of 10 ns in combination with photon re-absorption prolonging this decay time. As well, the saturation regions of the TALIF signals were evaluated for hydrogen and deuterium. The TALIF system proved to be reliable and the average fluorescence signal of 300 laser pulses was sufficient for the evaluation.

This system was automatized within a LabVIEW program developed for this purpose.

The aim of the investigations at ALFRED was the use of TALIF for a broad range of measured H atom densities for a thorough validation of the implemented setup and in order to operate it at similar H atom densities as expected at BATMAN Upgrade. This was achieved by operating TALIF on H_2 plasmas at varying pressure as well as plasmas containing a mixture of H_2 and He with low hydrogen content. Further, D_2 plasmas were investigated in order to determine the influence of a change between the two isotopes hydrogen and deuterium. For all measurements, the TALIF results are compared to measurements with OES. The determined H atom densities were in the range between $2 \times 10^{19}\,\mathrm{m}^{-3}$ (in the H_2/He mixture plasma) and $2 \times 10^{20}\,\mathrm{m}^{-3}$ (for the pure H_2 plasma). In the course of this, the relative behaviour of n_H can be explained by the behaviour of n_e and T_e. This was confirmed by comparing the TALIF results in the H_2 plasma to a dissociation model. n_e and T_e follow the behaviour as outlined by global power and particle balance models. When operating ALFRED with deuterium an atomic density between $2 \times 10^{20}\,\mathrm{m}^{-3}$ and $5 \times 10^{20}\,\mathrm{m}^{-3}$ was observed which is higher by factor of 2.5 compared to H_2 plasmas at the same pressure and, however, lower power coupled to the plasma. This isotope effect could be caused by the mass dependence of diffusion causing a slower atomic deuterium loss at the plasma vessel walls or the isotope dependence of the electron impact dissociation cross section. However, both effects are not pronounced enough to account for the factor 2.5 such that the full reason remains unresolved. The atomic temperature was found to be in the range between 400 K and 700 K and reasonably close to the gas temperature determined by OES. A comparison of the atomic density determined by TALIF and the corresponding result by OES using the optically thick evaluation yields that the OES data is systematically lower than the TALIF data by a factor of 1.5 to 2.5 for hydrogen and 3 to 3.5 for deuterium. In order to determine the cause of this, OES was also evaluated optically thin revealing an increase of n_H which was, however, not sufficient for resolving the discrepancy although completely neglecting the process of photon re-absorption. This leaves uncertainties in the TALIF calibration as well as a possible underestimation of the H_α branching ratio in the evaluation of the TALIF results as further possible causes of this overestimation. Both effects lead to an overestimation of n_H by TALIF. Therefore, the two diagnostics agree reasonably well in an ionizing plasma.

With this experience, the TALIF could be transferred to BATMAN Upgrade. The connection of the laser to BUG was established by using guiding mirrors which are enclosed by PVC tubing. PVC tubes are also used in order to enclose the the laser beam over its full length of 12 m. They were attached to the floor or the ceiling in order to minimize vibrations. This results in a total transmission of 30 % of the laser beam such that a maximum energy per pulse of 200 µJ was achieved within the ion source. The laser was guided into the ion source at a distance of 2.5 cm from the plasma grid and the fluorescence was collected perpendicular to the laser beam. A slit mask of 3 mm was used in order to limit the background radiation of the plasma and 4000 laser pulses were used for the measurement of one data point in order to minimize noise. Nevertheless, the radiation background of the plasma was observed to be higher by a factor of 10 compared to the fluorescence signal and considerable noise was present in the signal. The evaluation of the TALIF signals was therefore only possible close to the center of the two-photon absorption line profile by operating the laser energy in the saturation regime. Absolute densities were determined by correcting the saturation.

With this setup and evaluation, the very first TALIF measurements at a negative hydrogen ion source were possible. The dedicated TALIF campaign at BATMAN Upgrade was carried out without Cs evaporation into the ion source in order to guarantee the stability of the plasma during the TALIF signal acquisition and no negative ions were extracted. The campaign consisted of a pressure scan (0.3 Pa - 0.6 Pa) at 70 kW both with H_2 and D_2 plasmas and a power scan (20 kW - 70 kW) at 0.3 Pa and 0.6 Pa with a H_2 plasma. Line profile measurements could only be performed in the line center due to the low signal to noise ratio at the wings of the line profile. The central part corresponds to an atomic temperature between 1500 K and 2500 K for all investigated pressures both in hydrogen and deuterium. A second hotter component of the atomic energy distribution function could not be confirmed due to the low signal quality in the line profile wings. The absolute densities observed with TALIF were in the range between 3×10^{18}m^{-3} and 1.1×10^{19} m^{-3}. For high power at 0.3 Pa, the effect of neutral depletion was observed. In the D_2 plasma, the atomic density was found to be systematically higher compared to hydrogen by a factor of 1.2 to 1.5 exhibiting an isotope effect concerning the atomic density. The TALIF results were compared to n_H determined by OES. Here, the OES results were systematically higher than the TALIF results by a factor of 1.5. Partly, this can be explained by the fact that the OES evaluation was performed optically thin such that n_H is overestimated by this diagnostic. Further, a two-temperature line profile was not considered for TALIF causing a possible underestimation of n_H by TALIF if that distribution is present in the plasma. Considering this, the OES was therefore found to be in good agreement with TALIF also in the recombining plasma.

The n_H and T_H determined by TALIF were used in order to estimate the extracted ion current from the ion source and compare this value to the current measured with a cesiated ion source at comparable source parameters. The expected H^- production at the plasma grid due to the observed H atoms can not account for the extracted H^- current. This discrepancy could be resolved by assuming a hot population of H atoms or by a more relevant role of positive ions in the H^- production. An improvement of the TALIF signal to noise ratio at the line profile wings of the transition could resolve this issue by verifying or falsifying the presence of hot H atoms.

Summarizing this, the TALIF diagnostic could be implemented at the negative hydrogen ion source BATMAN Upgrade despite the multiple challenges that needed to be overcome. This marks the first time that TALIF is performed at such a source. The challenges could be overcome by first installing TALIF at the small scale experiment ALFRED collecting experience and setting up the measurement procedure. With this experience, the transfer of the laser beam to BATMAN Upgrade could be accomplished and the TALIF signal could be made visible against the strong H_α background such that quantitative measurements were possible. However, an improvement of the system is still possible by increasing the signal to noise ratio making the wings of the TALIF line profile accessible.

Bibliography

[ABF78] C. P. Ausschnitt, G. C. Bjorklund, and R. R. Freeman. *Hydrogen plasma diagnostics by resonant multiphoton optogalvanic spectroscopy.* Applied Physics Letters, **33** (1978), 851–853.

[Arg74] J. D. Argyros. *Photodissociation of H_2^+: variation with temperature.* Journal of Physics B: Atomic and Molecular Physics, **7** (1974), 2025–2035.

[Bac06] M. Bacal. *Physics aspects of negative ion sources.* Nuclear Fusion, **46** (2006), S250–S259.

[Bac12] M. Bacal. *Effect of fast positive ions incident on caesiated plasma grid of negative ion source.* Review of Scientific Instruments, **83** (2012), 02B101.

[BAFS78] G. C. Bjorklund, C. P. Ausschnitt, R. R. Freeman, and R. H. Storz. *Detection of atomic hydrogen and deuterium by resonant three-photon ionization.* Applied Physics Letters, **33** (1978), 54–56.

[BDD74] Y. Belchenko, G. Dimov, and V. Dudnikov. *A powerful injector of neutrals with a surface-plasma source of negative ions.* Nuclear Fusion, **14** (1974), 113–114.

[Beh91] K. Behringer. *Diagnostics and modelling of ECRH microwave discharges.* Plasma Physics and Controlled Fusion, **33** (1991), 997–1028.

[Beh98] K. Behringer. *Escape Factors for Line Emission and Population Calculations.* IPP Report 10/11, Max-Planck-Insitut für Plasmaphysik, 1998.

[BF18] S. Briefi, U. Fantz, and the NNBI Team. *Spectroscopic investigations of the ion source at BATMAN upgrade.* AIP Conference Proceedings, **2052** (2018), 040005.

[BF00] K. Behringer and U. Fantz. *The influence of opacity on hydrogen excited-state population and applications to low-temperature plasmas.* New Journal of Physics, **2** (2000), 23.1–23.19.

[BF20] S. Briefi and U. Fantz. *A revised comprehensive approach for determining the H_2 and D_2 rovibrational population from the Fulcher-α emission in low temperature plasmas.* Plasma Sources Science and Technology, **29** (2020), 125019.

[BFWS81] J. Bokor, R. R. Freeman, J. C. White, and R. H. Storz. *Two-photon excitation of the $n = 3$ level in H and D atoms.* Physical Review A, **24** (1981), 612–614.

[BHB+79] M. Bacal, G. W. Hamilton, A. M. Bruneteau, et al. *Measurement of H^- density in plasma by photodetachment.* Review of Scientific Instruments, **50** (1979), 719–721.

[Bir19] F. Biraben. *The first decades of Doppler-free two-photon spectroscopy.* Comptes Rendus Physique, **20** (2019), 671–681.

[BKHMJ88] J. Bittner, K. Kohse-Höinghaus, U. Meier, and T. Just. *Quenching of two-photon-excited H(3s, 3d) and O(3p 3P2,1,0) atoms by rare gases and small molecules.* Chemical Physics Letters, **143** (1988), 571–576.

[BM84] K. D. Bonin and T. J. McIlrath. *Two-photon electric-dipole selection rules.* Journal of the Optical Society of America B, **1** (1984), 52.

[BMB+02] M. G. H. Boogaarts, S. Mazouffre, G. J. Brinkman, et al. *Quantitative two-photon laser-induced fluorescence measurements of atomic hydrogen densities, temperatures, and velocities in an expanding thermal plasma.* Review of Scientific Instruments, **73** (2002), 73–86.

[BNH76] A. Blandin, A. Nourtier, and D. Hone. *Localized time-dependent perturbations in metals: formalism and simple examples.* Journal de Physique, **37** (1976), 369–378.

[BRF17] S. Briefi, D. Rauner, and U. Fantz. *Determination of the rotational population of H_2 and D_2 including high-N states in low temperature plasmas via the Fulcher-α transition.* J. Quant. Spectrosc. Radiat. Transfer, **187** (2017), 135–144.

[Bri22] S. Briefi. *Private communication.* Max-Planck-Institut für Plasmaphysik, (2022).

[BW13] M. Bacal and M. Wada. *Negative ion production by plasma-surface interaction in caesiated negative ion sources.* AIP Conference Proceedings, **1515** (2013), 41–48.

[BW20] M. Bacal and M. Wada. *Negative ion source operation with deuterium.* Plasma Sources Science and Technology, **29** (2020), 033001.

[BZRF22] S. Briefi, D. Zielke, D. Rauner, and U. Fantz. *Diagnostics of RF coupling in H^- ion sources as a tool for optimizing source design and operational parameters.* Review of Scientific Instruments, **93** (2022), 023501.

[CB15] P. Chabert and N. Braithwaite. *Physics of Radio-Frequency Plasmas.* Cambridge University Press, 2015.

[CCL+99] L. Chérigier, U. Czarnetzki, D. Luggenhölscher, et al. *Absolute atomic hydrogen densities in a radio frequency discharge measured by two-photon laser induced fluorescence imaging.* Journal of Applied Physics, **85** (1999), 696–702.

[Cha87] P. J. Chantry. *A simple formula for diffusion calculations involving wall reflection and low density.* Journal of Applied Physics, **62** (1987), 1141–1148.

[CMK+94a] U. Czarnetzki, K. Miyazaki, T. Kajiwara, et al. *Comparison of various two-photon excitation schemes for laser-induced fluorescence spectroscopy in atomic hydrogen.* Journal of the Optical Society of America B, **11** (1994), 2155.

[CMK+94b] U. Czarnetzki, K. Miyazaki, T. Kajiwara, et al. *Two-photon laser-induced fluorescence measurements of absolute atomic hydrogen densities and powder formation in a silane discharge.* Journal of Vacuum Science & Technology A: Vacuum, Surfaces, and Films, **12** (1994), 831–834.

[CS00] H. Conrads and M. Schmidt. *Plasma generation and plasma sources.* Plasma Sources Science and Technology, **9** (2000), 441–454.

[Cui91] H. L. Cui. *Resonant charge transfer in the scattering of hydrogen atoms from a metal surface.* Journal of Vacuum Science & Technology A: Vacuum, Surfaces, and Films, **9** (1991), 1823–1827.

[Dem05] W. Demtröder. *Experimentalphysik 3: Atome, Moleküle und Festkörper.* Springer, Berlin, Heidelberg, Deutschland, 2005.

[Dem07] W. Demtröder. *Laserspektroskopie, Grundlagen und Techniken.* Springer, Berlin, Heidelberg, Deutschland, 2007.

[DGdO+22] C. Dumitrache, A. Gallant, N. de Oliveira, et al. *Quantitative fs-TALIF in high-pressure NRP discharges: calibration using VUV absorption spectroscopy.* Plasma Sources Science and Technology, **31** (2022), 015004.

[Die58] G. Dieke. *The molecular spectrum of hydrogen and its isotopes.* Journal of Molecular Spectroscopy, **2** (1958), 494–517.

[DMT+15] G. Dilecce, L. M. Martini, P. Tosi, et al. *Laser induced fluorescence in atmospheric pressure discharges.* Plasma Sources Science and Technology, **24** (2015), 034007.

[DR92] R. Deutsch and E. Räuchle. *Influence of negative ions on the plasma boundary sheath.* Physical Review A, **46** (1992), 3442–3453.

[EB85] W. Eckstein and J. P. Biersack. *Reflection of low-energy hydrogen from solids.* Applied Physics A Solids and Surfaces, **38** (1985), 123–129.

[Edm22] Edmund Optics, Barrington, NJ, USA. *VIS-NIR Coated, Achromatic Lens*, 2022. Available via [85 mm lens] and [175 mm lens].

[EKG20] R. Engeln, B. Klarenaar, and O. Guaitella. *Foundations of optical diagnostics in low-temperature plasmas.* Plasma Sources Science and Technology, **29** (2020), 063001.

[Ell20] J. T. Ellis. *An investigation into plasma surface interactions, focussing on surface produced, and surface assisted, negative ion generation.* PhD thesis, University of York, 2020.

[Exc22] Exciton, Luxottica, Lockbourne, Ohio, USA. *DCM [online]*, 2022.

[Fan06] U. Fantz. *Basics of plasma spectroscopy.* Plasma Sources Sci. Technol., **15** (2006), 137–147.

[FBF+19] U. Fantz, F. Bonomo, M. Fröschle, et al. *Advanced NBI beam characterization capabilities at the recently improved test facility BATMAN Upgrade.* Fusion Engineering and Design, **146** (2019), 212–215.

[FBH+21] U. Fantz, S. Briefi, A. Heiler, et al. *Negative Hydrogen Ion Sources for Fusion: From Plasma Generation to Beam Properties.* Frontiers in Physics, **9** (2021), 709651.

[FF14] R. Friedl and U. Fantz. *Fundamental studies on the Cs dynamics under ion source conditions.* Review of Scientific Instruments, **85** (2014), 02B109.

[FFF+06] U. Fantz, H. Falter, P. Franzen, et al. *Spectroscopy — a powerful diagnostic tool in source development.* Nuclear Fusion, **46** (2006), S297–S306.

[FFK+07] U. Fantz, P. Franzen, W. Kraus, et al. *Negative ion RF sources for ITER NBI: status of the development and recent achievements.* Plasma Physics and Controlled Fusion, **49** (2007), B563–B580.

[FGH+17] G. Fubiani, L. Garrigues, G. Hagelaar, et al. *Modeling of plasma transport and negative ion extraction in a magnetized radio-frequency plasma source.* New Journal of Physics, **19** (2017), 015002.

[FH98] U. Fantz and B. Heger. *Spectroscopic diagnostics of the vibrational population in the ground state of and molecules.* Plasma Physics and Controlled Fusion, **40** (1998), 2023–2032.

[Fri13] R. Friedl. *Experimental investigations on the caesium dynamics in H_2/D_2 low temperature plasmas.* PhD thesis, Universität Augsburg, 2013.

[Fru17] A. Fruchtman. *Neutral gas depletion in low temperature plasma.* Journal of Physics D: Applied Physics, **50** (2017), 473002.

[FSF+11] P. Franzen, L. Schiesko, M. Fröschle, et al. *Magnetic filter field dependence of the performance of the RF driven IPP prototype source* *for negative hydrogen ions.* Plasma Physics and Controlled Fusion, **53** (2011), 115006.

[FSW13] U. Fantz, L. Schiesko, D. Wünderlich, and the NNBI Team. *A comparison of hydrogen and deuterium plasmas in the IPP prototype ion source for fusion.* AIP Conference Proceedings, **1515** (2013), 187–196.

[FW06] U. Fantz and D. Wünderlich. *Franck-Condon factors, transition probabilities, and radiative lifetimes for hydrogen molecules and their isotopomeres.* Atomic Data and Nuclear Data Tables, **92** (2006), 853–973.

[GAP+21] K. Gazeli, X. Aubert, S. Prasanna, et al. *Picosecond two-photon absorption laser-induced fluorescence (ps-TALIF) in krypton: The role of photoionization on the density depletion of the fluorescing state Kr* $5p'\,[3/2]_2$. Physics of Plasmas, **28** (2021), 043301.

[GKD98] A. Goehlich, T. Kawetzki, and H. F. Döbele. *On absolute calibration with xenon of laser diagnostic methods based on two-photon absorption.* The Journal of Chemical Physics, **108** (1998), 9362–9370.

[GLA+21] K. Gazeli, G. Lombardi, X. Aubert, et al. *Progresses on the Use of Two-Photon Absorption Laser Induced Fluorescence (TALIF) Diagnostics for Measuring Absolute Atomic Densities in Plasmas and Flames.* Plasma, **4** (2021), 145–171.

[GM31] M. Göppert-Mayer. *Über Elementarakte mit zwei Quantensprüngen.* Annalen der Physik, **401** (1931), 273–294.

[Gri97] H. Griem. *Principles of Plasma Spectroscopy.* Cambridge University Press, Cambridge, 1997.

[GWF10] R. Gutser, D. Wünderlich, U. Fantz, and the NNBI team. *Transport of negative hydrogen and deuterium ions in RF-driven ion sources.* Plasma Physics and Controlled Fusion, **52** (2010), 045017.

[GWF09] R. Gutser, D. Wünderlich, and U. Fantz. *Negative hydrogen ion transport in RF-driven ion sources for ITER NBI.* Plasma Physics and Controlled Fusion, **51** (2009), 045005.

[Ham22] Hamamatsu, Iwata City, Japan. *Metal package PMT with gate function*, 2022.

[HBB⁺17] R. S. Hemsworth, D. Boilson, P. Blatchford, et al. *Overview of the design of the ITER heating neutral beam injectors.* New Journal of Physics, **19** (2017), 025005.

[HDG⁺09] R. Hemsworth, H. Decamps, J. Graceffa, et al. *Status of the ITER heating neutral beam system.* Nuclear Fusion, **49** (2009), 045006.

[Her50] G. Herzberg. *Molecular Spectra and Molecular Structure: I. Spectra of Diatomic Molecules.* Van Nostrand, Toronto, New York, London, 1950.

[HFF22] A. Heiler, R. Friedl, and U. Fantz. *Impact of the photoelectric threshold sensitivity on the work function determination — Revealing ultra-low work functions of caesiated surfaces.* AIP Advances, **12** (2022), 035339.

[HFK⁺17] B. Heinemann, U. Fantz, W. Kraus, et al. *Towards large and powerful radio frequency driven negative ion sources for fusion.* New Journal of Physics, **19** (2017), 015001.

[HKO78] S. Horiguchi, K. Koyama, and Y. H. Ohtsuki. *Auger Neutralization of Slow Protons at Solid Surfaces.* Physica Status Solidi (b), **87** (1978), 757–763.

[Hol82] A. J. T. Holmes. *Electron cooling in magnetic multipole arc discharges.* Review of Scientific Instruments, **53** (1982), 1523–1526.

[Hop94] J. Hopwood. *Planar RF induction plasma coupling efficiency.* Plasma Sources Sci. Technol., **3** (1994), 460.

[IKS92] J. D. Isenberg, H. J. Kwon, and M. Seidl. *Surface production of H^- ions by backscattering of H^+ and H_2^+ ions in the 3–50 eV ion energy range.* AIP Conference Proceedings, **287** (1992), 38–47.

[Inn17] Innolas Laser GmbH, Krailling, Germany. *User Manual: SpitLight DPSS Compact 100*, 2017.

[Iro79a] F. E. Irons. *The Escape Factor in Plasma Spectroscopy - I. The Escape Factor Defined and Evaluated.* J. Quant. Spectrosc. Radiat. Transfer, **22** (1979), 1–20.

[Iro79b] F. E. Irons. *The Escape Factor in Plasma Spectroscopy - II. The Case of Radiative Decay.* J. Quant. Spectrosc. Radiat. Transfer, **22** (1979), 21–36.

[Iro79c] F. E. Irons. *The Escape Factor in Plasma Spectroscopy - III. Two Case Studies.* J. Quant. Spectrosc. Radiat. Transfer, **22** (1979), 37–44.

[Iro80] F. E. Irons. *The Escape Factor in Plasma Spectroscopy - IV. The Case of an Overlapping Doublet.* J. Quant. Spectrosc. Radiat. Transfer, **24** (1980), 119–132.

[JRS03] R. K. Janev, D. Reiter, and U. Samm. *Collision Processes in Low-Temperature Hydrogen Plasmas.* Technical Report JUEL-4105, Forschungszentrum Jülich, 2003.

[Koh15] N. Kohen. *Physique et modelisation d'une source d'ions negatifs pour l'injection du faisceau de neutres sur ITER.* PhD thesis, Universite de Toulouse III Paul Sabatier, 2015.

[KSB$^+$18] W. Kraus, L. Schiesko, F. Bonomo, et al. *First beam extraction experiments at BATMAN Upgrade.* AIP Conference Proceedings, **2052** (2018), 040004.

[LH95] W. Lochte-Holtgreven. *Plasma diagnostics.* AIP Press, New York, 1995.

[LL05] M. A. Lieberman and A. J. Lichtenberg. *Principles of Plasma Discharges and Materials Processing.* John Wiley and Sons, Hoboken, NJ, USA, 2005.

[Lou83] R. Loudon. *The quantum theory of light.* Oxford University Press, 2$^{\text{nd}}$ edition, 1983.

[Mar20] I. Mario. *Correlation between plasma and beam properties at the ELISE test facility.* PhD thesis, Universität Augsburg, 2020.

[MDZ99] M. Mozetič, M. Drobnič, and A. Zalar. *Recombination of neutral hydrogen atoms on AISI 304 stainless steel surface.* Applied Surface Science, **144-145** (1999), 399–403.

[MFB⁺21] F. Merk, R. Friedl, S. Briefi, et al. *The role of photon self-absorption on the H ($n = 2$) density determination by means of VUV emission spectroscopy and TDLAS in low pressure plasmas.* Plasma Sources Science and Technology, **30** (2021), 065013.

[MM71] G. A. Melin and R. J. Madix. *Energy accommodation during hydrogen atom recombination on metal surfaces.* Transactions of the Faraday Society, **67** (1971), 2711.

[MO99] A. F. Molisch and B. P. Oehry. *Radiation Trapping in Atomic Vapours.* Oxford University Press, 1999.

[MR02] R. L. Mills and P. Ray. *Substantial changes in the characteristics of a microwave plasma due to combining argon and hydrogen.* New Journal of Physics, **4** (2002), 22.

[MRD⁺16] M. Mrkvičková, J. Ráheľ, P. Dvořák, et al. *Fluorescence (TALIF) measurement of atomic hydrogen concentration in a coplanar surface dielectric barrier discharge.* Plasma Sources Science and Technology, **25** (2016), 055015.

[MVES01] S. Mazouffre, P. Vankan, R. Engeln, and D. C. Schram. *Behavior of the H atom velocity distribution function within the shock wave of a hydrogen plasma jet.* Physical Review E, **64** (2001), 066405.

[MW11] P. McNeely, D. Wünderlich, and the NNBI team. *Neutral depletion in an H^- source operated at high RF power and low input gas flow.* Plasma Sources Science and Technology, **20** (2011), 045005.

[Möl93] W. Möller. *Plasma and surface modeling of the deposition of hydrogenated carbon films from low-pressure methane plasmas.* Applied Physics A Solids and Surfaces, **56** (1993), 527–546.

[NIST] A. Kramida, Y. Ralchenko, J. Reader, and NIST ASD Team. *NIST Atomic Spectra Database, NIST Standard Reference Database.* NIST Atomic Spectra Database (ver. 5.9), [Online]. National Institute of Standards and Technology, Gaithersburg, MD, 2021.

[NSD01] K. Niemi, V. Schulz-von der Gathen, and H. F. Döbele. *Absolute calibration of atomic density measurements by laser-induced fluorescence spectroscopy with two-photon excitation.* Journal of Physics D: Applied Physics, **34** (2001), 2330–2335.

[OOR+89] D. K. Otorbaev, V. N. Ochkin, P. L. Rubin, et al. *Electron-excited molecules in nonequilibrium plasma*, chapter Electron-impact exctation levels of the rotational levels of molecular electron states in gas discharges, pages 121–174. Nova Science Publishers, Commack, NY, 1989.

[Phe58] A. V. Phelps. *Effect of the Imprisonment of Resonance Radiation on Excitation Experiments.* Physical Review, **110** (1958), 1362–1368.

[Phe09] A. V. Phelps. *Energetic ion, atom, and molecule reactions and excitation in low-current* H_2 *discharges: Model.* Phys. Rev. E, **79** (2009), 066401.

[Phe10] A. V. Phelps. *Erratum: Energetic ion, atom, and molecule reactions and excitation in low-current* $\mathrm{H_2}$ *discharges: Model [Phys. Rev. E 79, 066401 (2009)].* Phys. Rev. E, **81** (2010), 029903.

[PPT+95] B. Preppernau, K. Pearce, A. Tserepi, et al. *Angular momentum state mixing and quenching of* $n = 3$ *atomic hydrogen fluorescence.* Chemical Physics, **196** (1995), 371–381.

[Qio22] Qioptiq, Göttingen, Germany. *UV Grade Fused Silica Optical Windows, Standard Quality*, 2022.

[RBF17] D. Rauner, S. Briefi, and U. Fantz. *RF power transfer efficiency of inductively coupled low pressure* H_2 *and* D_2 *discharges.* Plasma Sources Sci. Technol., **26** (2017), 095004.

[Rei04] G. A. Reider. *Photonik.* Springer, Wien, New York, 2004.

[RWL82] B. Rasser, J. V. Wunnik, and J. Los. *Theoretical models of the negative ionization of hydrogen on clean tungsten, cesiated tungsten and cesium surfaces at low energies.* Surface Science, **118** (1982), 697–710.

[Sal07] E. B. Saloman. *Energy Levels and Observed Spectral Lines of Krypton, Kr I through Kr XXXVI.* Journal of Physical and Chemical Reference Data, **36** (2007), 215–386.

[SCBL02] M. D. Stewart, J. E. Chilton, J. B. Boffard, and C. C. Lin. *Use of radiation trapping for measuring electron-impact excitation cross sections for higher resonance levels of rare-gas atoms.* Physical Review A, **65** (2002), 032704.

[SCI+96] M. Seidl, H. L. Cui, J. D. Isenberg, et al. *Negative surface ionization of hydrogen atoms and molecules.* Journal of Applied Physics, **79** (1996), 2896–2901.

[SFK+21] L. H. Scarlett, D. V. Fursa, J. Knol, et al. *Isotopic and vibrational-level dependence of H_2 dissociation by electron impact.* Physical Review A, **103** (2021), L020801.

[Sha70] T. E. Sharp. *Potential-Energy Curves for Molecular Hydrogen and its Ions.* Atomic Data and Nuclear Data Tables, **2** (1970), 119–169.

[Sha71] T. E. Sharp. *Erratum: Potential-Energy Curves for Molecular Hydrogen and its Ions.* Atomic Data and Nuclear Data Tables, **3** (1971), 299.

[Shi83] K. Shimoda. *Introduction to Laser Physics.* Springer, Berlin, Heidelberg, Germany, 1983.

[Sir19] Sirah Lasertechnik, Grevenbroich, Germany. *User Manual: Pulsed Dye Laser*, 2019.

[Sir21] Sirah Lasertechnik, Grevenbroich, Germany. *Private Communiation*, 2021.

[SS68] L. W. Swanson and R. W. Strayer. *Field-Electron-Microscopy Studiesof Cesium Layers on Various Refractory Metals: Work Function-Change.* Journal of Chemical Physics, **48** (1968), 2421.

[SSS+17] J. B. Schmidt, B. Sands, J. Scofield, et al. *Comparison of femtosecond- and nanosecond-two-photon-absorption laser-induced fluorescence (TALIF) of atomic oxygen in atmospheric-pressure plasmas.* Plasma Sources Science and Technology, **26** (2017), 055004.

[Sta20] G. D. Stancu. *Two-photon absorption laser induced fluorescence: rate and density-matrix regimes for plasma diagnostics.* Plasma Sources Science and Technology, **29** (2020), 054001.

[Ste21] T. E. Steinberger. *Single and Multi-photon Laser Induced Fluorescence for Electric Thruster and Fusion Applications.* PhD thesis, West Virginia University, 2021.

[SVY12] I. I. Sobelman, L. A. Vainshtein, and E. A. Yukov. *Excitation of Atoms and Broadening of Spectral Lines.* Springer Berlin Heidelberg, 2012.

[SWM20] L. Schiesko, D. Wünderlich, and I. M. Montellano. *Kinetic sheath in presence of multiple positive ions, negative ions, and particle wall emission.* Journal of Applied Physics, **127** (2020), 033302.

[TDFP07] E. Tatarova, F. M. Dias, C. M. Ferreira, and N. Puač. *Spectroscopic determination of H, He, and H_2 temperatures in a large-scale microwave plasma source.* Journal of Applied Physics, **101** (2007), 063306.

[Tho88] A. P. Thorne. *Spectrophysics.* Chapman and Hall, London, United Kingdom, 1988.

[Tho18] Thorlabs Inc., Newton, New Jersey, USA. *System Bandwidth and Pulse Shape Distortion [online]*, 2018.

[Tho22] Thorlabs GmbH, Dachau, Germany. *0.39 NA TECS-Clad Multimode Optical Fiber, Step Index*, 2022.

[TTSC86] J. H. Tung, A. Z. Tang, G. J. Salamo, and F. T. Chan. *Two-photon absorption of atomic hydrogen from two light beams.* Journal of the Optical Society of America B, **3** (1986), 837.

[UDM+19] X. Urbain, A. Dochain, R. Marion, et al. *Photodissociation as a probe of the H_3^+ avoided crossing seam.* Philosophical Transactions of the Royal Society A: Mathematical, Physical and Engineering Sciences, **377** (2019), 20180399.

[UJ70] J. J. Uebbing and L. W. James. *Behavior of Cesium Oxide as a Low Work-Function Coating.* Journal of Applied Physics, **41** (1970), 4505–4516.

[vdHBM⁺00] H. W. P. van der Heijden, M. G. H. Boogaarts, S. Mazouffre, et al. *Time-resolved experimental and computational study of two-photon laser-induced fluorescence in a hydrogen plasma.* Physical Review E, **61** (2000), 4402–4409.

[vHBS⁺12] W. E. N. van Harskamp, C. M. Brouwer, D. C. Schram, et al. *Detailed H (n = 2) density measurements in a magnetized hydrogen plasma jet.* Plasma Sources Science and Technology, **21** (2012), 024009.

[VSE04] P. Vankan, D. Schram, and R. Engeln. *High rotational excitation of molecular hydrogen in plasmas.* Chemical Physics Letters, **400** (2004), 196 – 200.

[WBFF21] D. Wünderlich, S. Briefi, R. Friedl, and U. Fantz. *Emission spectroscopy of negative hydrogen ion sources: From VUV to IR.* Review of Scientific Instruments, **92** (2021), 123510.

[WF16a] C. Wimmer and U. Fantz. *Extraction of negative charges from an ion source: Transition from an electron repelling to an electron attracting plasma close to the extraction surface.* Journal of Applied Physics, **120** (2016), 073301.

[WF16b] D. Wünderlich and U. Fantz. *Evaluation of State-Resolved Reaction Probabilities and Their Application in Population Models for He, H, and H_2.* Atoms, **4** (2016), 26.

[WFA⁺17] C. Wimmer, U. Fantz, E. Aza, et al. *Investigation of plasma parameters at BATMAN for variation of the Cs evaporation asymmetry and comparing two driver geometries.* AIP Conference Proceedings, **1869** (2017), 030021.

[Wil66a] R. G. Wilson. *Electron and Ion Emission from Polycrystalline Surfaces of Be, Ti, Cr, Ni, Cu, Pt, and Type-304 Stainless Steel in Cesium Vapor.* Journal of Applied Physics, **37** (1966), 3161.

[Wil66b] R. G. Wilson. *Electron and Ion Emission from Polycrystalline Surfaces of Nb, Mo, Ta, W, Re, Os, and Ir in Cesium Vapor.* Journal of Applied Physics, **37** (1966), 4125.

[WML+21] D. Wünderlich, I. M. Montellano, M. Lindqvist, et al. *Effects of the magnetic field topology on the co-extracted electron current in a negative ion source for fusion.* Journal of Applied Physics, **130** (2021), 053303.

[WMS+13] D. Wünderlich, P. McNeely, L. Schiesko, et al. *Modeling the particle transport and ion production in a RF driven negative hydrogen ion source for ITER NBI.* AIP Conference Proceedings, **1515** (2013), 12.

[WSB+21] D. Wünderlich, L. H. Scarlett, S. Briefi, et al. *Application of molecular convergent close-coupling cross sections in a collisional radiative model for the triplet system of molecular hydrogen.* Journal of Physics D: Applied Physics, **54** (2021), 115201.

[WSM+12] D. Wünderlich, L. Schiesko, P. McNeely, et al. *On the proton flux toward the plasma grid in a RF-driven negative hydrogen ion source for ITER NBI.* Plasma Physics and Controlled Fusion, **54** (2012), 125002.

[WWR+21] D. Wünderlich, C. Wimmer, R. Riedl, et al. *NNBI for ITER: status of long pulses in deuterium at the test facilities BATMAN Upgrade and ELISE.* Nuclear Fusion, **61** (2021), 096023.

[YKC+21] X. Yang, D. Kogut, L. Couëdel, et al. *TALIF measurements of hydrogen and deuterium surface loss probabilities on quartz in low pressure high density plasmas.* Plasma Sources Science and Technology, **30** (2021), 015013.

[ZBF21] D. Zielke, S. Briefi, and U. Fantz. *RF power transfer efficiency and plasma parameters of low pressure high power ICPs.* Journal of Physics D: Applied Physics, **54** (2021), 155202.

[ZBLF22] D. Zielke, S. Briefi, S. Lishev, and U. Fantz. *Modeling inductive radio frequency coupling in powerful negative hydrogen ion sources: validating a self-consistent fluid model.* Plasma Sources Science and Technology, **31** (2022), 035019.

Acknowledgements

Ultimately, I want to thank all the very special people that contributed in one or the other way to this thesis. Without your help, nothing of this would have been possible. The language is chosen arbitrarily depending on the recipient.

- **Prof. Dr.-Ing. Ursel Fantz** für mittlerweile über 6 Jahre der Betreuung und Unterstützung während Bachelor-, Master- und schließlich Doktorarbeit in Augsburg und in Garching. Ich konnte viel lernen und werde davon noch lange zehren.
- **Prof. Dr. Helmut Karl** für die Übernahme des Zweitgutachtens.
- **Dr. Christian Wimmer** für die Betreuung der Doktorarbeit, die tatkräftige Hilfe bei allen Problemen auf die ich gestoßen bin, die Hilfe beim (unzähligen) Einjustieren des Lasers, den geduldigen Betrieb von BATMAN Upgrade während der TALIF-Messungen und für vieles mehr. Vielen Dank für die spannenden 3.5 Jahre!
- **Dr. Wolfgang Jacob** für die Präsenz als Scientific Counsel am IPP.
- **Dr. Stefan Briefi** für die ständige Hilfe bei allen Problemen, die ich mit der Spektroskopie oder mit dem Aufbau von ALFRED hatte, egal wie klein und (manchmal) unsinnig sie waren.
- **Dr. Roland Friedl** und **Dr. Dirk Wünderlich** für die ständige Präsenz und Hilfe bei der Interpretation meiner Daten während der gesamten Arbeit.
- **Bernd Heinemann** und **Rudolf Riedl** für die ständigen konstruktiven Beiträge zur Realisierung der TALIF an BATMAN Upgrade ohne das große Ganze aus den Augen zu verlieren.
- **Dr. Emile Carbone, Dr. Arne Meindl** and **Dr. Volker Schulz-von der Gathen** for introducing me to the fine art of TALIF, teaching me to be patient with the signals and answering countless questions on the diagnostic.

- **Dr. Alessandro Mimo, Dr. Andrew Hurlbatt, Giuseppe Starnella, Dr. Niek den Harder, Dr. Christian Hopf, Dr. Isabella Mario, Max Lindqvist, Richard Bergmayr, Dr. Dimitar Yordanov, Dr. Georgiy Zadvitskiy, Dr. Federica Bonomo, Dr. Loic Schiesko, Dr. Dominikus Zielke, Dr. Michael Barnes, Dr. Riccardo Nocentini, Guillermo Orozco, Markus Fröschle, Dr. Ante Hecimovic, Dr. Federico D'Isa, Christian Kiefer, Dr. Rodrigo Antunes** and all the other current and former co-workers which I surely forgot to mention (sorry :-)) for accompanying me during the time at IPP, the many fruitful discussions and many more cups of coffee. You gave me an example of how to be a good scientist which I try to live up to every single day.
- **Moritz Eckerskorn** und **Andreas Oberpriller** für eure Hilfe bei der Konstruktion der Lasereinhausung, von ALFRED und der Laserstrahleinhausung zu BATMAN Upgrade. Danke besonders Andi für die vielen Tage, die wir zusammen beim Basteln im BATMAN-Keller verbracht haben.
- **Alexander Oswald, Harald Fleck, Peter Klein, Sepp Deimel** und **Erik Heinz** für die immerwährende Unterstützung bei allen Konstruktionsproblemen, die ich an BATMAN hatte. Danke besonders Alex dafür, dass du immer ein offenes Ohr für mich hattest und immer eine Lösung gefunden hast.
- **Jürgen Steinberger** und **Philippe Araba** für die vielen Bauteile, die ich bei euch in Konstruktion gegeben habe und die vielen Ideen, die ihr zur Erstellung von meinen Plänen beigetragen habt.
- **Martin Kammerloher** und **Johannes Kolbinger** für den Bau vieler elektronischer Komponenten für die TALIF und die vielen Stunden auf der Suche nach RF-Störungen und wie man sie beseitigt.
- **Waltraud Sinz** und **Kurt Ritter** für alle organisatorischen Dinge und Computerprobleme, bei denen ihr mich während der letzten 3.5 Jahre unterstützt habt.
- Zu guter Letzt will ich mich bei meinen Eltern, meinen Geschwistern, meiner restlichen Familie, meinen Freunden, meinen Mitbewohner*innen, allen Mitmusiker*innen der letzten Jahre und ganz besonders bei meiner Freundin bedanken. Danke für den Rückhalt in manchmal schweren Zeiten, eure Geduld und euer Verständnis während meiner gesamten Doktorandenzeit.